OFFICIAL JOURNAL OF THE SCIENTIFIC SOCIETY OF ANATOMISTS, HISTOLOGISTS, EMBRYOLOGISTS AND TOPOGRAPHIC ANATOMISTS OF UKRAINE

DOI: 10.31393
ISSN 1818-1295
eISSN 2616-6194

ВІСНИК МОРФОЛОГІЇ
REPORTS OF MORPHOLOGY

VOL. 32, №1, 2026

Scientific peer-reviewed journal in the fields of normal and pathological anatomy, histology, cytology and embryology, topographical anatomy and operative surgery, biomedical anthropology, ecology, molecular biology, biology of development

Published since 1993
Periodicity: 4 times a year

Vinnytsya • 2026

ВІСНИК МОРФОЛОГІЇ - REPORTS OF MORPHOLOGY

Founded by the “Scientific Society of Anatomists, Histologists, Embryologists, and Topographic Anatomists of Ukraine” and National Pyrogov Memorial Medical University, Vinnytsya in 1993

Certificate of state registration КВ №9310 from 02.11.2004

Professional scientific publication of Ukraine in the field of medical sciences in specialties 221, 222, 228, 229
According to the list of professional scientific publications of Ukraine, approved by the order of the Ministry of Education and Science of Ukraine No. 1188 of 24.09.2020

Professional scientific publication of Ukraine in the field of biological sciences in specialty 091
According to the list of professional scientific publications of Ukraine, approved by the order of the Ministry of Education and Science of Ukraine No. 1471 of 26.11.2020

Approved by the Academic Council of National Pyrogov Memorial Medical University, Vinnytsya, protocol №8 from 26.02.2026.

Indexation: Scopus, CrossRef, Index Copernicus, Google Schoolar Metrics, National Library of Ukraine Vernadsky

Address editors and publisher:
Pyrogov Str. 56,
Vinnytsya, Ukraine - 21018
Tel.: +38 (0432) 553959
E-mail: nila@vnmu.edu.ua

Computer page-proofs - Slobodianiuk L.M.
Translator - Gunas V.I.
Technical support - Levenchuk S.S.
Scientific editing - editorship

The site of the magazine - https://morphology-journal.com

CONTENT

DOI: 10.31393/morphology-journal-2026-32(1)-01

Reports of Morphology, Vol. 32, №1, Pages 5-12

ISSN 1818-1295 eISSN 2616-6194

REPORTS OF MORPHOLOGY

Official Journal of the Scientific Society of Anatomists, Histologists, Embryologists and Topographic Anatomists of Ukraine

journal homepage: https://morphology-journal.com

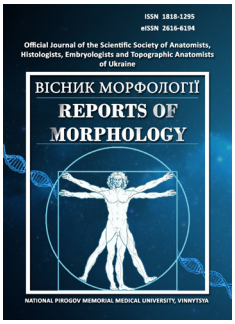

Dynamics of hippocampal morphological changes in condition of cisplatin and paclitaxel combined administration

Kulynych H. B., Herashchenko S. B., Fedorak V. M., Yurah H. Yu., Polyvkan M. I., Atamanchuk O. V.

Ivano-Frankivsk National Medical University, Ivano-Frankivsk, Ukraine

ARTICLE INFO

Received: 17 June 2025

Accepted: 10 November 2025

UDC: 611.813.7-009.17-092.9:615.277.3

CORRESPONDING AUTHOR

e-mail: e-mail: galija1979@ukr.net

Kulynych H. B.

CONFLICT OF INTEREST

The authors have no conflicts of interest to declare.

FUNDING

Not applicable.

DATA SHARING

Data are available upon reasonable request to corresponding author.

Combined chemotherapy regimens involving the concurrent administration of cisplatin and paclitaxel remain a standard approach for the treatment of many solid tumors; however, they are associated with a high incidence of neurotoxic complications. The central component of neurotoxicity remains insufficiently studied. The hippocampus is one of the most vulnerable structures of the central nervous system. Fragmentary data on the phasic nature, temporal dynamics, and morphofunctional correlates of central neurotoxicity with the simultaneous use of cisplatin and paclitaxel form a gap between the clinical manifestations of cognitive deficit and the results of most experimental models. The aim of this study was to characterize the temporal dynamics of morphological changes in the rat hippocampus following the concurrent administration of cisplatin and paclitaxel and to identify the key phases of central neurotoxicity development. Experimental studies were performed on adult male white inbred rats weighing 180-220 g. Morphological and morphometric changes in the hippocampus were evaluated on days 1, 7, 14, 28, 60, 90, and 120 after treatment using light microscopy and morphometric analysis of neuronal and glial elements. Statistical analysis was performed using one-way analysis of variance (ANOVA) and the Mann-Whitney U test. Concurrent administration of cisplatin and paclitaxel resulted in a phase-dependent pattern of hippocampal injury. In the early observation periods, edematous-dystrophic neuronal changes and disturbances of neuroglial interactions predominated. On days 7-14, progressive destructive processes were observed, while day 28 was characterized by the maximal level of morphological damage with pronounced disorganization of the pyramidal layer. In the late periods (60-120 days), signs of incomplete morphological repair were detected, including partial restoration of layer organization with persistent reactive glial changes. The obtained results indicate that the concurrent administration of cisplatin and paclitaxel leads to persistent structural alterations of the hippocampus, which may underlie cognitive disorders and substantiate the need for further investigation of neuroprotective strategies.

Keywords: *hippocampus, neurotoxicity, cisplatin, paclitaxel, combined chemotherapy, morphology, CA1 and CA3 neurons.*

Introduction

Combined chemotherapeutic regimens involving the concurrent administration of cisplatin and paclitaxel remain a cornerstone in the treatment of numerous solid malignancies. Despite their well-established clinical efficacy, these protocols are associated with a high incidence of neurotoxic complications. Clinical observations in patients receiving platinum-taxane regimens have documented impairments in memory and attention, slowed cognitive processing, and affective disturbances. These manifestations are consistent with experimental evidence demonstrating the adverse impact of chemotherapy on neurogenesis and cognitive function [4, 6, 19].

Such cognitive sequelae following systemic chemotherapy are linked to long-lasting alterations in neuronal plasticity and adult neurogenesis, as confirmed by both experimental and clinically oriented studies [1].

Although chemotherapy induced peripheral neuropathy has been extensively investigated, the central component of neurotoxicity remains insufficiently systematized at the experimental level. In this context, the hippocampus exhibits

particular vulnerability. As a structure characterized by high metabolic activity, its functional integrity critically depends on the preservation of neurogliovascular units. Cisplatin induces DNA damage, disrupts mitochondrial homeostasis, and activates apoptotic signaling pathways [2, 15, 16]. Paclitaxel, in turn, destabilizes microtubule dependent transport and promotes glial activation [10, 13, 18]. The convergence of these pathogenic mechanisms produces a synergistic toxic effect that may potentiate hippocampal injury [5, 11].

Despite this, data regarding the phased and temporal dynamics of central neurotoxicity under simultaneous exposure to cisplatin and paclitaxel remain fragmented. This gap limits the precise identification of morphological and functional correlates associated with specific chemotherapeutic regimens. Most preclinical models of paclitaxel-induced neurotoxicity are based on short-term protocols lasting 2-3 weeks, employing high single doses with a limited number of injections. While such approaches rapidly induce peripheral neuropathy, they fail to reproduce the gradual evolution of central nervous system damage observed in clinical practice [3, 12, 21].

In contrast, real-world therapeutic programs typically involve prolonged treatment schedules of 6-18 weeks, characterized by lower single doses but substantially higher cumulative exposure to paclitaxel, frequently combined with platinum-based agents [8, 9, 22, 25]. This pattern of exposure induces chronic, phase-dependent central neurotoxicity whose parameters do not correspond to those modeled in conventional experimental paradigms. The discrepancy between clinical manifestations of central toxicity and findings from standard preclinical studies necessitates a targeted analysis of hippocampal morphological alterations under prolonged combined cisplatin and paclitaxel administration that more closely reflects clinical treatment protocols.

Recent evidence further indicates the involvement of ion channels, particularly voltage-gated sodium channels, in the mechanisms of paclitaxel-induced neurotoxicity, thereby expanding the pathogenetic framework of central nervous system injury [23].

Aim of the study: to characterize the temporal dynamics of morphological changes in the rat hippocampus following concurrent administration of cisplatin and paclitaxel, and to identify the key phases in the development of central neurotoxicity.

Materials and methods

The study was conducted on sexually mature male white inbred rats weighing 180-220 g. The animals were housed in the vivarium of Ivano-Frankivsk National Medical University under standard conditions: temperature 21±2 °C, relative humidity 55-60 %, and a 12/12-hour light-dark cycle, with free access to food and water. A seven-day acclimatization period was provided prior to the initiation of the experiment. Euthanasia was performed by inhalational overdose of ether anesthesia. All animals survived until the scheduled experimental endpoints.

All procedures were carried out in accordance with the European Convention for the Protection of Vertebrate Animals Used for Experimental and Other Scientific Purposes (Strasbourg, 1986) and the Declaration of Helsinki (2013). The study protocol was approved by the Bioethics Commission of Ivano-Frankivsk National Medical University (Protocol No. 146/24, dated 26 September 2024).

The control group consisted of intact animals that received no pharmacological agents and were maintained under identical housing conditions (n=30). Combined toxicity was induced by concurrent intraperitoneal administration of cisplatin at a dose of 2 mg/kg (the solution was pre-warmed to 37 °C immediately before injection) and intravenous administration of paclitaxel at a dose of 5 mg/kg via the tail vein once weekly for six consecutive weeks (n=30). This regimen ensures dose equivalence to clinical combined chemotherapy protocols.

The selected doses of cisplatin (2 mg/kg) and paclitaxel (5 mg/kg) were aligned with clinically relevant exposure levels. Dose conversion was performed using the human equivalent dose method, whereby the animal dose was translated into a human dose using Km coefficients for rats (6) and humans (37), in accordance with the recommendations of Reagan-Shaw S. et al. [24]. The cumulative doses were 12 mg/kg for cisplatin and 30 mg/kg for paclitaxel.

Animals were sacrificed on days 1, 7, 14, 28, 60, 90, and 120. The hippocampus was fixed in 10 **%** neutral buffered formalin, embedded in paraffin, and semi-thin sections were prepared for light microscopy and morphometric analysis of neurons in the CA1 and CA3 regions. Morphometric evaluation was performed on serial histological sections stained with hematoxylin and eosin. The following parameters were assessed: perikaryal area, nuclear diameter, nuclear-to-cytoplasmic ratio, and neuronal density per visual field. For each animal, at least 10 fields were analyzed from three non-consecutive sections. Measurements were obtained digitally using a calibrated microscopy system and ImageJ software.

Statistical analysis was performed in Python using the SciPy library. Parametric comparisons were conducted using one-way analysis of variance (ANOVA), and nonparametric pairwise comparisons were performed using the Mann-Whitney U test. Data are presented as mean±standard deviation (M±SD). Differences were considered statistically significant at $p<0.05$.

The experimental study was carried out from April to October 2025, which was determined by the staged withdrawal of animals at predefined time points.

Results

In intact rats, the morphological organization of the hippocampus corresponded to age-matched normal morphology. Morphometric parameters of neurons in the CA1 and CA3 regions showed no statistically significant differences across the observation time points and remained stable throughout the study period.

Morphological examination of the hippocampus in

experimental animals revealed a distinct temporal pattern of toxic injury developing under concurrent cisplatin and paclitaxel administration.

On day 1, an early response to toxic exposure was observed. This stage was characterized by pericellular edema, cytoplasmic vacuolization, and partial rarefaction of the molecular layer. Moderate swelling of CA1 neurons was noted, while astrocytes exhibited early signs of hyperactivation, manifested by thickening of cellular processes and enlargement of perikarya.

Histological micrographs demonstrated initial hippocampal alterations typical of the acute toxic phase. Vacuolization of pyramidal neuron perikarya was evident, along with focal areas of cytoplasmic clearing, indicating edema and early disruption of ionic homeostasis. The molecular layer displayed focal tissue loosening, and intercellular spaces appeared moderately widened. Neurons retained their general contours; however, cytoplasmic heterogeneity was clearly detectable. Glial cells within the visual field responded with thickened cytoplasmic processes, consistent with early astrocytic activation.

Overall, the morphological pattern corresponded to initial structural alterations of the hippocampus, dominated by edematous-dystrophic changes (Fig. 1A).

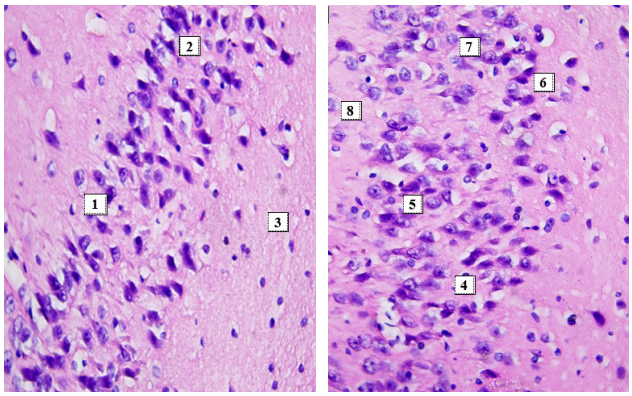

A B

Fig. 1. Morphological changes of the hippocampus in the early phase of combined cisplatin and paclitaxel toxicity on day 1 (fragment A) and day 7 (fragment B) of the experiment. 1 – neuroplasmic edema, 2 – cytoplasmic vacuolization, 3 – focal rarefaction of the molecular layer, 4 – pyknotic neurons, 5 – nuclear shrinkage, 6 – chromatin condensation, 7 – pericellular edema, 8 – disruption of CA1 laminar organization. Hematoxylin-eosin, ×400.

Beginning from day 7, pronounced signs of destruction became evident: pyknotic nuclei, hyperchromasia, and shrinkage of perikarya. The laminar organization of CA1 appeared irregular, and the number of dystrophic neurons increased.

The presented micrograph clearly demonstrates that the injury acquired a more overtly destructive character. Pyknotic neurons with dark, shrunken nuclei and condensed chromatin were observed. The perikarya of individual cells were reduced in size, with irregular contours, indicating progression of cytopathic processes. The lamination of the pyramidal layer was disrupted, and neuronal rows became uneven, with marked disorganization of the CA1 region.

Small foci of neuroplasmic lysis were also detected, along with early signs of cytoskeletal fragmentation. Background glial elements retained a reactive appearance, confirming the presence of a neuroinflammatory component.

Thus, the constellation of these alterations is characteristic of the initial destructive phase of toxicity (Fig. 1B).

From day 14 of the experiment, profound dystrophic changes in pyramidal neurons were recorded (Fig. 2A).

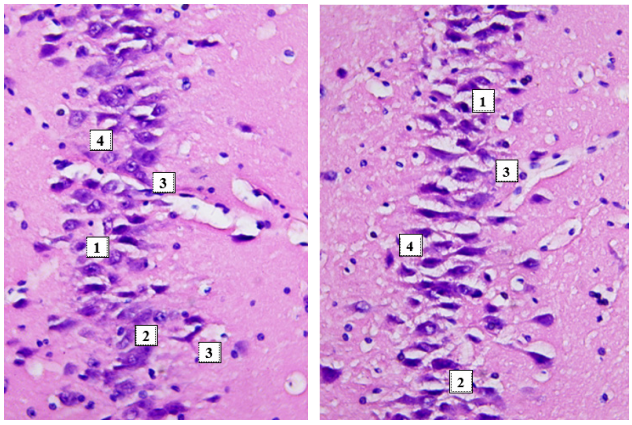

A B

Fig. 2. Profound destructive changes of the hippocampus during the period of maximal injury on day 14 (fragment A) and day 28 (fragment B) of the experiment. 1 – degeneration of CA1-CA3 neurons (of varying severity), 2 – fragmentation and homogenization of neuroplasm, 3 – pericellular and interstitial edema, 4 – disruption of synaptic zones. Hematoxylin-eosin, ×400.

The cytoplasm appeared unevenly cleared, with areas of neuroplasmic disintegration and fragmentation, indicating destruction of intracellular structures. The nuclei of a substantial proportion of neurons were deformed or shrunken, and focal chromatin condensation was observed. Pericellular spaces were markedly widened, consistent with pronounced edema.

The laminar organization of the CA1-CA3 regions was disrupted: the regular alignment of neuronal rows was lost, neuronal contours became indistinct, and the stroma exhibited foci of vacuolization and tissue rarefaction. The overall morphological pattern corresponded to a phase of progressive toxic destruction dominated by cytopathic mechanisms of injury.

By day 28, toxic alterations reached their culmination, and neuronal destruction acquired a massive character (Fig. 2B). The majority of CA1-CA3 neurons were in a state of profound degeneration or complete structural breakdown. In some areas, the neuroplasm transformed into a homogeneous mass, perikaryal contours were obliterated, and nuclei were either absent or represented by dark residual structures. The stroma contained numerous zones of extensive edema, with lysed fragments and areas of marked tissue disorganization.

Synaptic zones, normally well delineated within the pyramidal layer, appeared fragmented or completely disrupted, indicating severe impairment of neuronal connectivity. The overall histoarchitecture of the hippocampus was substantially distorted, with pronounced laminar disorganization, a feature clearly corresponding to the phase of maximal cytotoxic impact of the combined cytostatic agents.

By day 60, a reduction in the extent of toxic injury was observed; however, hippocampal architecture remained far from normal (Fig. 3A).

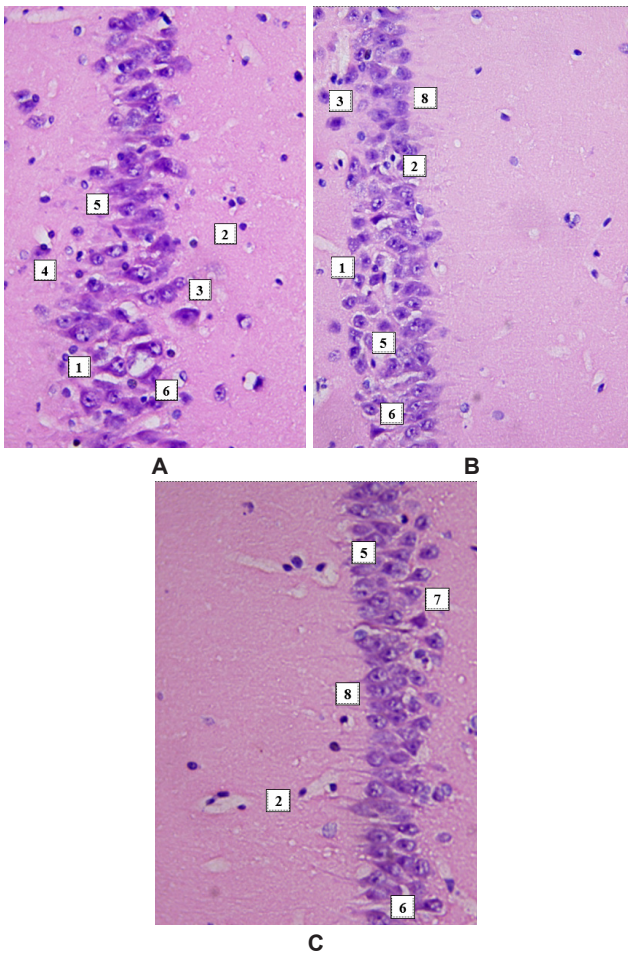

Fig. 3. Dynamics of morphological repair of the hippocampus at delayed time points of combined toxicity on days 60 (fragment A), 90 (fragment B), and 120 (fragment C) of the experiment. 1 – partial destruction and dystrophy of perikarya, 2 – residual glial and interstitial edema, 3 – irregular laminar organization of pyramidal neurons, 4 – reactive astrocytes with thickened and elongated processes, 5 – areas of partial neuronal normalization, 6 – residual dystrophic neurons, 7 – signs of restoration of astrocytic processes and stabilization of neuroglial interactions, 8 – narrowed intercellular spaces and reduction of cerebral edema. Hematoxylin-eosin, ×400.

At delayed time points of combined toxicity, signs of incomplete morphological repair persisted in the hippocampus. The perikarya of individual neurons remained dystrophically altered: the cytoplasm exhibited uneven staining with areas of clearing and fragmentation. Pericellular spaces were focally widened, reflecting the persistence of residual glial and interstitial edema.

The laminar organization of the pyramidal layer showed partial restoration; however, neuronal rows remained irregular, with localized areas of rarefaction. Astrocytic elements demonstrated sustained reactivity, manifested by thickening and elongation of processes and heterogeneity of cytoplasmic staining. At the same time, in certain visual fields, signs of stabilization of neuroglial interactions were observed, accompanied by reduction of edema and narrowing of intercellular spaces.

Overall, the detected alterations corresponded to a phase of partial morphological stabilization of the hippocampus, with persistence of residual manifestations of toxic injury.

By day 90, the morphological pattern was consistent with a phase of moderate repair. Neuronal cell bodies acquired more regular contours, and nuclei appeared lighter, with less condensed chromatin. The alignment of pyramidal neurons gradually improved, and the degree of their disorganized arrangement decreased.

In the intercellular matrix, the number of edematous zones diminished, although foci of glial reactivity were still present. Preserved neurons with features of partial ultrastructural normalization were observed; however, areas containing dystrophic remnants of prior injury persisted.

This morphological presentation indicates incomplete yet moderately progressive repair (Fig. 3B).

At the most remote time point, day 120, signs of morphological repair were observed. Perikaryal contours became more regular, neuronal cytoplasm appeared more homogeneous, and chromatin acquired a more typical distribution pattern. Astrocytes demonstrated restored process architecture, indicating stabilization of neuroglial interactions.

The laminar structure of the hippocampus approached near-orderly organization, and intercellular spaces were narrowed. The number of edematous zones in the stroma decreased. However, complete reconstruction of neuronal networks did not occur. Isolated dystrophic neurons, areas of subtle tissue rarefaction, and residual manifestations of prior toxic exposure were still present. The overall morphological pattern corresponded to a phase of incomplete but clearly evident recovery (Fig. 3C).

Morphometric parameters of hippocampal neurons at the peak of injury (day 28) following concurrent paclitaxel and cisplatin administration reflected pronounced alterations in perikaryal area, nuclear size, nuclear-to-cytoplasmic ratio, and neuronal density in response to combined toxicity (Table 1).

The morphometric data obtained on day 28 of the experiment demonstrate statistically significant alterations in neurons of the CA1 and CA3 regions of the hippocampus following concurrent administration of cisplatin and paclitaxel.

A decrease in perikaryal area, nuclear diameter, nuclear-

Table 1. Morphometric parameters of hippocampal neurons (CA1 and CA3) at the peak of injury (day 28) following concurrent administration of cisplatin and paclitaxel.

Parameter	Region	Control (M±SD)	Cisplatin + paclitaxel (M±SD)
Perikaryal area, μm²	CA1	178.4±12.6	132.7±10.9*
	CA3	196.2±14.1	147.8±12.3*
Nuclear diameter, μm	CA1	7.423±0.381	6.112±0.414*
	CA3	7.889±0.442	6.481±0.370*
Nuclear-to-cytoplasmic ratio	CA1	0.408±0.027	0.331±0.019*
	CA3	0.393±0.040	0.309±0.027*
Neuronal density, cells per field of view	CA1	22.82±2.38	15.61±2.10*
	CA3	20.33±2.09	13.92±1.83*

Notes: data are presented as M**±**SD; * – p<0.05 compared with control.

to-cytoplasmic ratio, and neuronal density is consistent with the findings of light microscopic analysis and reflects the development of dystrophic and destructive processes within the pyramidal layer of the hippocampus at the peak of combined neurotoxicity.

Discussion

The obtained morphological findings reflect a sequential, phase-dependent development of central neurotoxicity under combined cisplatin and paclitaxel administration. As early as day 1, initial signs of cytotoxic stress were detected, manifested by pericellular edema, cytoplasmic vacuolization, and reduced density of the molecular layer.

Similar acute responses have been described in experimental models of 5-fluorouracil and paclitaxel exposure, where primary destabilization of ionic homeostasis and activation of glial cells create an early toxic milieu [10, 18]. Our observations are consistent with these data and further support the concept that the initial phase of combined exposure is accompanied by disruption of neuron-glia interactions, which are regarded as one of the key triggering mechanisms of central chemotherapy-induced toxicity [30].

The generalized mechanisms of central chemotherapy-induced neurotoxicity, including neuroinflammation, oxidative stress, and disruption of neurotransmitter systems, have been comprehensively described in recent review articles [2].

In the early period following cisplatin administration, the development of cytopathic alterations in the hippocampus has been reported, associated with impaired energy metabolism and activation of stress-dependent signaling pathways [7].

Concurrently, experimental models of paclitaxel-induced neurotoxicity indicate a systemic pattern of toxic alterations that is not confined to the peripheral nervous system but may extend to central nervous system structures. This is supported by contemporary review data emphasizing the systemic nature of chemotherapy-related neurotoxicity [3, 17, 27]. In this context, the early hippocampal morphological disturbances identified in our study reflect the cumulative effect of both agents already at the initial stages of exposure.

During the intermediate period (7-14 days), destructive processes predominated, including the appearance of pyknotic nuclei, fragmentation of neuroplasm, deformation of perikarya, and disruption of the laminar organization of the CA1 region.

Experimental studies have demonstrated that paclitaxel induces a neuroinflammatory response in the hippocampus, accompanied by elevated levels of proinflammatory cytokines, particularly TNF-α and IL-1β [14]. At the level of gene expression, this response evolves into a broader cascade of signaling pathways associated with inflammation, oxidative stress, and activation of apoptotic mechanisms [13]. Cisplatin further amplifies these processes by disrupting mitochondrial homeostasis and activating caspase-dependent pathways of neuronal injury [15, 16]. Thus, the intermediate phase reflects the combined action of both cytostatic agents, which is fully consistent with the morphological findings obtained in the present study.

The peak of injury on day 28 was characterized by massive neuronal destruction within the CA1-CA3 regions, cytoskeletal disorganization, and disruption of synaptic architecture. Similar hippocampal morphological alterations have been described in models of Taxol-induced neurotoxicity [18].

Data reported by Kang S. et al. [12] indicate that combined chemotherapy results in substantial deformation of hippocampal microarchitecture and reduced dendritic complexity, which corroborates our findings under concurrent cisplatin and paclitaxel administration. Clinically significant cognitive deficits following chemotherapy are widely documented in both clinical and experimental studies [20, 29], and reduced neurogenesis together with impaired structural integrity of the hippocampus are considered their morphological substrate [6].

The morphometric parameters obtained on day 28 reflect the phase of maximal hippocampal injury. A 25-30 % reduction in the perikaryal area of CA1 and CA3 pyramidal neurons, decreased nuclear diameter, and more than a 30 % decline in neuronal density are consistent with data from experimental models of paclitaxel- and platinum-induced neurotoxicity, in which the peak of degenerative changes typically occurs during the third to fourth week of exposure.

Comparable morphometric shifts have been reported by Mercado-Gómez O. et al. [18], Kang S. et al. [12], and Manohar S. et al. [16], thereby supporting the validity of the selected model and the interpretation of the present findings.

At delayed observation time points (60-120 days), partial reparative changes were noted in both neuronal and glial elements; however, complete restoration of hippocampal morphological organization did not occur. The persistence of astrocytic reactivity, disruption of laminar structure, and the presence of dystrophically altered neurons are consistent with reports of prolonged suppression of neurogenesis and sustained dysfunction of neuron-glia interactions following systemic chemotherapy [1, 4, 19, 28]. These findings indicate a persistent toxic process that continues even after cessation of drug administration.

The combined effect of cisplatin and paclitaxel exhibits a pronounced synergistic pattern. Cisplatin induces DNA damage and mitochondrial dysfunction [16, 17], whereas paclitaxel disrupts microtubule dynamics and promotes glial activation and neuroinflammation [11, 14, 18].

In the study by Carozzi V. et al. [5], concurrent exposure to these agents was shown to markedly exacerbate neurotoxicity and alter glial cell reactivity. Such synergy explains the severity of injury observed in our model, ranging from early destabilization of ionic fluxes to pronounced structural disorganization of hippocampal tissue.

Particular attention should be given to data implicating ion channels and transporters in the mechanisms of chemotherapy-induced neurotoxicity. Recent studies indicate the involvement of voltage-gated sodium channels in the development of functional and structural disturbances of nervous tissue under paclitaxel exposure [23, 27]. In light of the morphological alterations identified in our study, impaired membrane stability and altered electrical conductivity may represent one of the key mechanisms of neuronal injury in this model.

Thus, the present findings demonstrate that prolonged weekly administration of cisplatin and paclitaxel induces a sequential cascade of hippocampal damage, ranging from an acute edematous-dystrophic response to maximal structural destruction followed by incomplete repair. The persistence of morphological defects at delayed time points is consistent with reports of sustained cognitive deficits after systemic chemotherapy [6, 19, 20, 29].

These observations underscore the rationale for early implementation of neuroprotective strategies aimed at attenuating neuroinflammation, preserving mitochondrial homeostasis, and stabilizing neuronal structures, which are considered promising approaches for the prevention of platinum-taxane-induced neurotoxicity [26].

At the same time, the obtained results should be interpreted in light of certain study limitations. The morphological analysis was primarily based on light microscopy and conventional histological staining, which does not allow differentiation of the contribution of specific cellular populations or molecular mechanisms of injury. Further investigations employing immunohistochemical markers of neurons and glial cells (NeuN, GFAP, Iba-1), as well as methods for assessing apoptosis and neuroinflammation, may provide deeper insight into the cellular basis of the observed alterations.

Moreover, integration of morphological findings with behavioral assessments represents a promising approach for establishing the functional relevance of hippocampal structural damage and for substantiating targeted neuroprotective strategies in taxane platinum chemotherapy.

Thus, concurrent administration of cisplatin and paclitaxel induces a sequential pattern of morphological alterations in the hippocampus encompassing an acute phase (day 1), early destruction (7-14 days), peak injury (day 28), and a phase of incomplete repair (60-120 days). Neurons within the CA1 and CA3 regions appear particularly vulnerable, with toxicity characterized by profound cytoskeletal disruption, synaptic disorganization, and impairment of neurovascular units.

The present findings substantiate the need for continued investigation of neuroprotective strategies aimed at the prevention and correction of chemotherapy-induced neurotoxicity.

Conclusions

1. For the first time, it has been demonstrated that six-week chronic exposure to paclitaxel (5 mg/kg × 6), administered concurrently with cisplatin, induces pronounced time-dependent morphological alterations in the hippocampus that differ from the effects observed in short-term low-dose preclinical models.

2. Concurrent administration of paclitaxel and cisplatin produces a phase-dependent cascade of hippocampal injury encompassing an acute response, progressive destruction, a peak of degeneration on day 28, and incomplete morphological repair at delayed time points, with predominant involvement of neurons in the CA1 and CA3 regions.

3. The identified disorganization of neuronal, synaptic, and glial elements within the hippocampus provides a morphological substrate for the development of cognitive impairment and substantiates the rationale for further investigation of neuroprotective strategies in taxane-platinum chemotherapy.

References

[1] Acharya, M. M., Martirosian, V., Chmielewski, N. N., Hanna, N., Tran, K. K., Liao, A. C., ... & Limoli, C. L. (2015). Stem cell transplantation reverses chemotherapy-induced cognitive dysfunction. *Cancer Research*, *75*(4), 676-686. doi: 10.1158/0008-5472.CAN-14-2237

[2] Areti, A., Komirishetty, P., Kumar, A., & Kumar, A. (2020). Role of oxidative stress and mitochondrial dysfunction in chemotherapy-induced peripheral neuropathy. *Molecular Neurobiology*, *57*(4), 2161-2177. doi: 10.1007/s12035-019-01853-0

[3] Authier, N., Gillet, J.-P., Fialip, J., Eschalier, A., & Coudore, F. (2000). A new animal model of vincristine-induced nociceptive peripheral neuropathy. *Brain Research*, *887*(2), 239-249. doi: 10.1016/S0006-8993(00)02910-3

[4] Briones, T. L., & Woods, J. (2011). Chemotherapy-induced cognitive impairment is associated with decreases in cell proliferation and histone modifications. *BMC Neuroscience*, *12*, 124. doi: 10.1186/1471-2202-12-124

[5] Carozzi, V., Chiorazzi, A., Canta, A., Oggioni, N., Gilardini, A., Rodriguez-Menendez, V., … & Cavaletti, G. (2009). Effect of the chronic combined administration of cisplatin and paclitaxel in a rat model of peripheral neurotoxicity. *European Journal of Cancer*, *45*(4), 656-665. doi: 10.1016/j.ejca.2008.10.038

[6] Christie, L.-A., Acharya, M. M., Parihar, V. K., Nguyen, A., Martirosian, V., & Limoli, C. L. (2012). Impaired cognitive function and hippocampal neurogenesis following cancer chemotherapy. *Clinical Cancer Research*, *18*(7), 1954-1965. doi: 10.1158/1078-0432.CCR-11-2000

[7] Domouky, A. M., Deraz, R. H., & Abdel-Kareem, R. H. (2022).

Neurotoxicity of cisplatin in hippocampus. *Egyptian Society of Clinical Toxicology Journal*, *10*, 29-48. doi: 10.21608/esctj.2022.135931.1008

[8] Ferris, C. F., Yee, J. R., Kenkel, W. M., Dumais, K., Moore, K., Rogers, J., … & Stolberg, T. (2019). Paclitaxel treatment disrupts brain functional connectivity and promotes affective and cognitive impairments in rodents. *Frontiers in Pharmacology*, *10*, 931. doi: 10.3389/fphar.2019.00931

[9] Ghamande, S., Lele, S., Marchetti, D., Baker, T., & Odunsi, K. (2003). Weekly paclitaxel in patients with ovarian cancer: A clinical experience. *International Journal of Gynecological Cancer*, *13*(2), 142-147. doi: 10.1046/j.1525-1438.2003.13045.x

[10] Groves, T. R., Farris, R., Anderson, J. E., Alexander, T. C., Kiffer, F., Carter, G., … & Allen, A. R. (2017). 5-fluorouracil chemotherapy upregulates cytokines and alters hippocampal dendritic complexity in aged mice. *Behavioural Brain Research*, *316*, 215-224. doi: 10.1016/j.bbr.2016.08.039

[11] Imai, S., Koyanagi, M., Azimi, Z., Matsumoto, M., Hisaoka, K., Yamamoto, N., ... & Narita, M. (2017). Taxanes and platinum derivatives impair glial function and enhance neuroinflammation. *Scientific Reports*, *7*, 5947. doi: 10.1038/s41598-017-05784-1

[12] Kang, S., Lee, S., Kim, J., Kim, J.-C., Kim, S.-H., Son, Y., … & Moon, C. (2018). Chronic treatment with combined chemotherapeutic agents affects hippocampal micromorphometry and function in mice, independently of neuroinflammation. *Experimental Neurobiology*, *27*(5), 419-436. doi: 10.5607/en.2018.27.5.419

[13] Li, Y., Yin, C., Liu, B., Nie, H., Wang, J., Zeng, D., … & Zhang, P. (2021). Transcriptome profiling reveals neuroinflammation- and apoptosis-related pathways in paclitaxel-induced neuropathy. *Journal of Neuroinflammation*, *18*, 48. doi: 10.1186/s12974-021-02098-y

[14] Li, Z., Zhao, S., Zhang, H., Liu, P., Liu, F., Guo, Y., & Wang, X. (2018). Proinflammatory factors mediate paclitaxel-induced impairment of learning and memory. *Mediators of Inflammation*, 2018, 3941840. doi: 10.1155/2018/3941840

[15] Lomelí-Cardona, N., Chávez-Munguía, B., García-Rodríguez, A., Martínez-Fong, D., & Arias, C. (2017). Cisplatin-induced mitochondrial dysfunction and oxidative damage in the central nervous system. *Free Radical Biology and Medicine*, *108*, 41-50. doi: 10.1016/j.freeradbiomed.2017.02.020

[16] Manohar, S., Jamesdaniel, S., & Salvi, R. (2014). Cisplatin inhibits hippocampal cell proliferation and triggers neuronal injury: Possible basis for chemotherapy-related cognitive impairment. *Neurotoxicity Research*, *25*(4), 369-380. doi: 10.1007/s12640-013-9443-y

[17] Mattar, M., Umutoni, F., Hassan, M. A., Wamburu, M. W., Turner, R., Patton, J. S., ... & Lei, W. (2024). Chemotherapy-Induced Peripheral Neuropathy: A Recent Update on Pathophysiology and Treatment. *Life (Basel)*, *14*(8), 991. doi: 10.3390/life14080991

[18] Mercado-Gómez, O., Ferrera, P., & Arias, C. (2004). Taxol-induced neurotoxicity in hippocampus: Morphological and functional correlates. *Journal of Neuroscience Research*, *78*(4), 553-562. doi: 10.1002/jnr.20264

[19] Nokia, M. S., Anderson, M. L., & Shors, T. J. (2012). Chemotherapy disrupts hippocampal theta oscillations and impairs memory-related processing. European *Journal of Neuroscience*, *36*(11), 3521-3530. doi: 10.1111/j.1460-9568.2012.08268.x

[20] Peukert, X., Pagenstecher, A., & van Wijk, N. (2020). Cognitive deficit after systemic chemotherapy: Mechanisms and translational relevance. *Frontiers in Oncology*, 10, 147. doi: 10.3389/fonc.2020.00147

[21] Pignata, S., Scambia, G., Katsaros, D., Gallo, C., Pujade-Lauraine, E., De Placido, S., ... & Perrone, F. (2014). Carboplatin plus paclitaxel once a week versus every 3 weeks in patients with advanced ovarian cancer (MITO-7): A randomised, multicentre, open-label, phase 3 trial. *The Lancet Oncology*, *15*(4), 396-405. doi: 10.1016/S1470-2045(14)70049-X

[22] Polomano, R. C., Mannes, A. J., Clark, U. S., & Bennett, G. J. (2001). A painful peripheral neuropathy in the rat produced by the chemotherapeutic drug, paclitaxel. *Pain*, *94*(3), 293-304. doi: 10.1016/S0304-3959(01)00363-3

[23] Pozzi, E., Terribile, G., Cherchi, L., Di Girolamo, S., Sancini, G., & Alberti, P. (2024). Ion channel and transporter involvement in chemotherapy-induced peripheral neurotoxicity. *International Journal of Molecular Sciences*, *25*(12), 6552. doi: 10.3390/ijms25126552

[24] Reagan-Shaw, S., Nihal, M., & Ahmad, N. (2008). Dose translation from animal to human studies revisited. *FASEB Journal*, *22*(3), 659-661. doi: 10.1096/fj.07-9574LSF

[25] Sparano, J. A., Wang, M., Martino, S., Jones, V., Perez, E. A., Saphner, T., … & Sledge, G. W. (2008). Weekly paclitaxel in the adjuvant treatment of breast cancer. *New England Journal of Medicine*, *358*(16), 1663-1671. doi: 10.1056/NEJMoa0707056

[26] Stanković, J. S. K., Selaković, D., Joksimović, J., Jakovljević, V., Mihailović, V., & Stojanović, N. M. (2020). Antioxidant supplementation in the treatment of platinum-induced neurotoxicity: Mechanistic rationale and evidence. *International Journal of Molecular Sciences*, *21*(20), 7753. doi: 10.3390/ijms21207753

[27] Tao, Z., Chen, Z., Zeng, X., Cui, J., & Quan, M. (2024). An emerging aspect of cancer neuroscience: A literature review on chemotherapy-induced peripheral neuropathy. *Cancer Lett*, *28*(611), 217433. doi: 10.1016/j.canlet.2024.217433

[28] Wellenberg, A., Brinkmann, V., Bornhorst, J., Ventura, N., Honnen, S., & Fritz, G. (2021). Cisplatin-induced neurotoxicity involves the disruption of serotonergic neurotransmission. *Pharmacological Research*, 174, 105921. doi: 10.1016/j.phrs.2021.105921

[29] Winocur, G., Vardy, J., Binns, M. A., Kerr, L., Tannock, I., & Wojtowicz, J. M. (2014). The effects of physical exercise on hippocampal neurogenesis and cognitive function in chemotherapy-treated rats. *Psychopharmacology*, *231*(11), 2311-2320. doi: 10.1007/s00213-013-3394-0

[30] Xing, B., Xin, T., Hunter, R. L., & Bing, G. (2007). Pioglitazone inhibition of microglial activation reduces dopaminergic neuronal loss and inflammatory responses. *Journal of Neuroimmunology*, *189*(1-2), 38-46. doi: 10.1016/j.jneuroim.2007.09.029

ДИНАМІКА МОРФОЛОГІЧНИХ ЗМІН У ГІПОКАМПІ ЗА УМОВ ОДНОЧАСНОГО ВВЕДЕННЯ ЦИСПЛАТИНУ ТА ПАКЛІТАКСЕЛУ

Кулинич Г. Б., Геращенко С. Б., Федорак В. М., Юрах Г. Ю., Поливкан М. І., Атаманчук О. В.

Комбіновані режими хіміотерапії з одночасним застосуванням цисплатину та паклітакселу залишаються стандартом

лікування багатьох солідних пухлин, однак асоціюються з високою частотою нейротоксичних ускладнень. Центральний компонент нейротоксичності й надалі залишається недостатньо вивченим. Гіпокамп є однією з найбільш вразливих структур центральної нервової системи. Фрагментарні дані щодо фазності, часової динаміки та морфофункціональних корелятів центральної нейротоксичності при одночасному застосуванні цисплатину та паклітакселу формують розрив між клінічними проявами когнітивного дефіциту та результатами більшості експериментальних моделей. Мета роботи – охарактеризувати часову динаміку морфологічних змін у гіпокампі щурів після одночасного введення цисплатину та паклітакселу та визначити ключові фази формування центральної нейротоксичності. Експериментальні дослідження проведено на статевозрілих самцях білих інбредних щурів масою 180-220 г. Морфологічні та морфометричні зміни гіпокампа оцінювали на 1, 7, 14, 28, 60, 90 та 120 добу після введення препаратів з використанням світлової мікроскопії та морфометрії нейронів і гліальних елементів. Статистичну обробку результатів здійснювали з використанням дисперсійного аналізу (ANOVA) та U-критерію Манна-Уїтні. Встановлено, що одночасна дія цисплатину та паклітакселу зумовлює фазний характер ушкодження гіпокампа. У ранні терміни спостереження переважали набряково-дистрофічні зміни нейронів і порушення нейрогліальних взаємодій. На 7-14 добу відзначали прогресування деструктивних процесів, а на 28 добу – максимальний рівень морфологічних ушкоджень із вираженою дезорганізацією пірамідного шару. У віддалені терміни (60-120 діб) виявляли ознаки неповної морфологічної репарації з частковим відновленням шарової організації та збереження реактивних гліальних змін. Отримані результати свідчать, що одночасне введення цисплатину та паклітакселу формує стійкі структурні порушення гіпокампа, які можуть лежати в основі когнітивних розладів і обґрунтовують необхідність подальшого пошуку нейропротекторних підходів.

Ключові слова: *гіпокамп, нейротоксичність, цисплатин, паклітаксел, комбінована хіміотерапія, морфологія, нейрони CA1 і CA3.*

Author's contribution

Kulynych G. B. – conceptualization, study design, investigation, data analysis, writing of the original draft, supervision.
Herashchenko S. B. – critical review, investigation, morphometric analysis, data interpretation.
Fedorak V. M. – statistical analysis, software.
Yurah G. Yu. – resources, validation.
Polyvkan M. I. – validation.
Atamanchuk O. V. – editing, validation.

DOI: 10.31393/morphology-journal-2026-32(1)-02 Reports of Morphology, Vol. 32, №1, Pages 13-18

ISSN 1818-1295 eISSN 2616-6194

REPORTS OF MORPHOLOGY

Official Journal of the Scientific Society of Anatomists, Histologists, Embryologists and Topographic Anatomists of Ukraine

journal homepage: https://morphology-journal.com

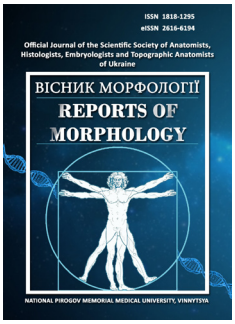

Modeling coronary sinus dimensions using regression analysis in patients without coronary artery pathology

Bilash S. M., Liulka Ye. M., Barannikov K. V., Pronina O. M., Shostya A. M., Koptev M. M., Pirog-Zakaznikova A. V., Oliinichenko Ya. O., Donchenko S. V., Oleksiienko V. V., Mamai O. V.

Poltava State Medical University, Poltava, Ukraine

ARTICLE INFO

Received: 4 June 2025

Accepted: 17 November 2025

UDC: 612.82:57.017.642

CORRESPONDING AUTHOR

e-mail: 0509539343@ukr.net

Liulka Ye. M.

CONFLICT OF INTEREST

The authors have no conflicts of interest to declare.

FUNDING

Not applicable.

DATA SHARING

Data are available upon reasonable request to corresponding author.

In contrast to the extensively studied anatomy of the arterial system of the heart, the venous system has remained in the background of researchers' interests. However, in recent years, the range of surgical procedures and manipulations involving the cardiac venous system has significantly expanded worldwide, including invasive electrophysiological studies and implantation of leads for left heart stimulation, among others. The aim of the study was to construct and analyze regression models of coronary sinus dimensions depending on anthropometric body parameters and other coronary sinus dimensions in patients without coronary artery pathology. A total of 24 patients (15 men and 9 women) of middle age (44-60 years according to the age classification of the World Health Organization) without coronary artery pathology were examined. All patients underwent CT coronary angiography at the State Institution "Amosov National Institute of Cardiovascular Surgery of National Academy of Medical Sciences of Ukraine" The study included patients without clinical manifestations of coronary artery disease. All patients underwent contrast-enhanced multislice computed tomography of the heart (CT coronary angiography) with assessment of anatomical parameters of the coronary venous sinus during the venous phase of contrast enhancement. Demographic (age, sex), anthropometric (body weight, height) and cardiometric parameters were introduced into the model as independent variables. Multiple linear regression analysis was performed using the licensed software package "Statistica 6.0" to identify the most significant factors. In all six constructed models of coronary sinus dimensions in patients without coronary artery pathology based on anthropometric parameters, the coefficient of determination (R^2) ranged from 0.122 to 0.468. Thus, the size of the coronary sinus depended on the studied body parameters by less than 50 %, and therefore these models have limited practical significance. All constructed models included the anteroposterior chest dimension, and only in one case was body length included. In six statistically significant models of coronary sinus dimensions in patients without coronary artery pathology based on other coronary sinus dimensions and anthropometric body parameters, the coefficient of determination ranged from 0.548 to 0.736. The constructed models most frequently included the transverse dimension of the coronary sinus at the ostium in the sagittal and axial planes, as well as the transverse dimension of the coronary sinus at the level of the oblique vein of the atrium in the axial plane (15.0 % each). These models may be applied in clinical practice for individualized preoperative assessment of the anatomy of the cardiac venous system. The proposed method of regression modeling of coronary sinus dimensions provides the possibility of noninvasive prediction of its parameters in patients without coronary artery pathology, thereby contributing to improved accuracy in planning invasive and interventional cardiology procedures.

Keywords: *coronary sinus, CT coronary angiography, morphometry, anthropometry, men and women without coronary artery pathology.*

Introduction

For a long time, the coronary venous system of the heart remained in the background of scientific interest, in contrast to the thoroughly studied and well-described coronary arterial bed, which is largely обусловлено the high number of life-

saving interventions performed on the coronary arteries [7, 14, 21, 35]. In recent years, the spectrum of diagnostic and therapeutic procedures in interventional cardiology involving the cardiac venous system has significantly expanded, including invasive electrophysiological studies, left ventricular pacing in cardiac resynchronization therapy, and delivery of stem cells to the myocardium after myocardial infarction, among others [1, 2, 9, 11].

Various methods are used to assess the anatomy of the cardiac venous bed, among which the study of cadaveric material and retrograde contrast imaging during interventional procedures predominate [23, 27, 30, 31]. A limitation of cadaveric studies is that the coronary venous sinus, as a soft elastic structure, lacks physiological turgor post mortem, which precludes accurate determination of its true dimensions [33]. Retrograde contrast imaging of the coronary venous sinus allows assessment of its anatomy only in a two-dimensional space, in contrast to contrast-enhanced multislice computed tomography synchronized with cardiac contractions (CT coronary angiography), which enables evaluation of all morphometric parameters in a three-dimensional format [5, 10, 20, 25].

Despite the substantial number of studies devoted to the morphometry of the coronary sinus, questions remain unresolved regarding the influence of individual anthropometric and cardiometric characteristics on its dimensions [8, 15, 22]. Moreover, most available data have been obtained from patients with cardiovascular pathology, which may distort normal anatomical relationships [17, 19, 28, 29]. The application of regression analysis methods makes it possible to develop predictive models that allow estimation of coronary sinus dimensions in patients without structural changes of the coronary bed. This provides a basis for standardization of morphometric parameters and optimization of preparation for invasive cardiac interventions [2, 9, 13, 36].

The aim of the study was to construct and analyze regression models of coronary sinus dimensions depending on anthropometric body parameters and other coronary sinus dimensions in patients without coronary artery pathology.

Materials and methods

A total of 24 middle-aged patients (15 men and 9 women; 44-60 years according to the age classification of the World Health Organization) without coronary artery pathology were examined. All patients underwent CT coronary angiography at the State Institution “Amosov National Institute of Cardiovascular Surgery of National Academy of Medical Sciences of Ukraine ” All examinations were conducted in accordance with generally accepted ethical standards, requirements for the protection of the rights, interests, and personal dignity of research participants, and the legislative regulations of Ukraine, as confirmed by the Protocol of the Meeting of the Biomedical Ethics Commission of the Ukrainian Medical Stomatological Academy (Protocol No. 171 dated 27.02.2019).

During CT coronary angiography, the following coronary sinus dimensions were measured (Fig. 1): KS_F – length of the coronary sinus from the ostium to the oblique vein of the atrium (mm); KS_G – transverse dimension of the coronary sinus at the ostium in the sagittal plane (mm); KS_H – transverse dimension of the coronary sinus at the ostium in the axial plane (mm); KS_I – transverse dimension of the coronary sinus in the middle third in the sagittal plane (mm); KS_J – transverse dimension of the coronary sinus in the middle third in the axial plane (mm); KS_K – transverse dimension of the coronary sinus at the level of the oblique vein of the atrium in the sagittal plane (mm); KS_L – transverse dimension of the coronary sinus at the level of the oblique vein of the atrium in the axial plane (mm). In addition, the anteroposterior chest dimension (GR_KL, mm) was determined on computed tomography images.

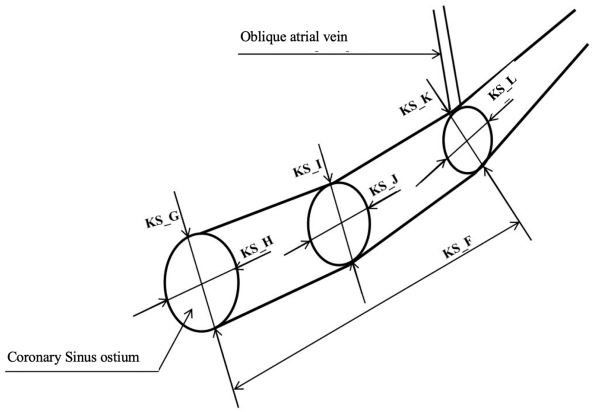

Fig. 1. Scheme for determining the dimensions of the coronary venous sinus.

Body weight was measured in all patients in the morning on an empty stomach (12 hours after the last meal) and after bowel evacuation using medical scales with an accuracy of 0.1 kg. Body height was measured using a stadiometer with an accuracy of 0.5 cm. Body mass index (BMI) was calculated using the formula: $BMI=m/h^2$, where m is body weight in kilograms and h is body height in meters. A BMI value <18.5 kg/m² indicates underweight; 18.5-24.9 kg/m² corresponds to normal body weight; 25.0-29.9 kg/m² indicates overweight; and ≥30.0 kg/m² is indicative of obesity [18].

Since statistically significant differences between men and women among body parameters and coronary sinus dimensions were established only for body weight and height, no separate sex-based stratification of variables was performed in modeling coronary sinus dimensions.

Regression models of coronary sinus dimensions were constructed using stepwise multiple regression analysis in the licensed software package “Statistica 6.0” [4].

Results

The constructed regression models of coronary sinus

dimensions depending on anthropometric body parameters in patients without coronary artery pathology are represented by the following linear equations:

length of the coronary sinus from the ostium to the oblique vein of the atrium = -32.15 + 0.458×GR_KL (R^2=0.468; $F_{(1.22)}$=19.32; p<0.001; Error of estimate=11.46);

transverse dimension of the coronary sinus at the ostium in the sagittal plane = -3.524 + 0.093×GR_KL (R^2=0.436; $F_{(1.22)}$=5.160; p<0.05; Error of estimate=4.520);

transverse dimension of the coronary sinus in the middle third in the sagittal plane = -13.17 + 0.038×GR_KL + 7.984×ROST (R^2=0.272; $F_{(2.21)}$=3.926; p<0.05; Error of estimate=1.979);

transverse dimension of the coronary sinus in the middle third in the axial plane = -5.710 + 0.058×GR_KL (R^2=0.464; $F_{(1.22)}$=19.08; p<0.001; Error of estimate=1.458);

transverse dimension of the coronary sinus at the level of the oblique vein of the atrium in the sagittal plane = -0.044 + 0.025×GR_KL (R^2=0.222; $F_{(1.22)}$=6.264; p<0.05; Error of estimate=1.118);

transverse dimension of the coronary sinus at the level of the oblique vein of the atrium in the axial plane = 0.976 + 0.017×GR_KL (R^2=0.122; $F_{(1.22)}$=3.068; p<0.093; Error of estimate=1.094);

here and hereafter, R^2 – coefficient of determination; $F_{(!.!!)}$=!!.!! – critical $_{(!.!!)}$ and calculated (!!.!!) values of the Fisher criterion; St. Error of estimate – standard error of the estimate.

A regression model for the *transverse dimension of the coronary sinus at the ostium in the axial plane* depending on anthropometric body parameters was not constructed.

We also constructed the following regression models of coronary sinus dimensions depending on other coronary sinus dimensions and anthropometric body parameters in patients without coronary artery pathology, expressed as the following linear equations:

length of the coronary sinus from the ostium to the oblique vein of the atrium = -24.35 + 0.435×GR_KL + 1.036×KS_G - 4.256×KS_L (R^2=0.681; $F_{(3.20)}$=14.23; p<0.001; Error of estimate=9.306);

transverse dimension of the coronary sinus at the ostium in the sagittal plane = -4.016 + 0.799×KS-H + 0.229×MAS - 2.018×IMT_1 (R^2=0.732; $F_{(3,20)}$=18.23; p<0.001; Error of estimate=2.726);

transverse dimension of the coronary sinus at the ostium in the axial plane = -7.662 + 0.593×KS_G + 3.166×SEX + 0.661×KS_J (R^2=0.736; $F_{(3.20)}$=18.60; p<0.001; Error of estimate=2.453);

transverse dimension of the coronary sinus in the middle third in the sagittal plane = 3.424 + 0.163×KS_G + 0.501×KS-J - 0.769×KS_L+ 0.501×KS_K (R^2=0.577; $F_{(4.19)}$=6.487; p<0.01; Error of estimate=1.585);

transverse dimension of the coronary sinus in the middle third in the axial plane = -5.747 + 0.050×GR-KL + 0.154×KS-H (R^2=0.579; $F_{(2.21)}$=14.41; p<0.001; Error of estimate=1.324);

transverse dimension of the coronary sinus at the level of the oblique vein of the atrium in the sagittal plane = 9.786 + 0.659×KS_L + 0.353×KS-I - 0.114×KS_H – 5.313×ROST (R^2=0.548; $F_{(4.19)}$=5.766; p<0.01; Error of estimate=0.917);

transverse dimension of the coronary sinus at the level of the oblique vein of the atrium in the axial plane = 2.193 + 0.481×KS_K (R^2=0.273; $F_{(1.22)}$=8.246; p<0.01; Error of estimate=0.996).

Discussion

Overall, most contemporary morphological studies indicate moderate positive correlations between the dimensions of the coronary venous sinus and general anthropometric parameters (height, weight, body surface area) [3, 24, 26]. In all six regression models constructed by us for coronary sinus dimensions in patients without coronary artery pathology based on anthropometric parameters, the coefficient of determination (R^2) ranged from 0.122 to 0.468. Thus, less than 50 % of the variability in coronary sinus dimensions can be explained by the studied body parameters, and therefore these models do not have substantial practical significance. This confirms the conclusion that general anthropometric indicators cannot fully replace anatomical imaging for clinical decision-making [8, 9, 16].

All constructed models included the anteroposterior chest dimension, and only in one case was body height included. This emphasizes that thoracic measurements may provide additional information regarding cardiac topography within the thoracic cavity and the relationship of cardiac structures to the musculoskeletal framework, which is not reflected by other anthropometric parameters. Other studies have also highlighted the importance of thoracic anatomy for predicting cardiac structural morphology; however, direct comparative data between the anteroposterior chest dimension and coronary venous sinus dimensions have not yet been identified [2, 21].

Of the seven possible models, we constructed six statistically significant regression models of coronary sinus dimensions in patients without coronary artery pathology based on other coronary sinus dimensions and anthropometric body parameters, with coefficients of determination greater than 0.5 (R^2=0.548-0.736). This indicates that combined models incorporating additional coronary venous sinus measurements provide substantially better prediction of its morphology, supporting the feasibility of applying these models in clinical practice for predicting morphometric characteristics of this structure. The most frequently included variables in the constructed models were the transverse dimension of the coronary sinus at the ostium in the sagittal and axial planes, the transverse dimension at the level of the oblique vein of the atrium in the axial plane (15.0 % each), as well as the transverse dimension in the middle third in the axial plane, the transverse dimension at the level of the oblique vein of the atrium in the sagittal plane, and the anteroposterior chest dimension (10.0 % each). Only the regression model for the transverse dimension of the coronary sinus at the level of the oblique vein of the atrium in the axial plane demonstrated

a coefficient of determination of 0.273 and therefore lacks substantial practical significance. This may be explained by anatomical features of this region, relatively high variability of individual parameters that correlate weakly with general body dimensions, as well as technical aspects of measurement in this area, for example sensitivity to the phase of the reconstruction cycle in CT imaging [24, 26, 34].

Our results confirm the importance of selecting an appropriate imaging modality. Among measurement techniques, most researchers prefer contrast-enhanced CT due to its superior spatial resolution and the possibility of constructing three-dimensional volumetric images and measurements. Studies based on cadaveric material do not allow adequate assessment of the spatial structure of the coronary venous sinus due to the absence of physiological tissue turgor [6, 12, 15, 32].

It should be noted that, according to many researchers, there is currently a lack of clearly unified standards worldwide for measuring the morphology of the coronary venous sinus [14].

Conclusions

1. All constructed regression models (6 out of 7 possible) of coronary sinus dimensions in patients without coronary artery pathology based on anthropometric parameters have a coefficient of determination less than 0.5 and therefore do not have substantial practical significance. The anteroposterior chest dimension was included in all constructed models.

2. Of the 7 possible models, 6 statistically significant regression models of coronary sinus dimensions in patients without coronary artery pathology based on other coronary sinus dimensions and anthropometric body parameters were constructed, with coefficients of determination ranging from 0.548 to 0.736. In most cases, the constructed models included other coronary sinus dimensions as predictor variables.

References

[1] Agarwal, J., Agarwal, A., Sinha, D. N., & Kumar, V. (2020). Morphological study of middle cardiac vein in human hearts of north western UP and its application for interventional procedure. *Indian Journal of Clinical Anatomy and Physiology, 7*(2), 130-133. doi: 10.18231/j.ijcap.2020.027

[2] Alkhouli, M., Lurz, P., Rodes-Cabau, J., Gulati, R., Rihal, C. S., Lerman, A., & Latib, A. (2022). Transcatheter coronary sinus interventions. *Cardiovascular Interventions, 15*(14), 1397-1412. doi: 10.1016/j.jcin.2022.05.039

[3] Amoozgar, H., Bazyari, V., Edraki, M., Mehdizadegan, N., Mohammadi, H., Naghshzan, A., … & Hajian, T. (2021). Age-adjusted reference values and Z-scores of the coronary sinus diameter among healthy children and adolescents in Southern Iran. *Arch Iran Med, 24*(11), 804-810. doi: 10.34172/aim.2021.120

[4] Antomonov, M. Yu. (2018). *Математическая обработка и анализ медико-биологических данных [Mathematical processing and analysis of medical and biological data]*. К.: МИЦ “Мединформ” – К.: Medical Center “Medinform”.

[5] Arunachalam, K. (2016) Coronary Sinus Anatomy and its Importance-evidence based Review. *Anat Physiol, 6*(2), 207. doi: 10.4172/2161-0940.1000207

[6] Azizova, A., Onder, O., Arslan, S., Ardali, S., & Hazirolan, T. (2020). Persistent left superior vena cava: clinical importance and differential diagnoses. Insights into Imaging, *11*(1), 110. doi: 10.1186/s13244-020-00906-2

[7] Bai, W., Xu, X., Ma, H., Zhong, L., Xie, H., Sun, C., … & Yang, J. (2020). Assessment of the Relationship Between the Coronary Venous and Arterial Systems Using 256-Slice Computed Tomography. *J Comput Assist Tomogr, 44*(1), 1-6. doi: 10.1097/RCT.0000000000000949

[8] Barchitta, A., Rossitto, G., Ruzza, L., Maio, D., Scaparotta, G., Bagordo, D., ... & Rossi, G. P. (2023). Coronary sinus diameter to estimate congestion and predict survival. *IJC Heart & Vasculature, 49*, 101294. doi: 10.1016/j.ijcha.2023.101294

[9] Borgquist, R., & Wang, L. (2022). Anatomy of the coronary sinus with regard to cardiac resynchronization therapy implantation. *Herzschrittmachertherapie + Elektrophysiologie, 33(2)*, 186-194. doi: 10.1007/s00399-022-00863-x

[10] Chauhan, A. J., & Kothari, R. J. (2024). Coronary sinus anomalies with case illustrations. *Journal of the Indian Academy of Echocardiography & Cardiovascular Imaging, 8*(3), 171-176. doi: 10.4103/jiae.jiae_13_24

[11] Dar, M. I., Lone, A. A., Hafeez, I., Tahir, S. M., Sheikh, J. M., Bilal, S., & Rather, H. A. (2025). Resynchronization Therapy in a Coronary Venous Sinus Anomaly. *Case Reports, 30*(22), 104576. doi: 10.1016/j.jaccas.2025.104576

[12] Dila, D. (2022). In anatomy, the coronary sinus is a collection of veins joined together to form a large vessel. *Interventional Cardiology Journal, 8*(10), 46. doi: 10.21767/2471-8157.8.10.46

[13] Gach-Kuniewicz, B., Goncerz, G., Ali, D., Kacprzyk, M., Zarzecki, M., Loukas, M., … & Mizia, E. (2023). Variations of coronary sinus tributaries among patients undergoing cardiac resynchronisation therapy. *Folia Morphologica, 82*(2), 282-290. doi: 10.5603/FM.a2022.0044

[14] Gensini, G. G., Di Giorgi, S., Coskun, O., Palacgo, A., & Kelly, A. E. (1965). Anatomy of the coronary circulation in living man: Coronary venography. *Circulation, 31*(5), 778-784. doi: 10.1161/01.CIR.31.5.7

[15] Gokhroo, R. K., Bisht, D. S., Padmanabhan, D., & Gupta, S. (2014). Coronary sinus anatomy: Ajmer Working Group Classification. *The Journal of Invasive Cardiology, 26*(2), 71-74. PMID: 24486664

[16] Hily, M., Bessières, B., Bonnet, D., & Houyel, L. (2024). An exceptional anomaly of the coronary venous drainage: anatomic description. *Cardiology in the Young, 34*(10), 2100-2104. doi: 10.1017/S1047951124025423

[17] Kassem, M., Lake, S., Roberts, W., Salandy, S., & Loukas, M. (2021). Cardiac veins, an anatomical review. *Translational Research in Anatomy, 23*, 100096. doi: 10.1016/j.tria.2020.100096

[18] Kataoka, K. (1995). Indices of obesity derived from body weight and height. *Nihon rinsho. Japanese Journal of Clinical Medicine, 53*, 147-153. PMID: 7563679

[19] Keiler, J., Meinel, F. G., Ortak, J., Weber, M. A., Wree, A., & Streckenbach, F. (2020). Morphometric Characterization of Human Coronary Veins and Subvenous Epicardial Adipose Tissue-Implications for Cardiac Resynchronization Therapy Leads. *Frontiers in Cardiovascular Medicine, 7*, 611160. doi: 10.3389/fcvm.2020.611160

[20] Kumar, M., Priti, B., Kumar, A., & Ranjan, R. (2024). Metri-

cal analysis of coronary sinus in human heart. *International Journal of Life Sciences, Biotechnology and Pharma Research, 13*(5), 470-476.

[21] Lin, F., Wang, Q., Meng, L., Liang, Y., Kong, X., Wei, K., … & Gu, X. (2023). Cardiac computed tomography based analysis of mitral annulus, coronary sinus and left circumflex artery in patients with mitral regurgitation: Implications for transcatheter mitral annuloplasty techniques. I*nternational Journal of Cardiology, 375*, 57-65. doi: 10.1016/j.ijcard.2023.01.023

[22] Mahato, P. K., & Singh, S. (2023). Morphometry of coronary sinus and its role in cardiac cannulation. *Journal of Population Therapeutics and Clinical Pharmacology, 30*(19), 2092-2095. doi: 10.53555/jptcp.v30i19.4624

[23] Mishra, R., Khan, K., Diwan, R. K., & Anwar, F. (2024). Exploring the coronary sinus in the cadaveric heart: A morphological and morphometric analysis. *African Journal of Biomedical Research, 27*(3S), 491-495. doi: 10.53555/AJBR.v27i3S.2031

[24] Młynarska, A., & Młynarski, R. (2024). Possibility to measure the volume of coronary sinus in contrast-enhanced computed tomography. *Polish Journal of Radiology, 89*, e428-e432. doi: 10.5114/pjr/191535

[25] Mlynarski, R., Mlynarska, A., Golba, K., & Sosnowski, M. (2020). Vein of Marshall visualization in cardiac computed tomography. *European Heart Journal, 41*(2), doi: 10.1093/ehjci/ehaa946.0161

[26] Mlynarski, R., Mlynarska, A., & Stasiow, B. (2021). Temporal changes of the diameter of the coronary sinus during the cardiac cycle. *Clin Physiol Funct Imaging, 41*(2), 192-198. doi: 10.1111/cpf.12685

[27] Ortale, J. R., Gabriel, E. A., Iost, C., & Marquez, C. Q. (2001). The anatomy of the coronary sinus and its tributaries. *Surgical and Radiologic Anatomy, 23*(1), 15-21. doi: 10.1007/s00276-001-0015-0

[28] Pushpakala, K., & Vidulatha, K. (2020). A study of the tributaries of the coronary sinus. *Journal of Medical Science and Clinical Research, 8*(3), 140-144. doi: 10.18535/jmscr/v8i3.22

[29] Rottlander, D., Saal, M., Ogutcu, A., Degen, H., & Haude, M. (2022). Anatomy and topography of coronary sinus and mitral valve annulus in functional mitral regurgitation. *Front Cardiovasc Med, 9*, 868562. doi: 10.3389/fcvm.2022.868562

[30] Silva, L. A. A., Meira, E. B. de S., Curimbaba, J., & Pimenta, J. A. (2020). Coronary sinus phlebography in cardiac resynchronization therapy patients: Identifying and solving demanding cases. *Journal of Innovations in Cardiac Rhythm Management, 11*(7), 4161-4170. doi: 10.19102/icrm.2020.110703

[31] Sirajuddin, A., Chen, M. Y., White, C. S., & Arai, A. E. (2020). Coronary venous anatomy and anomalies. *Journal of Cardiovascular Computed Tomography, 14*(1), 80-86. doi: 10.1016/j.jcct.2019.08.006

[32] Sławek-Szmyt, S., Szmyt, K., Żaba, C., Grygier, M., Lesiak, M., & Araszkiewicz, A. (2021). Peculiarities in coronary sinus anatomy: Implications for successful cannulation from an autoptic study. *EP Europace, 23*(11), 1787-1794. doi: 10.1093/europace/euab108

[33] Sun, L., Juan, Y.-H., Chen, J., Zhuang, J., Xie, J., Li, H., & Liu, H. (2018). Evaluation of unroofed coronary sinus syndrome using cardiovascular CT angiography: An observational study. *AJR. American Journal of Roentgenology, 211*(2), 314-320. doi: 10.2214/AJR.17.19128

[34] Takagi, T., Derval, N., Pambrun, T., Nakatani, Y., Andre, C., Ramirez, F., ... & Cochet, H. (2022). Optimized computed tomography acquisition protocol for ethanol infusion into the vein of marshall. *J Am Coll Cardiol EP, 8*(2), 168-178. doi: 10.1016/j.jacep.2021.09.020

[35] Wilson, A., & Bhutta, B. (2001). *Anatomy, Thorax, Coronary Sinus*. Treasure Island (FL): StatPearls Publishing. https://www.ncbi.nlm.nih.gov/books/NBK557566/

[36] Zehan, I. G., Eötvös, C. A., Moldovan, M. P., Andrei, M. G., Șchiop-Țentea, C. P., Lazar, R. D., … & Blendea, D. (2025). Angiographic anatomy of the left coronary veins: Beyond conventional cardiac resynchronization therapy. *Current Cardiology Reports, 27(1)*, 58. doi: 10.1007/s11886-025-02204-z

МОДЕЛЮВАННЯ РОЗМІРІВ КОРОНАРНОГО СИНУСА ЗА ДОПОМОГОЮ РЕГРЕСІЙНОГО АНАЛІЗУ У ПАЦІЄНТІВ БЕЗ ПАТОЛОГІЇ КОРОНАРНИХ АРТЕРІЙ

Білаш С. М., Люлька Є. М., Баранніков К. В., Проніна О. М., Шостя А. М., Коптев М. М., Пирог-Заказнікова А. В., Олійніченко Я. О., Донченко С. В., Олексієнко В. В., Мамай О. В.

На відміну від детально вивченої анатомії артеріальної системи серця, венозна система залишалась на другому плані в колі інтересу дослідників. Проте за останні роки у світі значно збільшився спектр хірургічних операцій та маніпуляцій із задіянням венозної системи серця, таких як інвазивні електрофізіологічні дослідження, імплантація електродів для стимуляції лівих відділів серця, тощо. Мета роботи – побудувати та провести аналіз регресійних моделей розмірів коронарного синуса в залежності від антропометричних параметрів тіла та інших розмірів коронарного синуса у пацієнтів без патології коронарних артерій. Проведено обстеження 24 пацієнтів (15 чоловіків і 9 жінок) середнього віку (44-60 років відповідно до вікової класифікації Всесвітньої організації охорони здоров'я) без патології коронарних артерій, котрим виконували КТ-коронарографію на базі ДУ «Національний інститут серцево-судинної хірургії ім. М. М. Амосова НАМН України». До дослідження були включені пацієнти, у котрих не було клінічних проявів ішемічної хвороби серця. Всім пацієнтам проводили мультиспіральну комп'ютерну томографію серця з контрастуванням (КТ-коронарографія) з оцінкою анатомічних параметрів коронарного венозного синуса під час венозної фази контрастування. Як незалежні змінні до моделі були введені демографічні (вік, стать), антропометричні (маса тіла, зріст) та кардіометричні показники. Для визначення найбільш значущих чинників використовували множинний лінійний регресійний аналіз проведений в ліцензійному пакеті «Statistica 6.0». В усіх шести побудованих моделях розмірів коронарного синуса у пацієнтів без патології коронарних артерій в залежності від антропометричних показників коефіцієнт детермінації (R^2) дорівнює від 0,122 до 0,468. Тобто величина розмірів коронарного синуса менше ніж на 50 % залежить від параметрів тіла, що вивчали і тому дані моделі не мають важливого практичного значення. До усіх побудованих моделей входить передньо-задній розмір грудної клітки та лише в одному випадку – довжина тіла. В 6 достовірних моделях розмірів коронарного синуса у

пацієнтів без патології коронарних артерій в залежності від інших розмірів коронарного синуса та антропометричних параметрів тіла коефіцієнт детермінації дорівнює від 0,548 до 0,736. До побудованих моделей найчастіше входять: поперечний розмір коронарного синуса в ділянці гирла у сагітальній та в аксіальній площинах, а також поперечний розмір коронарного синуса на рівні косої вени передсердя в аксіальній площині (по 15,0 %). Дані моделі можуть бути використані у клінічній практиці для індивідуалізованої передопераційної оцінки анатомії венозної системи серця. Запропонований метод регресійного моделювання розмірів коронарного синуса забезпечує можливість неінвазивного прогнозування його параметрів у пацієнтів без патології коронарних артерій, що сприяє підвищенню точності планування інвазивних та інтервенційних кардіологічних втручань.

Ключові слова: *коронарний синус, КТ-коронарографія, морфометрія, антропометрія, чоловіки та жінки без патології коронарних артерій.*

Author's contribution

Bilash S. M. – conceptualization, research, review writing and editing, supervision.
Liulka Ye. M. – conceptualization, research, review writing and editing, methodology and writing of the original draft.
Barannikov K. V. – supervision, formal analysis and validation, project administration.
Pronina O. M. – research, supervision, formal analysis and validation, project administration, supervision.
Shostya A. M. – supervision, formal analysis and validation, project administration.
Koptev M. M. – data visualization, resources.
Pirog-Zakaznikova A. V. – data visualization, resources.
Oliinichenko Ya. O. – data visualization, resources.
Donchenko S. V. – resources, software.
Oleksiienko V. V. – resources, software.
Mamai O. V. – resources, software.

DOI: 10.31393/morphology-journal-2026-32(1)-03

Reports of Morphology, Vol. 32, №1, Pages 19-25

ISSN 1818-1295 eISSN 2616-6194

REPORTS OF MORPHOLOGY

Official Journal of the Scientific Society of Anatomists, Histologists, Embryologists and Topographic Anatomists of Ukraine

journal homepage: https://morphology-journal.com

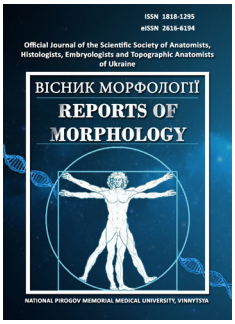

Microscopic and morphometric changes in the bronchi and lung parenchyma of laboratory rats three hours after administration of Leiurus macroctenus scorpion venom

Gunas V. I.[1], Maievskyi O. Ye.[2], Skoruk R. V.[1], Kyrychenko V. I.[1], Bandurka N. M.[1], Sorokoumov V. P.[1], Gunas I. V.[1]

[1] National Pirogov Memorial Medical University, Vinnytsya, Ukraine

[2] Educational and Scientific Center "Institute of Biology and Medicine", Taras Shevchenko National University of Kyiv, Kyiv, Ukraine

ARTICLE INFO

Received: 15 July 2025

Accepted: 3 December 2025

UDC: 616.514-037:572.087+612-071

CORRESPONDING AUTHOR

e-mail: freekozak1@gmail.com

Gunas V. I.

CONFLICT OF INTEREST

The authors have no conflicts of interest to declare.

FUNDING

Not applicable.

DATA SHARING

Data are available upon reasonable request to corresponding author.

Scorpionism is a widespread phenomenon occurring in various regions of the world and poses particular danger to elderly individuals and children. Despite numerous cases of scorpion venom exposure in humans, only a limited number of publications describe the clinical picture, especially regarding respiratory system involvement. Even fewer studies address morphological changes in the lungs or bronchi of deceased individuals or laboratory animals, particularly at different time intervals after a scorpion sting. These gaps at the morphological level, even with a relatively well-studied pathogenetic mechanism of scorpion venom action, do not allow for a complete understanding of its toxic effects. Only through comprehensive investigation of the venom is it possible not only to develop effective antivenoms but also to explore its potential as a promising therapeutic agent. The aim of the study was to determine microscopic and morphometric changes in the bronchi and lung parenchyma of rats three hours after administration of Leiurus macroctenus scorpion venom. Ten male rats maintained under vivarium conditions were used and divided into two groups of five animals each: group 1 (control) received physiological saline, and group 2 received scorpion venom at a dose of 28.8 μg/ml. Three hours after administration, the animals were euthanized and the lungs were collected for histological examination. For microscopic and morphometric analysis, 4-5 μm sections (stained with hematoxylin-eosin and Azan Trichrome) and semi-thin sections of 1-2 μm (stained with methylene blue) were prepared. Microscopy was performed at magnifications ranging from ×40 to ×1000 using an OLIMPUS BX 41 microscope. Morphometric analysis was conducted using Quickphoto Micro 2.3 software. Statistical analysis of the results was performed using the licensed software package "Statistica 6.0" with nonparametric methods. Three hours after venom administration, pronounced inflammatory changes developed in the lungs of experimental animals, manifested by massive lymphocytic-neutrophilic infiltration, most intense around medium- and small-diameter bronchi and bronchioles, up to partial destruction of their walls, fragmentation of muscle bundles, and adventitial edema. The interalveolar space was dominated by basophils, eosinophils, and macrophages, indicating a marked inflammatory response. In the parenchyma, areas of distelectasis alternated with emphysematous regions, where focal destruction of interalveolar septa and fluid accumulation were observed. Morphometric analysis demonstrated a decrease in alveolar width, alveolar entrance width, and alveolar depth (p=0.112, p=0.008, and p=0.174, respectively), as well as a statistically significant narrowing of the conducting portion of respiratory bronchioles (p=0.045). A tendency toward redistribution of air between the alveolar and bronchiolar compartments was identified, reflected histologically by changes in morphometric ratios. The obtained data indicate the development of acute inflammatory-destructive lung injury with impaired ventilatory function already at early stages after intoxication. The combination of observed microscopic changes suggests the formation of structural remodeling of the lung parenchyma as early as three hours after venom administration in laboratory animals.

Keywords: *morphology, scorpion venom, Leiurus macroctenus, rats, bronchi, lung parenchyma, morphological changes, morphometric changes.*

Introduction

Climate-driven shifts in environmental processes have led to an expansion of the distribution range of scorpion species that are dangerous to humans. Thus, scorpions of the genus Tityus, whose range is represented in South America, have shown that over 20 years, in a number of regions the number of scorpionism cases increased by 20 %, and in some regions of Argentina by 30-50 %. According to scientists, this was a consequence of an increase in regional temperature by 1-1.5 °C. In particular, in Argentina a trend toward an increase in scorpionism cases specifically in cities has been noted, which poses an additional hazard [2]. In particular, Tityus carrilloi, which was previously considered endemic to Argentina, has already spread into Paraguay, representing a serious challenge to that country's health care system, as the venom of this scorpion has pronounced neurotoxic activity [4].

Similar results were obtained in another study, where scientists predict that by 2070 the distribution range of the scorpion T. metuendus in Brazil will increase, posing a danger to the Indigenous peoples of this country, who usually suffer from scorpionism incidents 2.4 times more often and have a child mortality rate 10 times higher [7]. The use of artificial intelligence to create a predictive model of scorpion distribution in Brazil supplemented and confirmed these data as well [8].

Globally, the number of scorpion stings has reached 1 million per year, with rates of 100-300 cases per 100,000 population in certain regions. Case fatality is estimated at 0.2-0.5 % [3].

A particular concern is the fact that scorpions even within the same region can have different venom composition, which is explained by substantial proteomic diversity. This further complicates the management of scorpionism cases, given the frequent unavailability of antivenom in rural areas [5].

Morocco is one of the countries that suffers considerably from scorpionism. From 2021 to 2024, 2,206 cases were recorded there, of which 41 were fatal. Notably, most cases were recorded at home [10]. Data from Algeria show that scorpion stings are also increasing there: the annual number of cases averages 585.8 per 100,000 population. In 2019, the highest rate was recorded 694.8 per 100,000. Over the observation period from 2018 to 2024, 10 deaths were recorded [23].

In Brazil, the number of cases is steadily increasing from 66,986 in 2014 to 170,616 in 2023. Predictive models show that the number of scorpionism cases will rise to 274,246 in 2033. According to the authors, a key role in this is played by the scorpion species Tityus serrulatus, individuals of which can survive 400 days without food and are capable of reproducing without the participation of males [21].

Thus, scorpionism is a widespread and dangerous phenomenon, because scorpion venom varies markedly by species and is often a mixture of neurotoxins, cardiotoxins, nephrotoxins, and hemolytic toxins that affect different organ systems [25]. There is a need for morphological studies of venom effects on the main target organs, which will allow assessment of the possibility of developing appropriate pharmacotherapy.

The aim of the study was to determine microscopic and morphometric changes in the bronchi and lung parenchyma of rats three hours after administration of Leiurus macroctenus scorpion venom.

Materials and methods

The study was conducted on 10 white laboratory rats weighing 200±10 g, which were bred and maintained in a certified vivarium in accordance with the "Standard Rules for the Arrangement, Equipment, and Maintenance of Experimental Biological Clinics (Vivaria)" (vivarium of the Educational and Scientific Center "Institute of Biology and Medicine" of Taras Shevchenko National University of Kyiv) on a standard diet with free access to water and a 12-hour light cycle. The animals were divided into two groups of 5 animals each. Group 1 – control group, which received physiological saline. Group 2 – experimental group, which received a single intramuscular injection of Leiurus macroctenus scorpion venom solution at a concentration of 28.8 μg/ml in a dose of 0.5 ml (venom diluted in physiological saline) calculated according to LD50=0.08 mg/kg for this species [12]. Three hours after venom administration, the rats were euthanized by CO_2 inhalation. The lungs were removed at +4 °C immediately after euthanasia.

Venom was obtained by milking 15 sexually mature Leiurus macroctenus scorpions bred in captivity, which had been maintained for one year on a standard diet of Shelfordella lateralis cockroaches with free access to distilled water. The scorpions were kept under standard conditions at a temperature of 25-35 °C, humidity of 50-60 %, and natural lighting, with adequate ventilation provided in the terrariums. The milking procedure was performed once according to the method of Ozkan Ö. and Filazi A. [20] as modified by Yaqoob R. et al. [27], by applying an electrode to the prosoma and tail segment of an immobilized scorpion, with an electric current of 24 V applied for 5 seconds. The collected venom was stored at -20 °C.

The study was carried out in accordance with current regulations governing work with laboratory animals and in compliance with the "European Convention for the Protection of Vertebrate Animals Used for Experimental and Other Scientific Purposes," as well as the Law of Ukraine No. 3447-IV dated 21.02.2006 "On the Protection of Animals from Cruelty".

Part of the lung samples was fixed in 10 % neutral formalin, followed by dehydration in alcohols of increasing concentration, processing using a Logos ONE tissue processor (MILESTONE, Italy), and embedding in paraffin blocks using an automatic station TEC 2800 (HESTION, Australia). Serial sections 4-5 μm thick were then prepared using an AMR-400 rotary microtome (Amos Scientific Pty, Australia). The sections were stained with hematoxylin-

eosin and by the Azan Trichrome method. Another portion of the samples was fixed in 2.5 % glutaraldehyde solution (pH 7.3-7.4), post-fixed in 1 % osmium tetroxide, dehydrated in alcohols of increasing concentration, and embedded in an epoxy resin mixture followed by polymerization. Semi-thin sections 1-2 μm thick were prepared from these samples. The sections were cut using an Ultratome LKB 4801 A ultramicrotome (Bromma, Sweden) and stained with methylene blue.

Section analysis was performed using an OLIMPUS BX 41 light microscope at magnifications ×40, ×100, ×200, ×400, ×800, and ×1000. Image acquisition and morphometric analysis were carried out using Quickphoto Micro 2.3 software. The morphometric parameters studied included alveolar width, alveolar depth, alveolar entrance width, width of the conducting portion of the respiratory bronchiole, mean thickness of the interalveolar septum, the ratio of alveolar entrance width to alveolar depth (ratio A), and the ratio of the conducting portion width of the respiratory bronchiole to alveolar depth (ratio B).

Statistical analysis of the obtained results was performed using the licensed software package “Statistica 6.0” with nonparametric evaluation methods. Distribution characteristics of each variation series, mean values, and standard deviations were assessed. The significance of differences between independent quantitative variables was determined using the Mann–Whitney U test.

Results

In the lungs of rats administered Leiurus macroctenus scorpion venom, massive areas of lymphocytic-neutrophilic infiltration are observed three hours after injection. These changes are most pronounced around medium- and small-diameter bronchi and bronchioles, in some areas leading to partial destruction of their walls. Foci of lipocyte accumulation are also noted, predominantly located near sites of inflammatory infiltration. In the muscular layer of certain bronchi, disruption of its continuous structure is observed due to fragmentation of muscle bundles. In addition, marked adventitial edema is present in these bronchi (Figs. 1, 2).

In the interalveolar space, basophils and eosinophils predominate, containing numerous granules of varying optical density. Basophils exhibit abundant cytoplasm filled with large transparent vesicles and optically dense granules, and their nuclei are bilobed. Eosinophils also possess bilobed nuclei, although cells with bean-shaped nuclei are observed. Their cytoplasm is densely packed with numerous small granules. Macrophages are also identified, with cytoplasm completely filled with relatively large transparent phagolysosomes, indicating high phagocytic activity. Some of these cells lack nuclei, while others show reduced nuclei, which may suggest incomplete phagocytosis (Fig. 3).

Areas of lung tissue consolidation are observed due to collapse of alveolar walls. At the same time, regions of alveolar dilation are noted, followed by destructive changes in their walls and accumulation of fluid (Fig. 4).

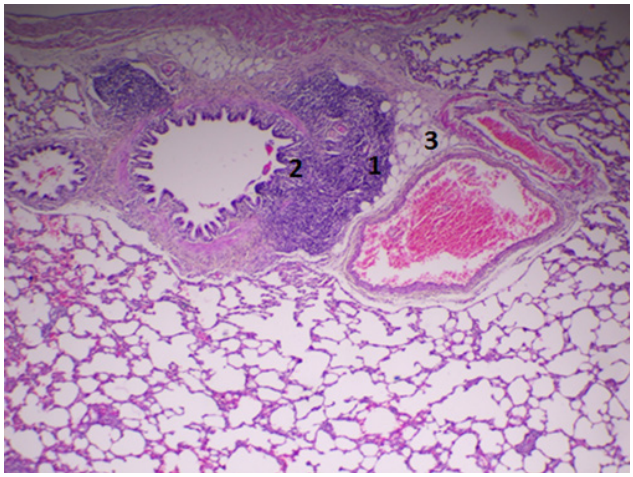

Fig. 1. Fragment of rat lung three hours after administration of Leiurus macroctenus scorpion venom. 1 – lymphocytic-neutrophilic infiltration; 2 – destroyed bronchiolar wall; 3 – lipocytes. Hematoxylin-eosin staining. Magnification ×40.

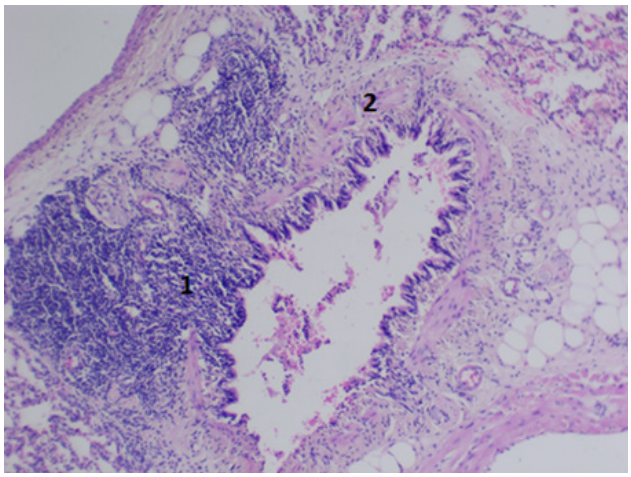

Fig. 2. Fragment of rat lung three hours after administration of Leiurus macroctenus scorpion venom. 1 – lymphocytic–neutrophilic infiltration; 2 – fragmented muscular layer of the bronchus. Hematoxylin-eosin staining. Magnification ×40.

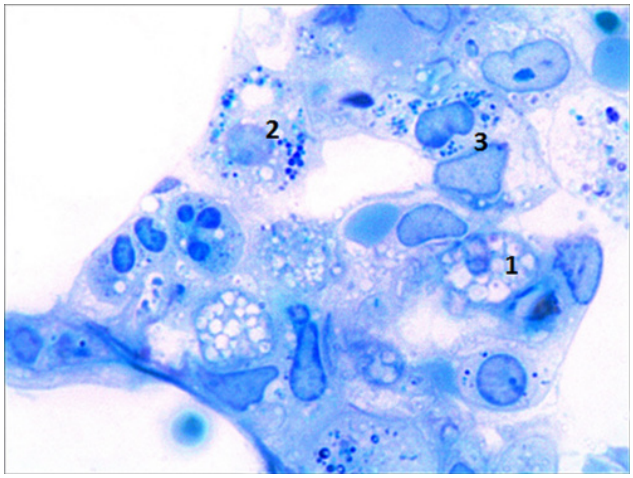

Fig. 3. Fragment of rat lung three hours after administration of Leiurus macroctenus scorpion venom. 1 – macrophage with phagolysosomes; 2 – eosinophil; 3 – basophil. Methylene blue

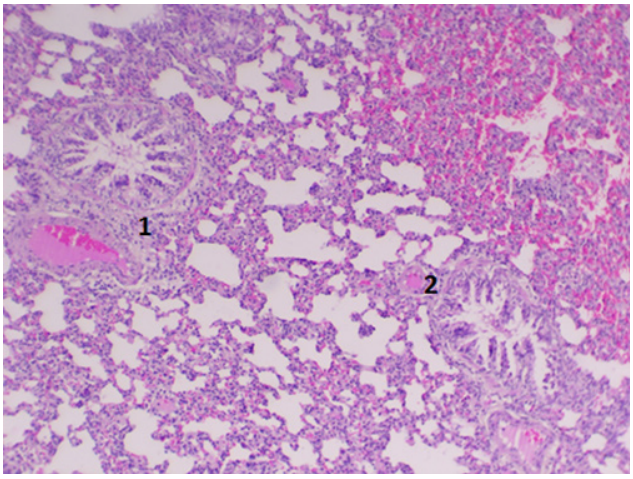

Fig. 4. Fragment of rat lung three hours after administration of Leiurus macroctenus scorpion venom. 1 – stromal edema; 2 – arteriole. Hematoxylin-eosin staining. Magnification ×40.

Morphometric analysis of the specimens demonstrated progression of a general trend toward redistribution of air between the alveoli and the conducting portion of the respiratory bronchioles. This was reflected by a decrease in alveolar width to 47.29±11.31 μm, alveolar entrance width to 27.50±4.01 μm, and alveolar depth to 68.72±9.50 μm, which were 21.35 % (p=0.112), 23.89 % (p=0.008), and 5.68 % (p=0.174) lower than control values, respectively. The mean thickness of the interalveolar septum was only 0.67 % lower (p=0.406) than in the control group. The width of the conducting portion of the bronchiole three hours after venom administration was 55.22±4.39 μm, which was statistically significantly 7.36 % lower than the control value (p=0.045).

The ratio of alveolar entrance width to alveolar depth (ratio A) and the ratio of the conducting portion width of the respiratory bronchiole to alveolar depth (ratio B) three hours after venom administration were 0.407±0.082 and 0.817±0.125, respectively, which were 22.77 % (p=0.112) and 3.31 % (p=0.940) lower compared to the control group.

Discussion

Thus, three hours after administration of Leiurus macroctenus scorpion venom, progressive edema was observed in the rat lungs, predominantly affecting the pulmonary stroma, along with infiltration of the interstitial space by inflammatory cells, which may impair tissue trophism and gas exchange processes. A continuing trend toward redistribution of air between the alveoli and the conducting portion of the respiratory bronchioles was noted, manifested by decreased alveolar width and entrance depth, consolidation of lung tissue, and collapse of alveolar walls. At the same time, areas of alveolar dilation were observed, accompanied by subsequent destructive changes of their walls and accumulation of fluid.

Studies describing lung morphology under the action of animal venoms are few in number, and they often concern snake venoms [1, 9, 13]. Thus, observation of groups of mice injected with the venom of the snake Crotalus durissus cascavella at a dose of 50 μg/kg showed different microscopic patterns at 1, 3, 6, 12, 24, and 48 h after administration. After 1 h, thickening of the interalveolar septa and marked vascular congestion were observed, with the appearance of a round-cell infiltrate, which by 3 h had already extended to the interalveolar septa with the formation of emphysema and disatelectasis. After 6 h, the infiltration decreased, but other changes persisted or progressed, and bronchial changes appeared which at 24-48 h caused bronchiolar spasm. Hemorrhages also appeared [1]. Other authors also studied the venom of this snake species, but administered it at a lower dose, 3.0 μg/kg. They found agreement between the macroscopic picture, manifested by impaired respiratory function, and the histological picture of lung injury acute parenchymal damage with a combination of atelectasis, emphysema, hemorrhages, round-cell infiltrate, edema, and vascular stasis [9].

A study of the effects of Vipera berus berus and Vipera berus nikolskii venom on lung morphometric parameters found that, compared with the control group (rats injected with saline), the mean vascular area in the lung increased 1.31-fold relative to intact animals, while the mean “respiratory compartment” index decreased to 0.8. The relative areas of disatelectasis, atelectasis, and emphysematous changes increased 6.03-, 7.15-, and 2.0-fold, respectively, compared with controls [16, 17].

Administration of Pseudechis papuanus venom at a dose of 35 μg after 40-60 min causes pulmonary edema in mice with massive accumulation of “hyaline” (proteinaceous) material in the alveolar spaces. At the same time, administration of the venom at a dose of 15 μg does not lead to the appearance of any microscopic changes in the lungs [26].

Comparison of morphological changes after administration of the venoms of the scorpions Tityus serrulatus and T. bahiensis at a dose of 200 μg/kg showed that in both cases laboratory animals exhibited marked hemorrhages, an inflammatory reaction, and an increased number of white blood cells in the bronchi and bronchioles [19].

A histological study of the effects of two Moroccan scorpion venoms showed that there is a correlation between the severity of the pathomorphological manifestations of venom action and its LD_{50}. At different time intervals, the authors noted dilation of alveolar spaces and destruction of alveolar structures in experimental animals [6].

Only isolated studies address the morphological impact of Leiurus macroctenus scorpion venom. In particular, available results concern changes in the adrenal glands of rats. One day after venom administration, pronounced changes in adrenal structure were detected, with hemorrhages and vascular congestion in this organ, indicating a systemic effect of the venom of this scorpion species [15]. Same microscopic changes were observed during kidneys investigation. Three hours after administration of Leiurus macroctenus venom intensive polymorphonuclear infiltration and disruption of blood vessels were found. Tubular necrosis appears in

kidneys tubular system [18].

A systematic review of 12 autopsy cases after scorpion stings was conducted by a team of researchers, who found that although the changes were nonspecific, they were uniform: the lungs showed signs of marked blood congestion and edema, which microscopically manifested as hemosiderophages in the alveoli, atelectasis, disatelectasis, edema (eosinophilic proteinaceous material), and subpleural emphysema [11].

A study of the effect of Tityus serrulatus scorpion venom on the bronchial epithelial cell line BEAS-2B showed that exposure to the venom at concentrations of 10 and 50 μg/mL for 1, 3, 6, and 24 h reduced cell viability, and cell death occurred through necrosis rather than apoptosis, as indicated by cytometry results [22].

Androctonus australis hector scorpion venom, when administered to laboratory animals at a dose of 10 μg/20 g, causes acute lung injury with involvement of alveolar macrophages and neutrophils (in particular, around the bronchi), occurring against a background of areas of edema and hemorrhages [24].

At the same time, bee venom, conversely, may have a positive effect on the morphological structure of the lungs. An experimental study showed that its venom can block IL-13-induced upregulation of MUC5AC [14].

Overall, comparison of data on the effects of scorpion venoms with the obtained results showed partial overlap in the morphological picture. The differences are likely the result of both different experimental models and species-specific features of venom composition.

Conclusions

1. Three hours after administration of Leiurus macroctenus venom, acute inflammatory-destructive lung injury develops in experimental animals, combining pronounced round-cell infiltration, structural damage to bronchi of various calibers, and reactive changes in the parenchyma.

2. Morphometric analysis demonstrated a reduction in the examined alveolar parameters, including statistically significant narrowing of the conducting portion of the respiratory bronchioles (p=0.045) and the alveolar entrance width (p=0.008), indicating impaired ventilatory balance in the studied lung samples.

3. The identified tendency toward redistribution of air between the alveolar and bronchiolar compartments reflects early functional alterations accompanying structural remodeling of lung tissue under the toxic influence of Leiurus macroctenus venom as early as three hours after exposure.

References

[1] Azevedo, E., Figueiredo, R. G., Pinto, R. V., Ramos, T. D. C. F., Sampaio, G. P., Bulhosa Santos, R. P., ... & Trindade, S. C. (2020). Evaluation of systemic inflammatory response and lung injury induced by Crotalus durissus cascavella venom. *PLoS One*, *15*(2), e0224584. doi: 10.1371/journal.pone.0224584

[2] Barrios-Montivero, A. E., Martínez, P. A., & Ojanguren-Affilastro, A. A. (2025). The Ongoing Expansion of the Medically Important Scorpions in Southern South America: AE Barrios-Montivero et al. *EcoHealth*, *22*(3), 313-331. doi: 10.1007/s10393-025-01722-0

[3] Bordon, K. C., Santos, G. C., Martins, J. G., Wiezel, G. A., Amorim, F. G., Crasset, T., ... & Arantes, E. C. (2025). Pioneering comparative proteomic and enzymatic profiling of Amazonian scorpion venoms enables the isolation of their first α-Ktx, metalloprotease, and phospholipase A2. *Toxins*, *17*(8), 411. doi: 10.3390/toxins17080411

[4] Borges, A., Caballero, C., de Arias, A. R., Smith, P., Owen, M., Nishi, A., ... & Wieczorko, T. (2025). First report of the medically significant Argentine scorpion Tityus carrilloi (Buthidae) in Paraguay: Epidemiological implications amid rising regional scorpionism. *Toxicon*, *264*, 108456. doi: 10.1016/j.toxicon.2025.108456

[5] Costa, M. F., da Silva, A. V., & de Vasconcelos, R. N. (2025). A Bibliometric Analysis of Scorpionism Epidemiology in Tropical Health. *Journal of Scientometric Research*, *14*(1), 142-59. doi: 10.5530/jscires.20251090

[6] Darkaoui, B., Lafnoune, A., Chgoury, F., Daoudi, K., Chakir, S., Mounaji, K., ... & Naoual, O. (2022). Induced pathophysiological alterations by the venoms of the most dangerous Moroccan scorpions Androctonus mauretanicus and Buthus occitanus: A comparative pathophysiological and toxic-symptoms study. *Human & Experimental Toxicology*, *41*, 09603271211072872. doi: 10.1177/09603271211072872

[7] de Andrade Moura, T., Chaves-Silveira, J., da Fonseca Teixeira, I. B., da Silva, F. F., Duarte, M. C. L. F., Oliveira, D., ... & Martinez, P. A. (2025). Impact of climate change on the distribution of Tityus scorpions (Buthidae) in the Amazon: Implications for conservation units and indigenous territories. *Toxicon*, *266*, 108532. doi: 10.1016/j.toxicon.2025.108532

[8] de Andrade Moura, T., Ojanguren-Affilastro, A. A., Sasa, M., Gutiérrez, J. M., Silva, F. F., Siqueira-Silva, T., & Martinez, P. A. (2025). AI models uncover factors influencing scorpionism in Northern Brazil. *Toxicon*, *258*, 108342. doi: 10.1016/j.toxicon.2025.108342

[9] de Oliveira Neto, J., de Moraes Silveira, J. A., Serra, D. S., de Araújo Viana, D., Borges-Nojosa, D. M., Sampaio, C. M. S., ... & Evangelista, J. S. A. M. (2017). Pulmonary mechanic and lung histology induced by Crotalus durissus cascavella snake venom. *Toxicon*, *137*, 144-149. doi: 10.1016/j.toxicon.2017.07.023

[10] Elmourid, A., Namiq, S., Boussaa, S., El Hidan, M. A., Bouimeja, B., & Touloun, O. (2025). Epidemiological profile and faunistic aspects of scorpionism in central Morocco: Evidence from three provinces. *Toxicon*, *269*, 108662. doi: 10.1016/j.toxicon.2025.108662

[11] Feola, A., Perrone, M. A., Piscopo, A., Casella, F., Della Pietra, B., & Di Mizio, G. (2020, September). Autopsy findings in case of fatal scorpion sting: a systematic review of the literature. In *Healthcare* (Vol. 8, No. 3, p. 325). MDPI. doi: 10.3390/healthcare8030325

[12] Gunas, V., Maievskyi, O., Raksha, N., Vovk, T., Savchuk, O., Shchypanskyi, S., & Gunas, I. (2024). Study of the Acute Toxicity of Scorpion Leiurus macroctenus Venom in Rats. *The Scientific World Journal*, *2024*(1), 9746092. doi: 10.1155/2024/9746092

[13] Haihua, C., Wei, W., Kun, H., Yuanli, L., & Fei, L. (2018).

Cobra venom factor-induced complement depletion protects against lung ischemia reperfusion injury through alleviating blood-air barrier damage. *Scientific reports*, *8*(1), 10346. doi: 10.1038/s41598-018-28724-z

[14] Kim, S., Kim, H. W., Chang, S. H., Leem, K. H., & Park, H. J. (2021). Bee venom prevents mucin 5AC production through inhibition of AKT and SPDEF activation in airway epithelia cells. *Toxins*, *13*(11), 773. doi: 10.3390/toxins13110773

[15] Kobzina-Didukh, D. S. (2025). Histological changes in the adrenal glands of rats one day after exposure to the venom of the scorpion Leiurus macroctenus. *Вісник Вінницького національного медичного університету=Reports of Vinnytsia National Medical University*, *29*(4), 566-571. doi: 10.31393/reports-vnmedical-2025-29(4)-02

[16] Lasavutz, V. S. (2024). Analysis of morphometric parameters of lung tissue under conditions of exposure to the venom of the vipers Vipera berus berus and Vipera berus nikolskii. *Морфологія=Morphologia*, *18*(4), 61-65. doi: 10.26641/1997-9665.2024.4.61-65

[17] Lasavutz, V. S. (2024). The morphological state of the lungs of rats exposed to Vipera berus nikolskii venom. *Морфологія=Morphologia*, *18*(3), 55-59. doi: 10.26641/1997-9665.2024.3.55-59

[18] Matkivska, R. M. (2025). Histological changes in the kidneys of experimental rats 3 hours after exposure to the venom of the scorpion Leiurus macroctenus. *Морфологія=Morphologia*, *19*(1), 31-34. doi: 10.26641/1997-9665.2025.1.31-34

[19] Miyamoto, J. G., Andrade, F. B., Ferraz, C. R., Candido, D. M., Knysak, I., Venancio, E. J., ... & Kwasniewski, F. H. (2018). A comparative study of pathophysiological alterations in scorpionism induced by Tityus serrulatus and Tityus bahiensis venoms. *Toxicon*, *141*, 25-33. doi: 10.1016/j.toxicon.2017.11.005

[20] Özkan, Ö., & Filazi, A. (2004). The determination of acute lethal dose-50 (LD50) levels of venom in mice, obtained by different methods from scorpions, Androctonus crassicauda (Oliver 1807). *Acta Parasitol Turcica*, *28*(1), 50-53.

[21] Pucca, M. B., Cavalcante, J. S., Jati, S. R., Cerni, F. A., Ferreira Jr, R. S., & Arantes, E. C. (2025). Scorpions are taking over: the silent and escalating public health crisis in Brazil. *Frontiers in Public Health*, *13*, 1573767. doi: 10.3389/fpubh.2025.1573767

[22] Rigoni, V. L. S., Kwasniewski, F. H., Vieira, R. P., Linhares, I. S., da Silva, J. L. V., Nogueira-Pedro, A., & Zamuner, S. R. (2016). Human bronchial epithelial cells injury and cytokine production induced by Tityus serrulatus scorpion venom: An in vitro study. *Toxicon*, *120*, 22-28. doi: 10.1016/j.toxicon.2016.07.013

[23] Saadi, H., Mouane, A., Ramdani, N., Chikha, M., Belkacemi, H., Ali, M. F., ... & Sadine, S. E. (2025). Unveiling scorpionism in Northern Algerian Sahara (El Oued Province): Epidemiological trends and faunistic diversity. *Toxicon*, *267*, 108597. doi: 10.1016/j.toxicon.2025.108597

[24] Saidi, H., Bérubé, J., Laraba-Djebari, F., & Hammoudi-Triki, D. (2018). Involvement of alveolar macrophages and neutrophils in acute lung injury after scorpion envenomation: New pharmacological targets. *Inflammation*, *41*(3), 773-783. doi: 10.1007/s10753-018-0731-9

[25] Sanclemente-Paz, E. (2025). Nephropathy Caused by Scorpion Stings. In *Tropical Nephrology* (pp. 113-120). Cham: Springer Nature Switzerland. doi: 10.1007/978-3-031-94777-3_9

[26] Solano, D., Rucavado, A., Escalante, T., Tavares, E. B. G., Bezerra, S. K. M., Olivo, C. R., ... & Gutiérrez, J. M. (2025). An Experimental Model of Acute Pulmonary Damage Induced by the Phospholipase A2-Rich Venom of the Snake Pseudechis papuanus. *Toxins*, *17*(6), 302. doi: 10.3390/toxins17060302

[27] Yaqoob, R., Tahir, H. M., Arshad, M., Naseem, S., & Ahsan, M. M. (2016). Optimization of the conditions for maximum recovery of venom from scorpions by electrical stimulation. *Pakistan journal of zoology*, *48*(1), 265-269. Corpus ID: 88882373

МІКРОСКОПІЧНІ ТА МОРФОМЕТРИЧНІ ЗМІНИ У БРОНХАХ І ПАРЕНХІМІ ЛЕГЕНЬ ЛАБОРАТОРНИХ ЩУРІВ ЧЕРЕЗ ТРИ ГОДИНИ ПІСЛЯ ВВЕДЕННЯ ОТРУТИ СКОРПІОНУ LEIURUS MACROCTENUS

Гунас В. І., Маєвський О. Є., Скорук Р. В., Кириченко В. І., Бандурка Н. М., Сорокоумов В. П., Гунас І. В.

Скорпіонізм є поширеним явищем, що зустрічається в різних регіонах світу, та несе особливу небезпеку для осіб похилого віку та дітей. Незважаючи на численні випадки дії отрути скорпіонів на організм людини, незначна кількість публікацій описують клінічну картину, особливо з боку дихальної системи у таких пацієнтів. Ще менше робіт присвячені опису морфологічних змін легень чи бронхів у померлих осіб чи лабораторних тварин, зокрема в різні часові рамки після укусу скорпіона. Дані прогалини на морфологічному рівні, навіть при досить добре вивченому патогенетичному шляху дії отрути скорпіона, не дозволяють мати повне розуміння картини токсичного впливу даної речовини. Лише за умов всебічного дослідження отрути можливе в подальшому не тільки створення протиотрути до неї але і застосування як перспективного лікарського засобу. Мета дослідження – визначити мікроскопічні та морфометричні зміни у бронхах і паренхімі легень щурів через 3 години після введення отрути виду скорпіона Leiurus macroctenus. Для дослідження використано 10 щурів самців, що утримувалися в умовах віварію і були розділені на 2 групи по 5 осіб у кожній: група 1 – щури контрольної групи, яким вводили фізіологічний розчин та щури групи 2 – яким вводили отруту скорпіона у дозі 28,8 мкг/мл. Через 3 години після введення проводили евтаназію щурів з вилученням легень на гістологічне дослідження. Для проведення мікроскопічного і морфометричного дослідження виготовлялися зрізи товщиною 4-5 мкм (забарвлення гематоксиліном-еозином і за методом Azan Trichrome) та напівтонкі зрізи 1-2 мкм (метиленовий синій). Мікроскопію виконували при збільшеннях від ×40 до ×1000 на мікроскопі OLIMPUS BX 41. Морфометричний аналіз виконували з допомогою програмного забезпечення Quickphoto Micro 2.3. Статистичний аналіз отриманих результатів проведений у ліцензійному пакеті «Statistica 6.0» з використанням непараметричних методів оцінки. Через 3 години після введення отрути у легенях дослідних тварин формуються виражені запальні зміни, що проявляються масивною лімфоцитарно-нейтрофільною інфільтрацією, найбільш інтенсивною навколо бронхів середнього, малого діаметрів та бронхіол, аж до часткового руйнуванням їх стінок, фрагментації м'язових пучків та набряку адвентиції. У міжальвеолярному просторі переважають базофіли, еозинофіли та макрофаги, що також свідчить на користь вираженої запальної реакції. У паренхімі ділянки дисателектазів чергуються з ділянками емфіземи, де місцями спостерігається деструкція міжальвеолярних

перегородок та накопичення рідини. При морфометричному дослідженні зафіксовано зменшення ширини альвеол, їх входу та глибини (p=0,112, p=0,008 та p=0,174 відповідно), а також статистично значуще звуження провідного відділу респіраторних бронхіол (p=0,045). Виявлено тенденцію до перерозподілу повітря між альвеолярним та бронхіолярним відділами, що відображено при гістологічному дослідженні змінами співвідношень морфометричних показників. Отримані дані свідчать про розвиток гострого запально-деструктивного ураження легень з порушенням вентиляційної функції вже у ранні терміни після інтоксикації. Сукупність виявлених мікроскопічних змін вказує на формування структурної перебудови легеневої паренхіми у відповідь на токсичну дію отрути вже на 3 годину після її введення лабораторним тваринам.

Ключові слова: *морфологія, отрута скорпіона, Leiurus macroctenus, щури, бронхи, паренхіма легень, морфологічні зміни, морфометричні зміни.*

Author's contribution

Gunas V. I. – research, methodology and writing of the original draft, conceptualization, formal analysis, software.
Maievskyi O. Ye. – supervision.
Skoruk R. V. – review writing and editing.
Kyrychenko V. I. – review writing and editing.
Bandurka N. M. – validation.
Sorokoumov V. P. – data visualization.
Gunas I. V. – project administration.

DOI: 10.31393/morphology-journal-2026-32(1)-04 Reports of Morphology, Vol. 32, №1, Pages 26-31

ISSN 1818-1295 eISSN 2616-6194

REPORTS OF MORPHOLOGY

Official Journal of the Scientific Society of Anatomists, Histologists, Embryologists and Topographic Anatomists of Ukraine

journal homepage: https://morphology-journal.com

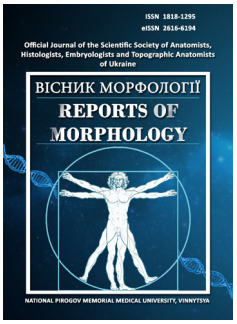

Empagliflozin attenuates post-injury myocardial remodeling in a rat isoproterenol model: a morphological and morphometric study

Kozan I. I., Fedorov S. V., Kozan N. M., Herashchenko A. S.

Ivano-Frankivsk National Medical University, Ivano-Frankivsk, Ukraine

ARTICLE INFO

Received: 24 June 2025

Accepted: 10 December 2025

UDC: 616.127-005.8:616.12-008.46:615.03

CORRESPONDING AUTHOR

e-mail: irakozan@ukr.net

Kozan I. I.

CONFLICT OF INTEREST

The authors have no conflicts of interest to declare.

FUNDING

Not applicable.

DATA SHARING

Data are available upon reasonable request to corresponding author.

Adverse post-myocardial infarction remodeling is a key pathway toward chronic heart failure. While sodium-glucose cotransporter-2 (SGLT2) inhibitors improve outcomes in heart failure, evidence on their structural effects when therapy is initiated after the acute injury phase remains limited. Study aim – to evaluate whether delayed initiation of empagliflozin attenuates histological remodeling features and reduces morphometric indices of cardiomyocyte hypertrophy in rats with isoproterenol-induced myocardial injury. Sixty male outbred white rats (200-250 g) were allocated to three groups (n=20 each): intact control, isoproterenol (ISO) + placebo, and ISO + empagliflozin. Myocardial injury was induced by ISO (85 mg/kg/day, subcutaneously, on days 0 and 1). From day 14, animals received empagliflozin (10 mg/kg/day by oral gavage) or vehicle for 30 days. Hearts were harvested on day 44. Left-ventricular sections were obtained from subendocardial, intramural, and subepicardial layers and stained with hematoxylin-eosin and Masson's trichrome. Digital morphometry quantified cardiomyocyte and nuclear area. Statistical analysis was conducted using the IBM SPSS 26.0 software (IBM, USA). It was established that ISO caused microvascular congestion, interstitial edema, cardiomyocyte disarray, and increased collagen deposition on Masson's staining. Delayed empagliflozin reduced the qualitative severity of injury and attenuated hypertrophic morphometry. Cardiomyocyte area was higher in ISO + placebo than in control (342.8±12.5 μm² vs 223.2±8.4 μm²; p<0.01) and decreased in ISO + empagliflozin (287.4±8.3 μm²; p<0.05 vs ISO + placebo), while remaining above control. Nuclear area followed a similar pattern (36.95±1.07 μm² vs 20.73±0.54 μm² in ISO + placebo and 26.81±0.65 μm² with empagliflozin). Acquired data suggests that delayed empagliflozin use after the experimental myocardial damage partially alleviates structural remodelling and morphometric signs of cardiomyocyte hypertrophy.

Keywords: *empagliflozin, morphology, myocardial remodeling, isoproterenol, fibrosis, morphometry, heart failure.*

Introduction

Adverse post-myocardial infarction (post-MI) remodeling is a multilevel process that connects an acute ischemic injury to chronic heart failure through myocyte loss, fibroblast activation, extracellular matrix (ECM) expansion, and maladaptive changes in ventricular geometry [16, 18]. Fibrosis and cardiomyocyte hypertrophy jointly increase myocardial stiffness and contribute to electrical instability and progressive dysfunction, which makes them clinically meaningful structural endpoints [28].

The study by Yap et al. examined the complex, dual role of macrophages in heart repair and remodeling following a myocardial infarction. It highlights the functional shift from early-phase pro-inflammatory macrophages, which clear necrotic debris, to late-phase reparative macrophages that facilitate scar formation and tissue stability. A central theme is the distinct origins of these cells, contrasting protective resident cardiac macrophages – which are present from birth and support heart health – with recruited monocyte-derived macrophages that can drive excessive inflammation and heart failure. By utilizing advanced single-cell sequencing, the authors argue for a move beyond simple classification toward "precision immunotherapies" that aim to reprogram these immune cells to optimize healing and prevent the pathological structural changes that lead to chronic cardiac

dysfunction [33].

In addition to gross structural changes, the infarct border zone (IBZ) serves as a critical arrhythmogenic substrate where complex cellular and molecular remodeling facilitates the development of life-threatening ventricular arrhythmias. This localized remodeling involves the transformation of resident fibroblasts into matrifibrocytes, the disruption of gap junction proteins such as Connexin43, and the impairment of ion channel function, which collectively create reentry circuits and electrical instability within the peri-infarct myocardium. Addressing these alterations through targeted pharmacological interventions or catheter ablation is essential, as the stabilization of the IBZ represents a pivotal therapeutic strategy for preventing sudden cardiac death post-myocardial infarction [7, 24].

SGLT2 inhibitors have emerged as disease-modifying therapy in heart failure, reducing heart-failure hospitalization and improving outcomes across phenotypes, including patients without diabetes [3, 20, 22]. Beyond glycemic actions, SGLT2 inhibition has been linked to improved myocardial energetics, reduction of oxidative stress, modulation of ionic homeostasis, and attenuation of profibrotic signaling, suggesting the potential to influence remodeling pathways directly [11, 19, 29]. However, the timing of initiation may be critical: structural remodeling evolves over weeks to months, and the degree to which SGLT2 inhibitors can modify remodeling when started after the early injury phase remains insufficiently characterized.

Rodent models are essential for mechanistic evaluation because they allow standardized injuries and controlled tissue sampling. The isoproterenol (ISO) model produces diffuse beta-adrenergic stress and injury with subsequent interstitial remodeling and fibrosis and is widely used to test antifibrotic and antihypertrophic interventions [5, 15].

Alpha-adrenoceptors provide a critical inotropic boost during early cardiac stress, while their chronic activation results in a unique pattern of hypertrophy and fibrosis that differs from isolated beta-stimulation. This suggests that the alpha1-signaling pathway is a significant, yet often overlooked, driver of early adaptive and subsequent maladaptive remodeling, emphasizing the need to consider multi-receptor signaling in the development of heart failure therapies [13].

Accordingly, this study tested the hypothesis that delayed initiation of empagliflozin after ISO-induced myocardial injury attenuates structural remodeling on histology and reduces morphometric indices of cardiomyocyte hypertrophy.

The aim of the study – to evaluate whether delayed initiation of empagliflozin attenuates histological remodeling and reduces morphometric indices of cardiomyocyte hypertrophy in rats with isoproterenol-induced myocardial injury.

Materials and methods

Experiments were designed and reported in accordance with ARRIVE 2.0 guidance and applicable European animal welfare legislation [14, 23]. Sixty male outbred white rats (200-250 g) were housed under standard conditions (12 h light / 12 h dark, 20-24 °C) with ad libitum access to chow and water. All procedures were approved by the institutional animal ethics committee Ivano-Frankivsk National Medical University (protocol No. 153/25 17.09.2025).

A controlled, parallel-group design was used with three groups (n=20 per group): 1 – intact control; 2 – ISO + placebo; 3 – ISO + empagliflozin. Randomization was performed using a computer-generated list. Image acquisition parameters were standardized, and digital morphometry was performed by an investigator blinded to group allocation.

Myocardial injury was induced by subcutaneous injections of isoproterenol hydrochloride (ISO; Sigma-Aldrich, USA) at 85 mg/kg/day for two consecutive days (days 0 and 1), a commonly applied regimen for beta-adrenergic injury followed by remodeling [17, 25]. Control animals received an equal volume of 0.9 % saline on the same schedule.

To model delayed initiation after the early injury phase, no active treatment was administered during days 0-13 aside from routine monitoring. From day 14, animals in the ISO + empagliflozin group received empagliflozin 10 mg/kg/day via oral gavage for 30 consecutive days (days 14-43); the ISO + placebo group received vehicle on the same schedule. The selected dose is within the range used in preclinical remodeling studies and provides systemic SGLT2 inhibition in rats [4, 12].

Animals were assessed daily for activity, grooming, respiratory pattern, and food/water intake. Humane endpoints included marked weight loss, severe dyspnea, or persistent distress. All animals were euthanized at the planned endpoint on day 44. Euthanasia was performed under deep anesthesia followed by exsanguination in accordance with AVMA guidance [1].

After thoracotomy, hearts were excised, rinsed in cold saline, and fixed in 10 % neutral buffered formalin for at least 24 h. After paraffin embedding, 4-5 μm transverse sections were obtained from the mid-ventricular level. Sampling explicitly included three left-ventricular layers: subendocardial, intramural, and subepicardial. Sections were stained with hematoxylin-eosin for general morphology and Masson's trichrome for collagen visualization [6].

Images were acquired using a bright-field microscope equipped with a calibrated digital camera. Total magnification ×576 corresponded to a 40× objective, a 10× ocular, and a 1.44× camera adapter (40×10×1.44=576). Scale bars were generated after calibration with a stage micrometer and were included in representative micrographs.

Digital morphometry was performed in ImageJ/Fiji [27]. For each animal, one section per ventricular layer was analyzed. In each layer, 10 non-overlapping fields were selected using systematic random sampling (random starting field followed by every k-th field). Cardiomyocytes with an intact contour and a clearly visible nucleus were measured; per animal, at least 90 cardiomyocytes (≥30 per layer) were quantified. Cross-sectional area (μm²) of the cardiomyocyte

and nuclear area (μm²) were obtained by manual outlining. For statistical analysis, the mean value per animal (not per cell) was used as the experimental unit to avoid pseudo-replication.

Statistical analysis was performed using IBM SPSS 26.0 software (IBM, USA). Data are presented as mean±SEM. Normality was assessed using the Shapiro-Wilk test. Group differences were evaluated using one-way ANOVA followed by Tukey's post-hoc comparisons for multiple testing. A two-sided $p<0.05$ was considered statistically significant.

Results

All animals were followed until the prespecified endpoint (day 44). Representative micrographs are shown for the two post-injury experimental groups included in the image set (ISO + placebo and ISO + empagliflozin) (Fig. 1, Fig. 2). Control histology is summarized for context but not illustrated in the current figure set. Qualitative microscopy was complemented by quantitative morphometry across all three groups (Table 1).

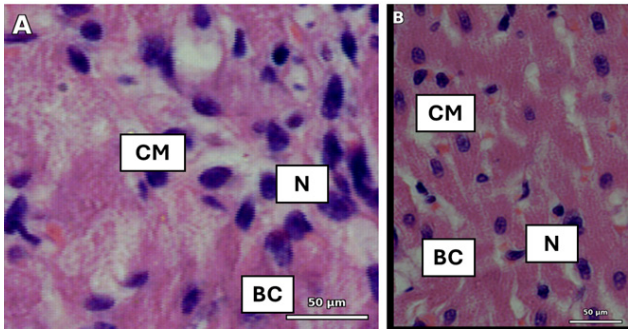

Fig. 1. Representative hematoxylin and eosin micrographs of left-ventricular myocardium from the ISO + placebo group (A) and the ISO + empagliflozin group (B). Scale bar = 50 μm. **Notes:** CM – cardiomyocyte; BC – blood capillary; N – nucleus.

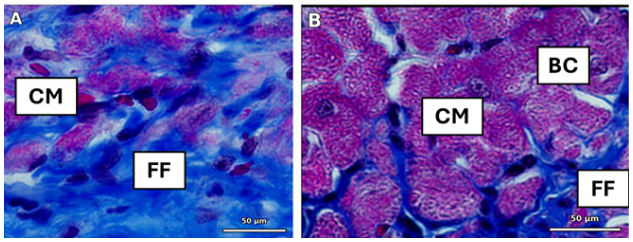

Fig. 2. Representative Masson's trichrome micrographs of left-ventricular myocardium from the ISO + placebo group (A) and the ISO + empagliflozin group (B). Collagen fibers are stained blue. Scale bar = 50 μm. **Notes:** CM – cardiomyocyte; BC – capillary; FF – focus of fibrosis.

In the ISO + placebo group, hematoxylin and eosin stained sections demonstrated a remodeling phenotype characterized by cardiomyocyte enlargement, myofibrillar disorganization, microvascular congestion, and interstitial widening consistent with edema. Clusters of small mononuclear cells were frequently observed in the interstitium, supporting an inflammatory component of ongoing post-injury remodeling (see Fig. 1A).

Table 1. Morphometric parameters of left-ventricular cardiomyocytes.

Parameter	Control (n=20)	ISO + placebo (n=20)	ISO + empagliflozin (n=20)	p value
Cardiomyocyte area, μm²	223.2±8.4	342.8±12.5*	287.4±8.3#	<0.001
Nuclear area, μm²	20.73±0.54	36.95±1.07*	26.81±0.65#	<0.001

Notes: * – $p<0.01$ vs control; # – $p<0.05$ vs ISO + placebo (one-way ANOVA with Tukey post-hoc).

In the ISO + empagliflozin group, the overall severity of these changes was reduced. Myocardial architecture appeared more orderly with less conspicuous interstitial widening and fewer inflammatory cell aggregates, while residual cardiomyocyte hypertrophy remained detectable (see Fig. 1B).

Masson's trichrome in ISO + placebo showed prominent expansion of collagen (blue) within the interstitium and around small vessels, with areas of more confluent collagen deposition suggestive of replacement fibrosis in regions compatible with myocyte dropout (see Fig. 2A).

In ISO + empagliflozin, collagen accumulation remained present but appeared less extensive and less confluent than in the placebo group, with more preserved cardiomyocyte bundles separating collagen strands (see Fig. 2B).

Quantitative morphometry supported the qualitative impressions. Compared with controls, cardiomyocyte area increased by 53.6 % in ISO + placebo and by 28.8 % with empagliflozin; relative to ISO + placebo, empagliflozin was associated with a 16.2 % lower mean cardiomyocyte area (one-way ANOVA with Tukey post-hoc; see Table 1).

Nuclear area followed a similar pattern: relative to controls, nuclear area rose by 78.2 % in ISO + placebo and by 29.3 % in ISO + empagliflozin, with a 27.4 % lower nuclear area in ISO + empagliflozin versus ISO + placebo (see Table 1).

Discussion

This study evaluated whether empagliflozin initiated after the early phase of beta-adrenergic myocardial injury influences structural remodeling in a rat ISO model. The main findings are that delayed empagliflozin reduced the qualitative severity of histological remodeling (edema, microvascular congestion, injury pattern, and collagen deposition) and attenuated morphometric signatures of cardiomyocyte hypertrophy compared with placebo. These results indicate that remodeling pathways remain partially modifiable beyond the acute injury "window" and that SGLT2 inhibition can exert a measurable antihypertrophic and potentially antifibrotic signal even when started after early injury evolution.

Post-injury remodeling is a dynamic, evolving continuum rather than an isolated event. Following the acute phase, sustained inflammatory signaling triggers fibroblast proliferation, myofibroblast differentiation, and extracellular matrix (ECM) turnover. This is accompanied

by a cardiomyocyte growth response, primarily driven by mechanical strain and neurohormonal activation [34].

Within this framework, fibrosis and hypertrophy are intrinsically linked: ECM expansion enhances passive stiffness and impairs cardiomyocyte-capillary coupling, while hypertrophy – initially an adaptive response to normalize wall stress – eventually becomes maladaptive. Although the isoproterenol (ISO) model differs from coronary occlusion, it reliably replicates diffuse injury and interstitial remodeling, serving as a robust platform for evaluating therapies targeting fibrosis and hypertrophy [2, 15]. The qualitative changes observed in this study – including microvascular congestion, edema, structural disarray, and collagen deposition – align closely with this established conceptual framework.

Clinical trials have established that SGLT2 inhibitors significantly reduce heart failure hospitalizations and improve cardiovascular outcomes across diverse HF phenotypes, including in non-diabetic populations [8, 31, 32]. While the rapid clinical benefits are often attributed to hemodynamic and renal mechanisms, accumulating mechanistic evidence suggests that SGLT2 inhibition directly modulates myocardial morphology. Proposed pathways include enhanced substrate and mitochondrial metabolism, attenuation of oxidative stress, restoration of intracellular sodium and calcium homeostasis, and suppression of pro-fibrotic signaling and inflammatory activation [9, 10, 21]. Although these specific pathways were not directly assayed in the present study, our morphological and morphometric findings are consistent with a remodeling-modifying effect rather than a purely hemodynamic influence, as they reflect fundamental changes in tissue composition and cellular growth.

In rat models of myocardial infarction, empagliflozin has been shown to improve post-infarct remodeling, a process associated with increased expression of GTP-cyclohydrolase-1 and NO-signaling pathways, suggesting microvascular and redox-mediated protection against hypertrophy and interstitial remodeling [4]. Furthermore, studies in non-diabetic rats early after infarction have demonstrated significant impacts on cardiac fibrosis and physiology [12]. Despite variations in injury triggers and timing across these studies, a consistent theme emerges: the capacity of SGLT2 inhibition to mitigate the fibrotic and hypertrophic processes inherent to myocardial remodeling.

Human mechanistic trials provide additional context. EMPA-TROPISM demonstrated improvements in ventricular volumes, mass, and functional parameters in non-diabetic HFrEF patients, consistent with reverse remodeling at the organ level [26]. In the post-MI setting, the EMMY trial reported beneficial effects on biomarkers and imaging parameters when empagliflozin was initiated shortly after acute myocardial infarction [30]. The present study differs intentionally by delaying therapy until day 14 after ISO injury, aiming to approximate a subacute/chronic initiation scenario. The observation that morphometric hypertrophy and qualitative remodeling markers were still attenuated suggests that at least part of the remodeling program remains sensitive to SGLT2 inhibition beyond the early injury phase.

Quantitative morphometry provided a robust second line of evidence supporting the qualitative histology. Cardiomyocyte area increased by more than 50 % after ISO exposure, and nuclear area increased by nearly 80 %, supporting true cellular hypertrophy rather than sampling artifact. Delayed empagliflozin reduced both indices. Although a formal nuclear-cytoplasmic ratio was not directly calculated, a descriptive nuclear-to-cell area ratio derived from group means increased after ISO exposure and returned to control with empagliflozin, indicating parallel modulation of cellular and nuclear growth. Such a pattern aligns with the concept that antihypertrophic effects may reflect upstream signaling modulation rather than selective nuclear changes.

The methodological choices were structured to improve reproducibility and to address common reporting weaknesses in animal studies. Blinded morphometry, explicit layer sampling, and animal-level statistical units were used to reduce bias and pseudo-replication. In addition, explicit reporting of optical components and adapter-derived total magnification clarifies image scaling and reduces a frequent source of confusion in morphological manuscripts [23]. Because there were three experimental groups, inference was based on one-way ANOVA with multiplicity-controlled post-hoc testing rather than on repeated pairwise tests.

Several limitations should be acknowledged. Fibrosis was described qualitatively based on Masson's staining rather than quantified as collagen area fraction using standardized thresholding or confirmed biochemically (e.g., hydroxyproline). Functional endpoints such as echocardiography or hemodynamics were not included, so structural observations cannot be directly linked to systolic or diastolic performance. In addition, only male animals were used, and sex-specific differences in remodeling biology may limit generalization. Although sampling covered three ventricular layers, the present morphometry was not designed to test layer-specific gradients of remodeling.

Future studies should incorporate quantitative fibrosis metrics, molecular profiling of fibro-inflammatory pathways, and functional cardiac assessment to establish a "structure-mechanism-function" chain for delayed SGLT2 inhibition.

Conclusions

1. Isoproterenol-induced injury produced a remodeling phenotype with edema, architectural disarray, collagen deposition, and marked cardiomyocyte/nuclear hypertrophy.

2. Empagliflozin initiated two weeks after injury partially attenuated histological remodeling and significantly reduced morphometric indices of hypertrophy compared with placebo.

References

[1] American Veterinary Medical Association. (2020). AVMA guidelines for the euthanasia of animals: 2020 edition. https://

www.avma.org/sites/default/files/2020-02/Guidelines-on-Euthanasia-2020.pdf

[2] Anamalley, R., Rajassageran, L., Apparoo, Y., Jauri, M. H., Kamisah, Y., Murni Yunos, N., & Budin, S. B. (2022). Repeated administration of low dose isoprenaline on the rat's cardiovascular system. *Sains Malaysiana*, *51*(7), 2147-2157. doi: 10.17576/jsm-2022-5107-17

[3] Anker, S. D., Butler, J., Filippatos, G., Ferreira, J. P., Bocchi, E., Böhm, M., ... & Packer, M. (2021). Empagliflozin in heart failure with a preserved ejection fraction. *N Engl J Med*, *385*(16), 1451-1461. doi: 10.1056/NEJMoa2107038

[4] Asensio Lopez, M. D. C., Lax, A., Hernandez Vicente, A., Saura Guillen, E., Hernandez-Martinez, A., Fernandez Del Palacio, M. J., ... & Pascual-Figal, D. (2020). Empagliflozin improves post-infarction cardiac remodeling through GTP enzyme cyclohydrolase 1 and irrespective of diabetes status. *Scientific Reports, 10*(1), 13553. doi: 10.1038/s41598-020-70454-8

[5] Bader Eddin, L., Nagoor Meeran, M. F., Kumar Jha, N., Goyal, S. N., & Ojha, S. (2025). Isoproterenol mechanisms in inducing myocardial fibrosis and its application as an experimental model for the evaluation of therapeutic potential of phytochemicals and pharmaceuticals. *Animal Models and Experimental Medicine, 8*(1), 67-91. doi: 10.1002/ame2.12496

[6] Bancroft, J. D., & Gamble, M. (Eds.). (2019). *Theory and practice of histological techniques (8th ed.).* Elsevier. https://www.elsevier.com/books/theory-and-practice-of-histological-techniques/9780702068645

[7] Calcagno, D. M., Taghdiri, N., Ninh, V. K., Mesfin, J. M., Toomu, A., Sehgal, R., & Christman, K. L. (2022). Single-cell and spatial transcriptomics of the infarcted heart define the dynamic onset of the border zone in response to mechanical destabilization. *Nature Cardiovascular Research, 1*(11), 1039-1055. doi: 10.1038/s44161-022-00160-3

[8] Chen, B., Guo, J., Ye, H., Wang, X., & Feng, Y. (2024). Role and molecular mechanisms of SGLT2 inhibitors in pathological cardiac remodeling (Review). *Molecular Medicine Reports*, *29*(5), 73. doi: 10.3892/mmr.2024.13197

[9] Chen, R., Zhang, Y., Zhang, H., Zhou, H., Tong, W., Wu, Y., & Chen, Y. (2023). SGLT2 inhibitor dapagliflozin alleviates intramyocardial hemorrhage and adverse ventricular remodeling via suppressing hepcidin in myocardial ischemia-reperfusion injury. *Eur J Pharmacol*, *950*, 175-729. doi: 10.1016/j.ejphar.2023.175729

[10] Chen, R., Zhang, Y., Zhou, H., Hu, Y., & Chen, Y. (2023). SGLT2 inhibitor-pretreated macrophage transplantation improves adverse ventricular remodeling after acute myocardial infarction. *Journal of Cardiovascular Pharmacology*, *82*(4), 287-297. doi: 10.1097/FJC.0000000000001466

[11] Cowie, M. R., & Fisher, M. (2020). SGLT2 inhibitors: Mechanisms of cardiovascular benefit beyond glycaemic control. *Nature Reviews Cardiology, 17*, 761-772. doi: 10.1038/s41569-020-0406-8

[12] Daud, E., Ertracht, O., Bandel, N., Cohen, S., & Binah, O. (2021). The impact of empagliflozin on cardiac physiology and fibrosis early after myocardial infarction in non-diabetic rats. *Cardiovascular Diabetology*, *20,* Article 132. doi: 10.1186/s12933-021-01322-6

[13] Dewenter, M., Pan, J., Knödler, L., Tzschöckel, N., Henrich, J., Cordero, J., & Vettel, C. (2022). Chronic isoprenaline/phenylephrine vs. exclusive isoprenaline stimulation in mice: critical contribution of alpha$_1$-adrenoceptors to early cardiac stress responses. *Basic Research in Cardiology*, *117*(1)*,* 15. doi: 10.1007/s00395-022-00920-z

[14] European Parliament & Council. (2010). Directive 2010/63/EU of the European Parliament and of the Council of 22 September 2010 on the protection of animals used for scientific purposes. *Official Journal of the European Union*, *L276*, 33-79. http://data.europa.eu/eli/dir/2010/63/oj

[15] Flori, L., Lazzarini, G., Spezzini, J., Pirone, A., Calderone, V., Testai, L., & Miragliotta, V. (2024). The isoproterenol-induced myocardial fibrosis: A biochemical and histological investigation. *Biomed & Pharmacother*, *174*, 116-534. doi: 10.1016/j.biopha.2024.116534

[16] Frantz, S., Hundertmark, M. J., Schulz-Menger, J., Bengel, F. M., & Bauersachs, J. (2022). Left ventricular remodelling post-myocardial infarction: pathophysiology, imaging, and novel therapies. *European Heart J, 43*(27), 2549-2561. doi: 10.1093/eurheartj/ehac223

[17] Li, H., Sureda, A., Devkota, H. P., Shaqra, Q. M., Shen, Z., Tang, J., & Cao, G. (2012). Cardioprotective effect of paeonol and danshensu combination on isoproterenol-induced myocardial injury in rats. *PLoS ONE, 7*(11), e48872. doi: 10.1371/journal.pone.0048872

[18] Logeart, D., Taille, Y., Derumeaux, G., Gellen, B., Sirol, M., Galinier, M., & Mercadier, J. J. (2024). Patterns of left ventricular remodeling post-myocardial infarction, determinants, and outcome. *Clin Res in Cardiol*, *113*(12), 1670-1681. doi: 10.1007/s00392-023-02331-z

[19] Lopaschuk, G. D., & Verma, S. (2020). Mechanisms of cardiovascular benefits of Sodium Glucose Co-Transporter 2 (SGLT2) Inhibitors: A State-of-the-Art Review. *JACC Basic to Translational Science*, *5*(6), 632-644. doi: 10.1016/j.jacbts.2020.02.004.

[20] McMurray, J. J., Solomon, S. D., Inzucchi, S. E., Køber, L., Kosiborod, M. N., Martinez, F. A., ... & Langkilde, A. M. (2019). Dapagliflozin in patients with heart failure and reduced ejection fraction. *N Engl J Med, 381*(21), 1995-2008. doi: 10.1056/NEJMoa1911303

[21] Minciună, I. A., Tomoaia, R., Mihăilă, D., Cismaru, G., Puiu, M., Roșu, R., … & Pop D. (2024). Recent advances in understanding the molecular mechanisms of SGLT2 inhibitors in atrial remodeling. *Curr Issues Mol Biol, 46*(9), 9607-9623. doi: 10.3390/cimb46090571

[22] Packer, M., Anker, S. D., Butler, J., Filippatos, G., Pocock, S. J., Carson, P., ... & Zannad, F. (2020). Cardiovascular and renal outcomes with empagliflozin in heart failure. *N Engl J Med, 383*(15), 1413-1424. doi: 10.1056/NEJMoa2022190

[23] Percie du Sert, N., Hurst, V., Ahluwalia, A., Alam, S., Avey, M. T., Baker, M., ... & Würbel, H. (2020). The ARRIVE guidelines 2.0: Updated guidelines for reporting animal research. *PLoS Biology, 18*(7), e3000410. doi: 10.1371/journal.pbio.3000410

[24] Rexius-Hall, M. L., Khalil, N. N., Escopete, S. S., Li, X., Hu, J., Yuan, H., … & McCain, M. L. (2022). A myocardial infarct border-zone-on-a-chip demonstrates distinct regulation of cardiac tissue function by an oxygen gradient. *Sci Adv, 8*(49). doi: 10.1126/sciadv.abn7097

[25] Rona, G., Chappel, C. I., Balazs, T., & Gaudry, R. (1959). An infarct-like myocardial lesion and other toxic manifestations produced by isoproterenol in the rat. *Archives of Pathology, 67*(4), 443-455. PMID: 13636626

[26] Santos-Gallego, C. G., Vargas-Delgado, A. P., Requena-Ibanez, J. A., Garcia-Ropero, A., Mancini, D., Pinney, S., & Badimon, J. J. (2021). Randomized trial of empagliflozin

in nondiabetic patients with heart failure and reduced ejection fraction (EMPA-TROPISM). *J Am Coll Cardiol, 77*(3), 243-255. doi: 10.1016/j.jacc.2020.11.008
[27] Schneider, C. A., Rasband, W. S., & Eliceiri, K. W. (2012). NIH Image to ImageJ: 25 years of image analysis. *Nature Methods, 9*(7), 671-675. doi: 10.1038/nmeth.2089
[28] Van Linthout, S., Matz, I., González, A., & Davis, J. (2025). Cardiac fibroblasts in myocardial injury and heart failure. *European Heart Journal*, Article ehaf902. doi: 10.1093/eurheartj/ehaf902
[29] Verma, S., & McMurray, J. J. V. (2018). SGLT2 inhibitors and mechanisms of cardiovascular benefit. *Diabetologia, 61*, 2108-2117. doi: 10.1007/s00125-018-4673-7
[30] von Lewinski, D., Kolesnik, E., Tripolt, N. J., Pferschy, P. N., Benedikt, M., Wallner, M., ... & Sourij, H. (2022). Empagliflozin in acute myocardial infarction: The EMMY trial. *European Heart Journal, 43*(41), 4421-4432. doi: 10.1093/eurheartj/ehac494
[31] Wan, J., Xu, F., Zuo, H., Jiang, X., Wang, Y., Jiang, Y., … & Li, H. (2024). Impact of SGLT2 inhibitors on left ventricular remodeling in diabetic patients with acute myocardial infarction. *J Cardiovasc Pharmacol Ther, 29*, 10742484241301191. doi: 10.1177/10742484241301191
[32] Xu, M. L., Wang, H., Ouyang, D., Qi, H., & Li, X. H. (2025). The impact of SGLT2 inhibitors on cardiac remodeling after myocardial infarction: An updated meta-analysis of randomized controlled trials. *Front Pharmacol, 16*, 1699066. doi: 10.3389/fphar.2025.1699066
[33] Yap, J., Irei, J., Lozano-Gerona, J., Vanapruks, S., Bishop, T., & Boisvert, W. A. (2023). Macrophages in cardiac remodelling after myocardial infarction. *Nat Rev Cardiol, 20*(6), 373-385. doi: 10.1038/s41569-022-00823-5
[34] Yong, J., Tao, J., Wang, K., Li, X., & Yang, Y. (2025). Post-myocardial infarction cardiac remodeling: Multidimensional mechanisms and clinical prospects of stem cell therapy. *Stem Cell Reviews and Reports, 21*(5), 1369-1427. doi: 10.1007/s12015-025-10888-7

ЕМПАГЛІФЛОЗИН ПОСЛАБЛЮЄ ПОСТУШКОДЖУВАЛЬНЕ РЕМОДЕЛЮВАННЯ МІОКАРДА ЩУРІВ ПРИ ВІДТЕРМІНОВАНОМУ ПРИЗНАЧЕННІ В МОДЕЛІ ІЗОПРЕНАЛІНУ: МОРФОЛОГІЧНЕ ТА МОРФОМЕТРИЧНЕ ДОСЛІДЖЕННЯ

Козань І. І., Федоров С. В., Козань Н. М., Геращенко А. С.

Несприятливе постінфарктне ремоделювання міокарда є одним із ключових шляхів до формування хронічної серцевої недостатності. Попри те, що інгібітори натрій-глюкозного котранспортера-2 (НЗКТГ2) покращують клінічні результати при серцевій недостатності, дані щодо їхніх структурних ефектів за умови початку терапії після гострої фази ушкодження залишаються обмеженими. Мета дослідження – оцінити, чи послаблює відтерміноване призначення емпагліфлозину гістологічні ознаки ремоделювання та зменшує морфометричні індекси гіпертрофії кардіоміоцитів у щурів з ізопреналін-індукованим ушкодженням міокарда. Шістдесят самців білих безпородних щурів (200-250 г) розподілили на три групи (n=20 у кожній): інтактний контроль, ізопреналін (ISO) + плацебо та ISO + емпагліфлозин. Ушкодження міокарда моделювали введенням ISO (85 мг/кг/добу, підшкірно, у дні 0 і 1). Починаючи з 14-го дня тварини отримували емпагліфлозин (10 мг/кг/добу перорально через зонд) або носій протягом 30 днів. Серця вилучали на 44-й день. Зрізи лівого шлуночка відбирали із субендокардіального, інтрамурального та субепікардіального шарів і забарвлювали гематоксиліном-еозином та за Массоном. Цифровою морфометрією визначали площу кардіоміоцита та площу ядра. Статистичний аналіз виконували із використанням програмного забезпечення IBM SPSS 26.0 (IBM, США). Встановлено, що ISO спричиняв мікросудинний застій, інтерстиціальний набряк, дезорганізацію кардіоміоцитів і посилене відкладання колагену при забарвленні за Массоном. Відтермінований емпагліфлозин зменшував якісну вираженість ушкодження та послаблював морфометричні ознаки гіпертрофії. Площа кардіоміоцита була більшою у групі ISO + плацебо, ніж у контролі (342,8±12,5 мкм² проти 223,2±8,4 мкм²; p<0,01) і зменшувалась при застосуванні емпагліфлозину (287,4±8,3 мкм²; p<0,05 порівняно з ISO + плацебо), залишаючись вищою за контроль. Площа ядра змінювалася подібно (36,95±1,07 мкм² проти 20,73±0,54 мкм² у ISO + плацебо та 26,81±0,65 мкм² при емпагліфлозині). Отримані результати дозволяють зробити висновок, що відтермінове призначення емпагліфлозину після експериментального ушкодження міокарда частково послаблює структурне ремоделювання та морфометричні ознаки гіпертрофії кардіоміоцитів.

Ключові слова: *емпагліфлозин, морфологія, ремоделювання міокарда, ізопреналін, фіброз, морфометрія, серцева недостатність.*

Author's contribution

Kozan I. I. – acquisition of data, analysis and interpretation of data, drafting the article.
Fedorov S. V. – conception and design of the study, final approval.
Kozan N. M. – analysis and interpretation of data, critical revising.
Herashchenko A. S. – analysis and interpretation of data.

DOI: 10.31393/morphology-journal-2026-32(1)-05 Reports of Morphology, Vol. 32, №1, Pages 32-37

ISSN 1818-1295 eISSN 2616-6194

REPORTS OF MORPHOLOGY

Official Journal of the Scientific Society of Anatomists, Histologists, Embryologists and Topographic Anatomists of Ukraine

journal homepage: https://morphology-journal.com

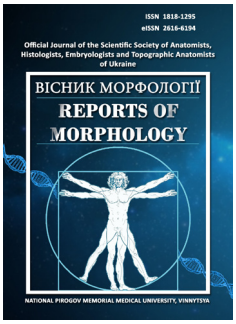

Pathomorphological changes in the thyroid gland due to combined gunshot lesions

Khoroshun E. M.[1,2], Makarov V. V.[1,2], Vorovskiy O. O.[4], Misyura K. V.[3], Negoduiko V. V.[1,2], Chernobil B. M.[1]

[1] Military Medical Clinical Center of the Northern Region of the Command of the Medical Forces of the Armed Forces of Ukraine, Kharkiv, Ukraine

[2] Kharkiv National Medical University, Kharkiv, Ukraine

[3] SI "Institute of Endocrine Pathology named after V. Ya. Danylevskyi of the National Academy of Medical Sciences of Ukraine", Kharkiv, Ukraine

[4] Vinnytsia National Pirogov Memorial Medical University, Vinnytsia, Ukraine

ARTICLE INFO

Received: 22 July 2025

Accepted: 26 December 2025

UDC: 616-001.45616.441

CORRESPONDING AUTHOR

e-mail: vorovskiysurgery@ukr.net

Vorovskiy O. O.

CONFLICT OF INTEREST

The authors have no conflicts of interest to declare.

FUNDING

Not applicable.

DATA SHARING

Data are available upon reasonable request to corresponding author.

Modern military conflicts are accompanied by gunshot injuries affecting all parts of the body. The thyroid gland is located near the carotid arteries, internal jugular veins, esophagus, larynx, and trachea. Injury to these structures creates the potential for rapid airway compromise due to compression or bleeding from adjacent tissues, while the thyroid gland itself may also serve as a potential source of hemorrhage. When determining the extent of surgical intervention, it is not always possible to clearly define the exact boundaries of a gunshot injury. This issue can be addressed by conducting pathomorphological studies of the damaged area of the thyroid gland. The aim was to study the pathomorphological changes of the thyroid gland in gunshot injuries in order to determine the volume of surgical intervention. The treatment outcomes of combatants with gunshot injuries to the thyroid gland, which accounted for 7.4 %, were analyzed. Of this number, 28.6 % of wounded patients with grade III and IV thyroid injuries were included in the group that underwent pathomorphological examination. For pathomorphological analysis, upon delivery of the material from the mobile hospital (Role 2), preliminary freezing of tissues was performed by immersion in liquid nitrogen followed by fixation in 96 % ethanol. After paraffin processing of the material from the damaged areas of the thyroid gland, sections 4-5 μm thick were prepared and stained with hematoxylin and eosin. The set of pathomorphological studies was carried out using a Primo Star microscope (Carl Zeiss) at ×280 magnification. Images were captured with a high-resolution digital camera with 8-bit digitization, AxioCam (ERc 5s), with a pixel size of 2.2 μm and Carl Zeiss AxioCam (ERc5s) Configuration Tool software. The examinations revealed large macrohemorrhages beneath the capsule and within thyroid follicles with partial destruction. The presence of colloid vacuolization within the follicular lumen indicated the onset of destructive changes in the follicle itself; however, on the 5th day after injury, partially destroyed follicles demonstrated a reverse process. In cases of complete destruction of the follicular wall, there was a high risk of hormone release into the bloodstream with subsequent development of "thyrotoxic storm" and acute mental disorder. Thus, the thyroid gland demonstrated the ability to undergo regenerative changes 4-5 days after injury, indicating the necessity of performing primary surgical wound debridement and subsequent necrectomies only within the boundaries of damaged tissues.

Keywods: *thyroid gland, gunshot injury, pathomorphological changes of the follicle, thyrocyte.*

Introduction

Since 2014, Russian military aggression against the people of Ukraine has been ongoing. During this time, Russia has continuously developed and improved various types of high-energy weapons, the use of which results in severe injuries among servicemen of the Armed Forces of Ukraine and the civilian population [9, 13, 16, 20]. Tissue

damage caused by gunshot wounds occurs through three mechanisms: direct impact or crushing, shock waves, and temporary cavitation. The cavitation effect extends to an area approximately 20-30 times greater than the bullet diameter. The cavity formed by this phenomenon, especially in parenchymal organs, causes significant injury around the wound channel, where, due to microcirculatory damage, a secondary zone of necrosis develops that cannot be identified during the initial examination [3]. Although these mechanisms are well described in the literature, the development of new weapons and advances in protective armor have significantly altered injury patterns and their anatomical distribution.

Neck trauma has long been of professional interest to trauma surgeons. The first data on combat injuries to this region were collected during the American Civil War (1861-1865), when more than 4,000 neck wounds were recorded with a mortality rate exceeding 35 % without surgical intervention [15]. Although the neck accounts for only 1 % of total body surface area, according to some authors it disproportionately accounts for 16-39 % of injuries. The neck contains vital structures including major blood vessels, nerves, and the upper airway. Moreover, unlike the head or chest, the anatomical structure of the neck lacks natural protection. As a result, penetrating or blunt neck injuries have devastating consequences and are highly lethal in 41-73 % of cases [25]. Isolated neck injuries, according to some authors, account for up to 10 % of all injuries [18].

Due to a restrained approach to early surgical interventions, mortality in neck wounds at earlier stages of medical evacuation exceeded 54 %, and severe complications developed in nearly 80 % of the wounded. At present, some authors report that with surgical management of combat neck injuries, mortality does not exceed 2-6 % [23].

The neck contains vital structures including major blood vessels, nerves, and the upper aerodigestive tract. Zone II, located between the cricoid cartilage and the angle of the mandible, contains the carotid and vertebral arteries, internal jugular veins, esophagus, trachea, and cranial nerves X, XI, and XII, and is also the location of the thyroid gland [4, 6]. Injury to these structures creates the potential for rapid airway compromise due to direct trauma or indirectly through compression or hemorrhage from adjacent tissues, with the thyroid gland itself being a potential source of bleeding [10]. Previous studies of penetrating neck trauma have described thyroid injuries as rare and clinically insignificant [19, 23].

In peacetime, the incidence of thyroid gland injuries was <0.1 %. Among these, 59.7 % of patients had isolated thyroid injury, while in 40.3 % the injury was associated with damage to adjacent neck organs. Authors report that 75.8-85.6 % of these injuries had a penetrating mechanism [23]. Visual and instrumental assessment of injury extent does not always allow clear delineation of the boundaries of gunshot damage to the thyroid gland. This issue can be addressed by performing pathomorphological studies to determine the cause and extent of tissue damage specifically in gunshot injuries of the thyroid gland.

The aim of the study was to investigate the pathomorphological changes of the thyroid gland in gunshot injuries in order to determine the appropriate extent of surgical intervention.

Materials and methods

During the specified period, the proportion of combatants with gunshot injuries to the thyroid gland treated at the Military Medical Clinical Center of the Northern Region (Role 3) was 7.4 %, all of whom were male. The exact total number of wounded during this period cannot be disclosed, as these data are classified. All injured individuals were male, with a mean age of 32.0±1.5 years. In 45.6 % of cases, combined trauma was identified, including both gunshot injury and thermal damage. All gunshot wounds were penetrating in nature; 82.4 % were through-and-through wounds, and 17.6 % were blind wounds; 97.8 % were fragment injuries and 2.2 % were bullet wounds; in 47.1 % of cases, fragment injuries were associated with blast trauma.

Regarding the number of injuring agents, multiple injuries occurred in 79.4 % of cases, with a maximum of five metallic fragments; single injuries accounted for 20.6 %. The maximum fragment size reached 4.5×2.5 cm². In cases of single gunshot wounds, the external carotid artery was injured in 5.9 % of cases and the larynx in 2.9 %. In multiple gunshot injuries, the carotid artery was damaged in 27.9 % of cases, the jugular vein in 11.6 %, the pharynx in 41.2 %, the larynx in 23.5 %, the trachea in 10.3 %, the hyoid bone in 5.9 %, the esophagus in 4.4 %, and the thyroid gland in 7.4 % (it should be noted that the incidence of injuries to this organ is steadily increasing). The distribution of thyroid injuries by class was as follows: class I – 32.3 % (local and general conservative treatment), class II – 41.4 % (local treatment and primary surgical wound debridement; in the presence of hematoma and bleeding – hemostasis and hematoma drainage), class III – 20.7 % (thyroid necrectomy), class IV – 3.4 % (necrectomy performed twice).

To assess injury severity, the ISS scale (≥16) was applied, or in cases involving injury to two or more neck organs (corresponding to a score ≥3), the abbreviated injury scale (AIS) was used [24]. In this cohort, according to ISS scores, injury severity was moderate in 48.5 % of patients (ISS <16), severe in 33.8 % (ISS 16-25), and critical in 19.1% (ISS >25).

After admission, 72.1 % of the wounded underwent ultrasound examination of the soft tissues of the neck using a Logiq P8P910 device (USA, 2021) with a linear L3-12p probe operating at 3-12 MHz to determine the extent of injury. In cases of airway injury, 36.2 % of combatants underwent video bronchoscopy, and in suspected esophageal injury, 26.5 % underwent video esophagogastroduodenoscopy using an OLYMPUS CV-170 video endoscopy system (2017). Spiral computed tomography of the head, neck, chest, and abdominal organs was performed in 82.4 % of patients using a “Revolution EVO” scanner with a 0.5 mm slice thickness.

For histological examination, thyroid tissue obtained from the wound channel was fixed in 40 % neutral formalin and

processed according to standard pathological laboratory protocols (the authors express gratitude to the staff of the State Institution “Danilevsky Institute for Endocrine Pathology Problems of the NAMS of Ukraine” for assistance in conducting pathomorphological studies). Upon delivery of specimens from the mobile hospital (Role 2), tissues were preliminarily frozen by immersion in liquid nitrogen followed by fixation in 96 % ethanol. After paraffin processing of material from damaged thyroid areas, 4-5 μm sections were prepared and stained with hematoxylin and eosin. The complex of pathomorphological examinations was performed using a Primo Star microscope (Carl Zeiss) at ×280 magnification. Images were captured with a high-resolution 8-bit digital AxioCam (ERc 5s) camera with a pixel size of 2.2 μm using Carl Zeiss AxioCam (ERc5s) Configuration Tool software [16].

Statistical analysis of the obtained results was performed using Excel (Microsoft Office, USA).

Results

Primary surgical medical care for wounded combatants was initially provided at Role 1 (also known as unit-level medical care), where all efforts were focused on hemorrhage control; primary surgical wound management, including debridement and drainage of the gunshot wound; antibiotic prophylaxis; and infusion support. The wounded were subsequently transported to a mobile hospital (Role 2) of the Armed Forces of Ukraine in the Donetsk region, where repeated surgical wound debridement with limited necrectomy and attempts to remove metallic fragments using specialized magnetic instruments were performed in patients with mild and moderate injuries, while stabilization measures were provided for severely injured patients. In most cases, transportation was accomplished within the “golden hour.” After stabilization, severely wounded servicemen and other personnel with neck injuries were transferred to the Military Medical Clinical Center of the Northern Region (Role 3) for further examination and treatment. During videobronchoscopy, bronchial tree sanitation was performed, and in 3 patients (2.2 %), foreign bodies were removed from the bronchial lumen.

Normally, thyroid gland tissue consists of clusters of follicles, which are the structural and functional units of the gland. Follicles contain a cavity filled with homogeneous gelatinous material (colloid) [1] (Fig. 1). When stained with hematoxylin and eosin, the colloid appears pink, while follicular cells (thyrocytes) appear purple. The colloid consists of thyroglobulin, an iodinated glycoprotein that represents an inactive storage form of thyroid hormones [14]. The space between follicles is filled with connective tissue stroma, penetrated by fenestrated capillaries and lymphatic vessels, and contains parafollicular cells. The thyroid gland is the only endocrine gland whose secretory products are stored intracellularly within thyrocytes, which line the follicular wall as a single layer of cuboidal or columnar epithelium resting on a basement membrane.

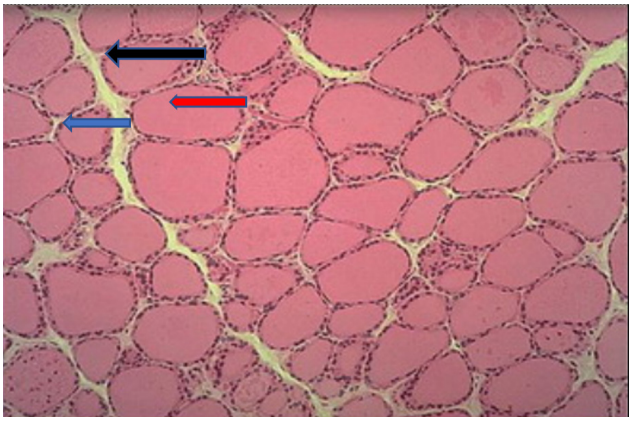

Fig. 1. Fragment of the thyroid gland with a follicle filled with colloid (red arrow), a single layer of follicular cells – thyrocytes (blue arrow), and parafollicular cells (black arrow). Hematoxylin-eosin staining. ×280.

As a result of gunshot injury, pathomorphological changes occur in the thyroid gland that are specific to this organ and determine the subsequent course of treatment. The excised portion of the thyroid gland with predominant gunshot destruction was subjected to histological examination (Fig. 2).

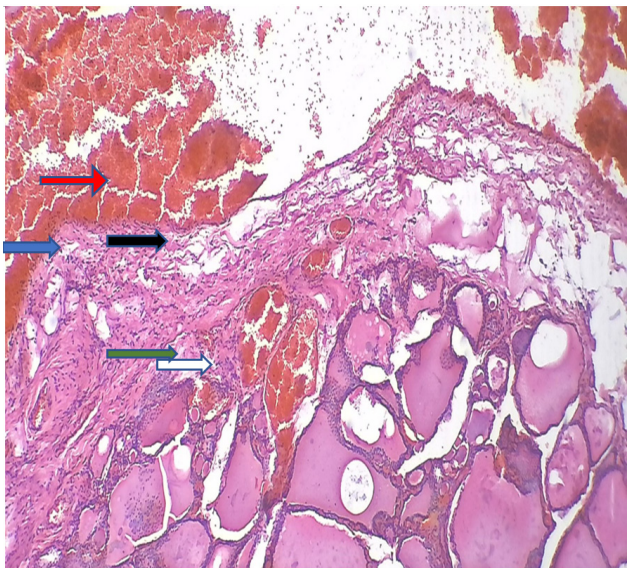

Fig. 2. Fragment of the thyroid gland after gunshot injury at the time of hospitalization: presence of large macrohemorrhages in the thyroid gland beneath the capsule (red arrow) and within the follicles (blue arrow); preserved follicles (white arrow); a destroyed follicle with preserved colloid (black arrow); vacuolization of the colloid (green arrow). Hematoxylin-eosin staining. ×280.

Macroscopic examination revealed the presence of a subcapsular hematoma. Histological analysis demonstrated blood infiltration of thyroid tissue, with large macrohemorrhages beneath the capsule and within follicles accompanied by partial destruction. In damaged follicles, thyrocytes resting on a thickened basement membrane transformed from cuboidal or columnar to flattened

epithelium. The presence of colloid vacuolization within the follicular lumen indicated the onset of destructive changes in the follicle itself; however, the possibility of a reversible process remained. In cases of complete destruction of the follicular wall, hormone release into the bloodstream may occur, potentially leading to the development of a “thyrotoxic storm” [17] and acute mental disorder.

Investigation of thyroid tissue pathomorphosis allows understanding of the evolution of structural changes after gunshot injury. On the 5th day of hospitalization, extracapsular macrohemorrhage was detected, along with destructive follicular changes manifested by fibrotization of the follicular wall with closure of its lumen (irreversible pathomorphological changes), as well as follicles with preserved lumens (indicating possible anatomical and functional recovery) (Fig. 3).

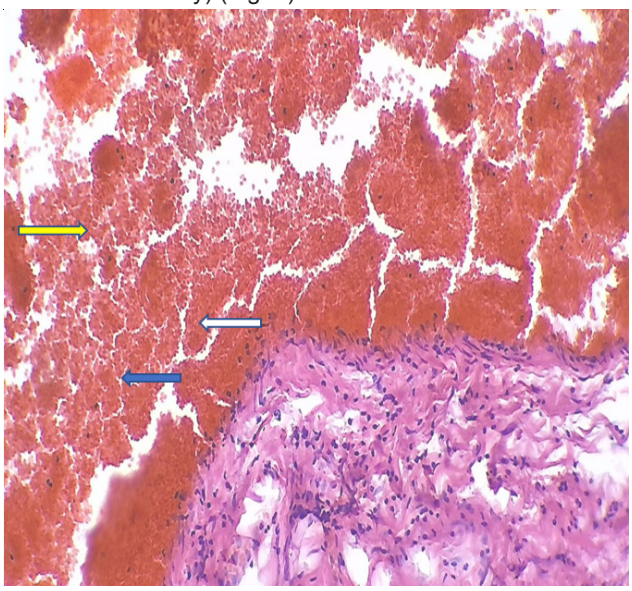

Fig. 3. Fragment of the thyroid gland after gunshot injury on day 5: extracapsular macrohemorrhage extending beyond the capsule (yellow arrow), complete destruction of follicles and their walls with preservation of volume (blue arrow), fibrotization of follicular walls (white arrow). Hematoxylin-eosin staining. ×280.

All patients underwent surgical interventions that included necrectomy with removal of remaining metallic fragments that could not be extracted using specially designed magnetic instruments at previous levels of care. When feasible, cartilage and pharyngeal reconstruction was performed. Surgical management also included thyroid necrectomy of varying extent, followed by drainage of the postoperative wound and, when necessary, creation of a lower tracheostomy.

Discussion

Thus, in cases of gunshot injury to thyroid gland, we identified large macrohemorrhages beneath the capsule and within the follicles with partial destruction of the latter. The presence of colloid vacuolization within the follicular lumen indicates the onset of destructive changes in the follicle. However, on the 5th day after gunshot injury, the thyroid gland demonstrated the capacity for regenerative changes. In cases of complete destruction of the follicular wall, there was a high risk of hormone release into the bloodstream with subsequent development of “thyrotoxic storm” and acute mental disorder.

We consider this study relevant and timely, as the global literature reports an increase in gunshot injuries to the neck with thyroid involvement from 3.2 % [17] to 13.8-20 % of all gunshot injuries, which corresponds to our findings (7.4 %) and allows us to present our own experience in the diagnosis and management of this pathology.

Due to the close anatomical proximity of vital structures in the neck, which may be simultaneously injured during gunshot trauma, mortality rates range from 35-36 % to 54-58 % of all fatal cases [26]. The primary cause of mortality in penetrating neck trauma is uncontrolled hemorrhage. It is believed that prolonged bleeding, particularly with the development of hemorrhagic shock, leads to hypothermia, coagulopathy, and acidosis, the so-called lethal triad resulting in irreversible systemic changes [7]. However, some authors suggest that the lethal triad does not always directly lead to death, emphasizing acidosis associated with severe hypoxemia and tissue hypoxia. These authors consider tissue hypoxemia, acidosis, and ischemia-reperfusion toxemia to be the main causes of death in hemorrhagic shock [5]. In our opinion, this is more characteristic of prolonged bleeding or its consequences.

The thyroid gland ranks first among organs in terms of blood flow per unit mass. Its blood supply is primarily provided by the paired superior and inferior thyroid arteries [8]. In 3-10 % of individuals, an unpaired artery, the “Neubauer artery” (a. thyroidea ima), arises from the aortic arch or brachiocephalic trunk [12]. Neck wounds are characterized by the impossibility of applying a tourniquet. Continued bleeding within a confined space may result in the formation of a compressive hematoma and venous obstruction, potentially leading to impairment of the parathyroid glands or laryngeal nerves. Subsequently, such hematomas may become infected and cause the development of neck phlegmon. Advanced hemostatic patches that form covalent bonds with moist tissues, as well as active patches containing biochemical agents that promote coagulation, demonstrate significantly greater hemostatic effectiveness compared to compression-only dressings [21]. Recently, hemostatic dressings containing clotting activators (fibrinogen, thrombin, etc.) have been developed. Studies have shown that the use of such dressings at the prehospital stage achieves hemostasis in 90.5 % of cases [22]. This approach has enabled the transfer of up to 70 % of patients with vascular injuries from Role 1 to Role 2 without profuse bleeding.

Patients with hemodynamic instability underwent emergency surgery. In determining surgical tactics, entry and exit wound sites were considered in cases of minor injuries. The trajectory of the wound tract and the extent of damage were assessed using preoperative computed tomography

[27], which was performed in 82.4 % of patients. Isolated thyroid injury is extremely rare and occurs in approximately 1-2 % of cases. In the studied cohort, no isolated thyroid injuries were identified, which was confirmed by preoperative computed tomography.

During removal of foreign bodies (metal fragments) located in high-risk areas of the neck, in order to prevent damage to vital anatomical structures, fragments were extracted either by palpation or using specialized magnetic instruments through separate surgical approaches [2].

Conclusions

1. The study of pathomorphological changes of the thyroid gland after gunshot injury demonstrated that damage to follicles and release of colloid into the bloodstream may lead to the development of a delayed “thyrotoxic storm”.

2. The thyroid gland was found to have the capacity for regenerative changes beginning 4-5 days after injury, indicating that primary surgical wound debridement and subsequent necrectomies should be performed strictly within the boundaries of damaged tissues.

3. In cases of combined thyroid gland injuries involving adjacent organs, preoperative computed tomography should be performed to determine the appropriate treatment strategy and to prevent additional anatomical damage.

References

[1] Al-Suhaimi, E. A., & Khan, F. A. (2022). Thyroid glands: Physiology and structure. In *Emerging concepts in endocrine structure and functions* (pp. 133-160). Singapore: Springer Nature Singapore. doi: 10.1007/978-981-16-9016-7_5

[2] Bäckman, P. B., Riddez, L., Adamsson, L., & Wahlgren, C. M. (2020). Epidemiology of firearm injuries in a Scandinavian trauma center. *European Journal of Trauma and Emergency Surgery*, *46*(3), 641-647. doi: 10.1007/s00068-018-1045-1

[3] Baum, G. R., Baum, J. T., Hayward, D., & McKay, B. J. (2022). Gunshot wounds: ballistics, pathology, and treatment guidelines, with emphasis on bullet residue. *Orthopaedic Research and Reviews*, *14*, 293. doi: 10.2147/ORR.S378278

[4] Bodnar, Ya. Ya., & Faifura, V. V. (2020). *Патологічна анатомія і патологічна фізіологія людини: Підручник [Pathological anatomy and pathological physiology of human: Textbook]*. Тернопіль: Укрмедкнига=Ternopil: Ukrmedknyga.

[5] Bonanno, F. G. (2023). Debunking the lethal triad and delineating damage control surgery. *Minerva Surg*, *78*(6), 692-709. doi: 10.23736/S2724-5691.23.09916-1

[6] Chorna, V. V., Fedotova, V. V., Kolomiyets, V. V., Lypkan, V. M., Rybinsky, M. V., Savichan, K. V., & Gudzevych, L. S. (2025). Comprehensive analysis of scientific studies of penetrating neck injuries in the world and Ukraine. *Trauma*, *26*(1), 11-20. doi: 10.22141/1608-1706.1.26.2025.994

[7] Ditzel, Jr. R. M., Anderson, J. L., Eisenhart, W. J., Rankin, C. J., DeFeo, D. R., Oak, S., & Siegler, J. (2020). A review of transfusion-and trauma-induced hypocalcemia: is it time to change the lethal triad to the lethal diamond? *Journal of Trauma and Acute Care Surgery*, *88*(3), 434-439. doi: 10.1097/TA.0000000000002570

[8] Gebara, M. (2025). Superior Thyroid Artery. In *The Clinical Anatomy of the Vascular System* (pp. 69-72). Cham: Springer Nature Switzerland. doi: 10.1007/978-3-031-78326-5_7

[9] Gybalo, R. V., Lurin, I. A., Safonov, V., Dudla, D. I., Oklei, D. V., & Dinets, A. (2022). Retained bullet in the neck after gunshot wounds to the chest and arm in combat patient injured in the war in Ukraine: a case report. *International Journal of Surgery Case Reports*, 99. doi: 10.1016/j.ijscr.2022.107658

[10] Huang, S. S., & Lien, W. C. (2022). Successful nonoperative management of a traumatic bilateral thyroid hemorrhage following blunt neck trauma. *Journal of Emergencies, Trauma, and Shock*, *15*(4), 186-187. doi: 10.4103/jets.jets_157_21

[11] Jasim, S., Dean, D. S., & Gharib, H. In: Feingold, C. R., Ahmed, S. F., Anawalt, B., … & Wilson. D. P. (2023). Fine-needle aspiration of the thyroid gland. *Endotext [Internet]. South Dartmouth (MA): MDText.com, Inc; 2000*. PMID: **25905400**

[12] Kapral N., & Khot R. (2022). Thyroid anatomy and ultrasound evaluation. *Techniques in Vascular and Interventional Radiology*, *25*(2), 100818. doi: 10.1016/j.tvir.2022.100818

[13] Kazmirchuk, A., Yarmolyuk, Y., Lurin, I., Hybalo, R., Buryanov, O., Derkach, S., & Karpenko, K. (2022). Ukraine’s experience in managing casualties from combat operations using the NATO four-tier health care system “Changes as needed”. *World Journal of Surgery*, *46*(12), 2858-2862. doi: 10.1007/s00268-022-06718-3

[14] Lishchuk, O. Z., Suslyk, G. I., Safonova, O. V., & Lishchuk, B. F. (2021). Current views on the main metabolic and regulatory effects of thyroid hormones: (literature review). *Achievements of Clinical and Experimental Medicine*, (1), 12-16. doi: 10.11603/1811-2471.2021.v.i1.11988

[15] Loss, L., Henry, R., White, A., Matsushima, K., Barrett, C., Lammers, D., ... & Inaba, K. (2025). Penetrating neck trauma: a comprehensive review. *Trauma Surgery & Acute Care Open*, *10*(1). doi: 10.1136/tsaco-2024-001619

[16] Lurin, I., Burianov, O., Yarmolyuk, Y., Klapchuk, Y., Derkach, S., Gorobeiko, M., & Dinets A. (2024). Management of severe defects of humerus in combat patients injured in Russo-Ukrainian war. *Injury*, *55*(2). doi: 10.1016/j.injury.2023.111280

[17] Pickering, C., Muzaffar, J., Reid, C., Zakaria, B., Coulson, C., Sharma, N., & Breeze, J. (2023). Management and outcomes of military penetrating neck injuries: an eleven-year retrospective case note review. *Injury*, *54*(1), 119-123. doi: 10.1016/j.injury.2022.11.034

[18] Reina-Sepulveda, F., Cantu-Alejo, D., Martínez-Fernández, A., Rodríguez-Garcia, H., Guevara-Charles, A., Pérez-Rodríguez, E., ... & Muñoz-Maldonado, G. (2022). 5-year treatment and outcomes of penetrating neck injury in the emergency department. Penetrating neck injury. *Cirugía Española*, *100*(10), 629-634. doi: 10.1016/j.ciresp.2021.06.009

[19] Rodriguez-Ortiz, L. R., Perez-Torres, A. M., Saldaña-Mendez, A. N., & Labat-Alvarez, E. J. (2021). A rare case of traumatic thyroid gland hypoperfusion/devascularization after a gunshot wound through the neck: computed tomography findings. *The American Journal of Case Reports*, *22*, e930505-1–e930505-5. doi: 10.12659/AJCR.930505

[20] Rogovskyi, V. M., Koval, B., Lurin, I. A., Gumeniuk, K., Gorobeiko, M., & Dinets, A. (2023). Temporary arterial shunts in combat patient with vascular injuries to extremities wounded in Russian-Ukrainian war: a case report. *International Jour-*

nal of Surgery Case Reports, *102*, 107839. doi: 10.1016/j.ijscr.2022.107839

[21] Scerrino, G., Richiusa, P., Graceffa, G., Lori, E., Sorrenti, S., & Paladin, N. C. (2022). Recent Advances in Thyroid Surgery. *Journal of Clinical Medicine*, *11*(23), 7233. doi: 10.3390/jcm11237233

[22] Simpson, C., Tucker, H., & Hudson, A. (2021). Pre-hospital management of penetrating neck injuries: a scoping review of current evidence and guidance. *Scandinavian Journal of Trauma, Resuscitation and Emergency Medicine*, *29*(1), 137. doi: 10.1186/s13049-021-00949-4

[23] Spencer, D., Grigorian, A., Schubl, S., Awad, K., Elfenbein, D., Dogar, T., & Nahmias, J. (2019). Thyroid trauma – a national analysis of incidence, mortality, and concomitant injury. *Journal of Surgical Research*, *242*, 200-206. doi: 10.1016/j.jss.2019.04.042

[24] Su, W. T., Rau, C. S., Chou, S. E., Tsai, C. H., Liu, H. T., Hsu, S. Y., & Hsieh, C. H. (2022). Association between Elevated De Ritis Ratio and mortality outcome in adult patients with Thoracoabdominal Trauma. *Healthcare (Basel)*, *10*(10), 2082. doi: 10.3390/healthcare10102082

[25] Tsur, N., Dudkiewicz, D., Talmy, T., Radomislensky, I., Givon, A., Katorza, E., ... & Shapira, S. (2025). Battlefield Neck Injuries: Contemporary Insights From the Israeli National Trauma Registry. *JACEP Open*, *6*(4), 100211. doi: 10.1016/j.acepjo.2025.100211

[26] Usenko, O. Yu., Lurin, I. A., Gumenyuk, K. V., Negoduiko, V. V., Mykhaylusov, R. M., Ryzhenko, A. P., & Salyutin, R. V. (2022). Use of surgical magnetic instruments for the diagnosis and removal of ferromagnetic foreign bodies of the abdominal cavity in combat gunshot trauma. *Clinical Surgery*, *89*(7-8), 30-34. doi: 10.26779/2522-1396.2022.7-8.30

[27] Velioglu, Y., Yuksel, A., & Durgun, B. (2018). Gunshot injury of head and neck region with an atypical bullet trajectory: the importance of whole body computed tomography scan. *J Coll Physicians Surg Pak*, *28*(9), S215-6. doi: 10.29271/jcpsp.2018.09.S215

ПАТОМОРФОЛОГІЧНІ ЗМІНИ ЩИТОПОДІБНОЇ ЗАЛОЗИ ВНАСЛІДОК КОМБІНОВАНИХ ВОГНЕПАЛЬНИХ УРАЖЕНЬ

Хорошун Е. М., Макаров В. В., Воровський О. О., Місюра К. В., Негодуйко В. В., Чернобіль Б. М.

Сучасні військові конфлікти супроводжуються вогнепальними травмами всіх частин тіла. Щитоподібна залоза розташована поблизу сонних артерій, внутрішніх яремних вен, стравоходу, гортані, трахеї. Травма даних структур створює потенціал для швидкого порушення прохідності дихальних шляхів через стиснення чи кровотечі з сусідніх структур, де і сама щитоподібна залоза також є потенційним джерелом кровотечі. При визначенні об'єму оперативного втручання не завжди можна вказати на чітку межу вогнепального пошкодження. Вирішити дану проблему можливо провівши патоморфологічні дослідження ушкодженої ділянки щитоподібної залози. Мета – вивчити патоморфологічні зміни щитоподібної залози при вогнепальному пораненні для визначення об'єму хірургічного втручання. Були вивчені результати лікування бійців з вогнепальним пораненням щитоподібної залози, що склали 7,4 %. Від даної кількості в групу, яким було проведено патоморфологічне дослідження, увійшли 28,6 % поранених з III та IV класами пошкодження щитоподібної залози. Для проведення патоморфологічного дослідження при доставці матеріалу з мобільного шпиталю (Role 2) проводили попереднє заморожування тканин шляхом занурення тканин у рідкий азот з наступною фіксацією в 96 % спирті. Після парафінової обробки матеріалу із пошкоджених ділянок щитоподібної залози виготовляли зрізи товщиною 4-5 мкм, які забарвлювали гематоксиліном та еозіном. Комплекс патоморфологічних досліджень проводився на мікроскопі Primo Star (Carl Zeiss) зі збільшенням ×280 разів. Зображення подавались на цифрову камеру високої роздільної здатності 8-бітного оцифрування AxioCam (ERc 5s) з розміром пікселя 2,2 мкм та програмним забезпеченням Carl Zeiss AxioCam (ERc5s) Configuration Tool. При проведенні даних досліджень виявлені великі макрокрововиливи під капсулу та у фолікули щитоподібної залози з частковою їх руйнацією. Наявність вакуолізації колоїду в просвіті фолікула свідчила про початок деструктивних змін самого фолікула, проте на 5 добу після травми у фолікулах, які були частково зруйновані, спостерігався зворотній процес. При повній руйнації стінки фолікула був високий ризик викиду гормонів у кров'яне русло з наступним розвитком «тиреотоксичного шторму» та гострого психічного розладу. Таким чином, встановлена здатність щитоподібної залози піддаватись регенеративним змінам через 4-5 діб після пошкодження, що вказує на необхідність виконання первинної хірургічної обробки ран та наступних некректомій тільки в межах пошкоджених тканин.

Ключові слова: *щитоподібна залоза, вогнепальне поранення, патоморфологічні зміни фолікула, тиреоцит.*

Author contribution

Khoroshun E. M. – project administration.
Makarov V. V. – supervision, formal analysis and validation.
Vorovskyi O. O. – methodology and writing of the original draft; review writing and editing.
Mysiura K. V. – research, review writing and editing, data visualization.
Negoduiko V. V. – conceptualization, research, data visualization.
Chernobyl B. M. – resources, software.

DOI: 10.31393/morphology-journal-2026-32(1)-06 Reports of Morphology, Vol. 32, №1, Pages 38-46

ISSN 1818-1295 eISSN 2616-6194

REPORTS OF MORPHOLOGY

Official Journal of the Scientific Society of Anatomists, Histologists, Embryologists and Topographic Anatomists of Ukraine

journal homepage: https://morphology-journal.com

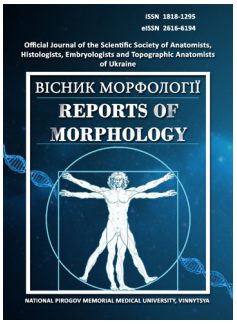

Osteoimmunomodulation by functional protective coatings: tuning innate and adaptive immunity for titanium implant osseointegration

Bondarenko O. O., Rolduhina M. O., Bondarenko N. S., Maltsev I. O., Loskutov O. Y., Shpon'ka I. S.

Dnipro State Medical University, Dnipro, Ukraine

ARTICLE INFO

Received: 11 August 2025

Accepted: 6 January 2026

UDC: 617.3:616-091.8:616.71-089.28:615.462

CORRESPONDING AUTHOR

e-mail: bondarenko.olexandr@dmu.edu.ua Bondarenko O. O.

CONFLICT OF INTEREST

The authors have no conflicts of interest to declare.

FUNDING

This study was a part of the research project "Molecular-genetic and morphological features of reparative bone regeneration using functional-protective coatings of implant materials" with governmental funding, state number of registration 0119U101119.

DATA SHARING

Data are available upon reasonable request to corresponding author.

The long-term clinical reliability of intraosseous implants is often compromised by aseptic loosening, an implant failure mode driven by chronic inflammation and fibrous encapsulation. Current evidence suggests that osseointegration relies on complex osteoimmunological interactions rather than mechanical interlocking. This study aimed to investigate the immunomodulatory effects of functional protective coatings, specifically bioactive hydroxyapatite (HAp) and bio-inert alumina (Al2O3), on the interplay between innate and adaptive immune responses. A rat femoral model (n=160) was utilized, featuring seven distinct implant surface configurations varying in roughness (Ra 1.89-23.7 μm) and chemical composition. Peri-implant bone tissue harvesting was conducted at 1, 2, 4, and 8 weeks to capture the progression from acute to chronic inflammatory stages. The methodology employed a comprehensive immunohistochemical (IHC) analysis using specific markers: CD3 for T-cells, CD25 for activated lymphocytes, CD45R for B-cells, CD68 for pan-macrophages, and CD163 for the reparative M2 phenotype of macrophages. Statistical validation involved non-parametric Kruskal-Wallis analysis with Dunn's post-hoc correction and Spearman's rank correlation to quantify topographic versus chemical influences. Persistent T-cell-mediated inflammation characterized the peri-implant environment of the titanium control groups; regardless of surface roughness, these implants exhibited elevated densities of activated T-cells (CD3+/CD25+) sustained through the eighth week, confirming a chronic inflammation. Established bioactive HAp coatings significantly suppressed adaptive immune activation, promoting a decisive phenotypic shift toward reparative M2 macrophages (CD163+) and facilitating early woven bone formation by week 4. A distinct immunogenic failure mode was observed in the hybrid alumina-titanium coating group (TSPTC), where mechanical instability led to the release of coating particles, triggering specific B-cell (CD45R+) infiltration, indicative of a pathological humoral reaction rather than physiological myelointegration. Impact assessed by correlative analysis revealed no significant association between surface roughness and immune cell infiltration, whereas an increasing bioactivity rank correlated negatively with adaptive immune cell densities, indicating the dominant role of surface chemistry over topography in resolving inflammation. Characterized by regularities in immune crosstalk, the data showed that T-cell density positively correlated with activation markers, while the HAp layer acted as an immunological buffer, effectively masking the titanium substrate to prevent autocrine amplification of inflammation. Our study underscores the critical importance of stable functional protective coatings in tuning the peri-implant immune environment. Specifically, these coatings play a pivotal role in overriding chronic adaptive immune signals and promoting M2 macrophage polarization, thereby establishing the pro-reparative microenvironment necessary for long-term osseointegration.

Keywords: *osteoimmunology, osseointegration, functional protective coatings, titanium implants, macrophage polarization, interleukin-2 receptor.*

Introduction

Osseointegration of intraosseous implants is no longer viewed only as a mechanical interlocking phenomenon but as

a complex biological cascade governed by the principles of osteoimmunology [29]. Successful peri-implant bone healing relies on a precise inflammatory sequence: an initial acute proinflammatory phase to recruit progenitor cells, followed by a timely transition to a reparative and anti-inflammatory environment [24]. Despite advancements in the last few decades, chronic implant failure remains a significant clinical challenge. In orthopedics, long-term aseptic loosening affects approximately 13 % of total hip arthroplasty patients over 25 years postoperatively, necessitating complex revision surgeries [5]. Similarly, in dentistry, peri-implantitis, a progressive inflammatory condition, affects nearly 20 % of patients, threatening the longevity of oral rehabilitation and imposing substantial healthcare costs [30]. The principal cause of such failures is frequently a dysregulated immune response, in which the inflammatory sequence described above is unsuccessful, that results in a long-term proinflammatory milieu and subsequent fibrous encapsulation, rather than effective osseointegration [12].

To address this challenge, implantology has introduced the concept of functional protective coatings, which are designed not only to mitigate mechanical problems, such as stress shielding [17], but also to harness their immunomodulatory properties essential for preventing chronic inflammation and guiding towards successful tissue regeneration [2, 26]. Among these, bioactive materials such as hydroxyapatite (HAp) are known for their osteoconductive properties and potential to modulate early immune responses [23], whereas ceramics such as alumina (Al_2O_3) offer excellent biocompatibility and mechanical stability, with emerging evidence suggesting their role in immune modulation [15]. Investigating these materials is crucial, given their widespread use and potential for advanced immunomodulatory designs.

Consequently, an effective functional protective coating must possess inherent anti-inflammatory properties and facilitate a rapid transition to a reparative immune phenotype, a challenge that current research is actively addressing [6]. To date, many studies in this direction were focused on the innate immune system, particularly the plasticity of macrophages (MPH). While functional protective coatings show promise in modulating innate immune responses through M2 MPH polarization [9, 16], a significant gap remains in understanding their impact on the adaptive immune system, which plays a crucial role in chronic bone implant failure. Recent evidence challenges the traditional view of titanium as biologically inert and suggests that titanium implants can elicit T cell-mediated immune responses under certain conditions [28]. The sustained activation of T- and B-cells stimulated by surface instability or particle release, can drive chronic inflammation and osteolysis [3]. This potential for activation of chronic inflammation presents a significant challenge in surface bioengineering. For instance, techniques such as plasma spraying, while increasing roughness (R_a) for enhanced mechanical anchorage, can indirectly exacerbate inflammation, thereby triggering a chronic adaptive immune response, as described by Kheder W. et al. [11].

This raises a pivotal question: can functional protective coatings, such as alumina or HAp, act as immunological buffers and preserve the beneficial topographic cues that tune M2 MPH while simultaneously dampening the adverse activation of T- and B-lymphocytes? This highlights the need to understand the complex interaction between implant materials and the adaptive immune system, which has yet to be fully elucidated and is only now gaining significant relevance due to the increased focus on the role of T-regulatory lymphocytes (Tregs) in recent studies [27, 29].

We hypothesized that functional protective coatings, particularly alumina and HAp ceramics, combine their unique chemical properties with a specific surface topography to form an anti-inflammatory microenvironment, with increased M2 polarization and reduced infiltration of T- and B-cells, which decreases peri-implant inflammation.

Accordingly, the primary *objective* of this study was to investigate the immunomodulatory effects of functional protective coatings (Al_2O_3 and HAp) on both innate and adaptive immune responses, specifically focusing on T- and B-cell activation and their interactions with MPH polarization, using a comprehensive immunohistochemical approach on *in vivo* rat femoral model. The secondary objective was to assess a local bone tissue response to the experimental modifications of titanium implant surfaces, according to the standard protocols for pre-clinical *in vivo* evaluation of medical devices [10, 25].

Materials and methods

Implant fabrication and animal model. The detailed protocols for implant fabrication, surface characterization, surgical procedure, and animal housing have been described previously [4]. Briefly, seven groups of cylindrical titanium implants (15×1.5 mm) were manufactured with varying surface roughness (R_a 1.89-23.7 μm) and chemical compositions (titanium, alumina, and HAp) using sandblasting and plasma-spray technology. The experimental design is illustrated in figure 1.

This study utilized archived paraffin-embedded histological samples from a previously approved *in vivo* study (Biomedical Ethics Committee of Dnipro State Medical University meeting minutes No. 2 dated 26.10.19). Briefly, 160 female Wistar rats received intramedullary implants in the distal femur and were euthanized at 1, 2, 4, and 8 weeks post-surgery (n=5 per group/time point). Harvested bone specimens were fixed in 10 % neutral buffered formalin and demineralized with EDTA prior to paraffin embedding. The animals were divided into seven groups according to the implant type: Ti, untreated titanium; TS, sandblasted titanium; and sandblasted titanium with consequent various plasma-sprayed configurations (TSP, titanium powder; TSPC, alumina ceramics; TSPT, titanium wire; TSPTC, titanium wire and alumina; TSPH, HAp-ceramics). Twenty rats that received untreated and uncoated titanium (Ti) implants served as the control group, 20 rats from the TSPH group served as a comparative cohort

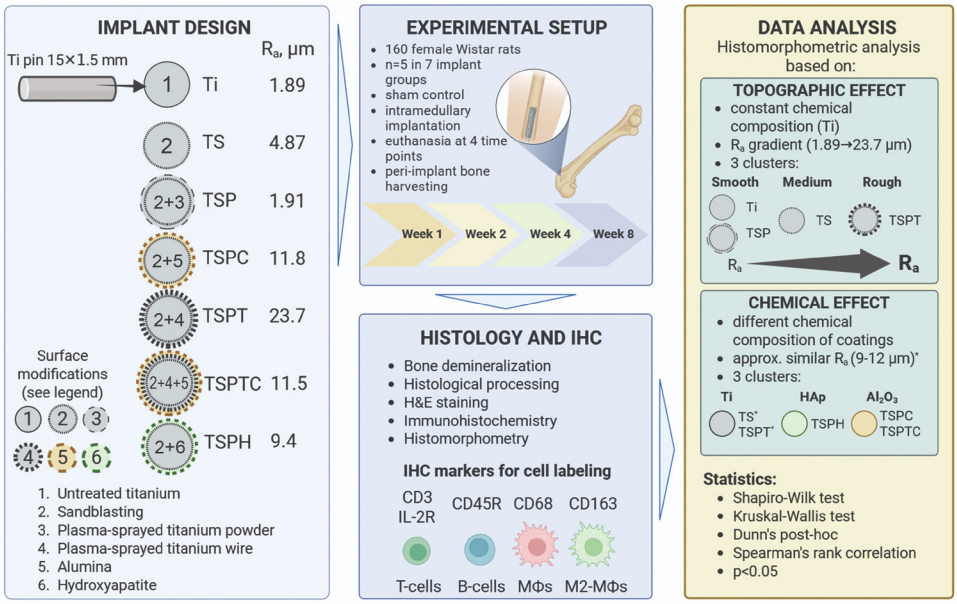

Fig. 1. Experimental workflow and analytical stratification. Left panel: Implant coatings were characterized by surface roughness (R_a 1.89-23.7 μm) and chemical composition (Ti, Al_2O_3, HAp). Middle panel: *In vivo* study design using a rat femoral model (n=160), with harvest points at 1, 2, 4, and 8 weeks for histological and immunohistochemical (IHC) profiling of macrophages (MPH), T-cells, and B-cells. Right panel: Statistical stratification strategy separating topographic effects (roughness gradient) from chemical effects, comparing Al_2O_3 and HAp coatings against Ti. Note: * – TS and TSPT were selected for chemical effect evaluation to serve as titanium reference controls; their roughness values bracket the ceramic groups (~9-12 μm), facilitating the dissociation of surface chemistry contributions from topographic cues.

with conventional HAp-coated implants, and another 20 animals formed the sham-operated group.

Histological and immunohistochemical analyses. 4-μm-thick sections were obtained from archived paraffin blocks using a Thermo HM 355S microtome (Thermo Fisher Scientific, Germany). Sections of each tissue sample were used for routine histological staining with hematoxylin and eosin (H&E) and for subsequent immunohistochemical (IHC) staining. For this purpose, they were mounted on adhesive slides (Superfrost, Thermo, Germany), deparaffinized with xylene, and rehydrated. Further procedures were performed according to the standard protocol [19]. The primary antibodies used were as follows: CD163 (rabbit monoclonal EPR19518, 1:500), CD25/IL-2 receptor (rabbit polyclonal, 1:400), CD3 (rabbit monoclonal SP7, 1:150), CD45R/B220 (rabbit polyclonal, 1:2000), and CD68 (rabbit polyclonal, 1:1000; all antibodies, Abcam, United Kingdom). The sections were incubated with primary antibodies overnight at 4 °C in a humid chamber. Immunodetection was performed using the Master Polymer Plus Detection System (Master Diagnostica, Spain), followed by visualization with a diaminobenzidine (DAB) chromogen reaction in the presence of hydrogen peroxide and horseradish peroxidase, which produced a brown signal at the antigen binding sites. Counterstaining was performed using Gill's hematoxylin for 30 s. Finally, the sections were dehydrated in graded alcohols, cleared in xylene, and mounted under coverslips using a permanent mounting medium.

Microscopy and histomorphometry. Microscopy was performed using a ZEISS "AxioImager.A2" (Carl Zeiss AR, Germany) light microscope (×10, ×20, and ×40 objectives). Digital images and morphometric analyses were performed using ZEN 2 Blue Edition software (Carl Zeiss AR, Oberkochen, Germany). Tissue inflammation was evaluated using a semiquantitative scoring system for polymorphonuclear leukocytes (PNLs), MPH, and lymphocytes [10] as follows: (G0) absent; (G1) mild, up to 5 inflammatory cells per high power (×400) field (PHF); (G2) moderate, 5-10 inflammatory cells PHF; and (G3) severe, heavy inflammatory infiltrate.

Quantitative analysis of IHC marker expression was performed within a standardized region of interest (ROI) in the peri-implant tissue that remained after implant extraction. For each section, five separate ROIs were selected using high-power magnification (×400) to count the IHC-positive cells. The mean value of these ROIs was considered satisfactory for the representation of each specimen and was expressed as the number of cells per mm^2.

Statistical analysis. All statistical analyses were performed using GraphPad Prism software (version 8.2 (263); GraphPad Software, San Diego, CA, USA). Data are presented as mean ± standard deviation (SD). After assessing data normality using the Shapiro-Wilk test, differences between multiple experimental groups were evaluated using the Kruskal-Wallis test with Dunn's post-hoc correction.

To quantify the impact of the material composition, an ordinal bioactivity rank was assigned based on established chemical reactivity hierarchies [8]: titanium (bio-inert metal)=1; Al_2O_3 (bio-inert ceramic)=2; HAp (bioactive

ceramic)=3. Spearman's rank correlation was calculated in groups of implants with similar R_a that represented different coating composition (TS and TSPT – titanium, TSPC and TSPTC – alumina, TSPH – HAp) to determine the relationship between bioactivity ranks and immune cell density. Similarly, a correlation analysis was performed between the measured roughness values (R_a) of only the titanium-based groups (Ti, TSP, TS, TSPT) and the density of the corresponded immunolabeled cells to assess the relationship between roughness and inflammation. Statistical significance was set at $p<0.05$.

Results

Qualitative histological and immunohistochemical assessments. Histological analysis using H&E staining revealed changes in inflammatory and tissue repair events across all observational periods. In the acute phase (1-7 days), all experimental groups exhibited a provisional matrix composed of fibrin and erythrocytes with significant monocytic infiltration and scattered PNLs (Fig. 2 A). By week 2, all alumina- and titanium-based coating groups displayed a dense lymphomacrophagic infiltrate (G3) organized within a fibrous capsule (Fig. 2 B), whereas TSPH group showed early woven bone formation in small areas, replacing the fibro-inflammatory cuff. In the chronic phase (weeks 4-8), inflammation resolved to a mild, scattered profile (G1) in the TSPH group, where peri-implant areas were characterized by direct bone-to-implant contact (Fig. 2 C); conversely, the rough titanium (TS and TSPT), alumina and hybrid groups (TSPC and TSPTC) maintained persistent moderate inflammation (G2) containing a mixed lymphomacrophagic diffuse infiltrate with occasional foreign-body giant cells surrounding detached coating particles (Fig. 2 D).

Immunohistochemical analysis corroborated these morphological observations (Fig. 3).

By week 2, CD68-positive MPH (Fig. 3 J, K), and CD3-positive T-lymphocytes (Fig. 3 A, B), and $CD45R^+$ cells (Fig. 3 G, H) formed a diffuse 20-40-μm-thick inflammatory infiltrate localized amidst the fibrous tissue directly adjacent to the implant interface. $CD25^+$ cells were dispersed among the lymphocytic infiltrates (Fig. 3 D, E). CD163-positive M2-MPH were sparsely distributed within the fibrous tissue, predominantly in samples harvested after four weeks. At week 8, scattered $CD163^+$ M2 cells were still retained in a thin fibrous layer on the bone-free areas of the implant surfaces (Fig. 3 M, N). The cell distribution pattern was generally diffused with a gradient of increased cellularity towards the implant surfaces; however, in some cases, abundant foci of immune cells were found at a distance from the implant surface. In particular, the TSPTC group exhibited focal accumulations of MPH and dense $CD3^+/CD45R^+$ lymphocytic clusters, specifically localized near the detached coating

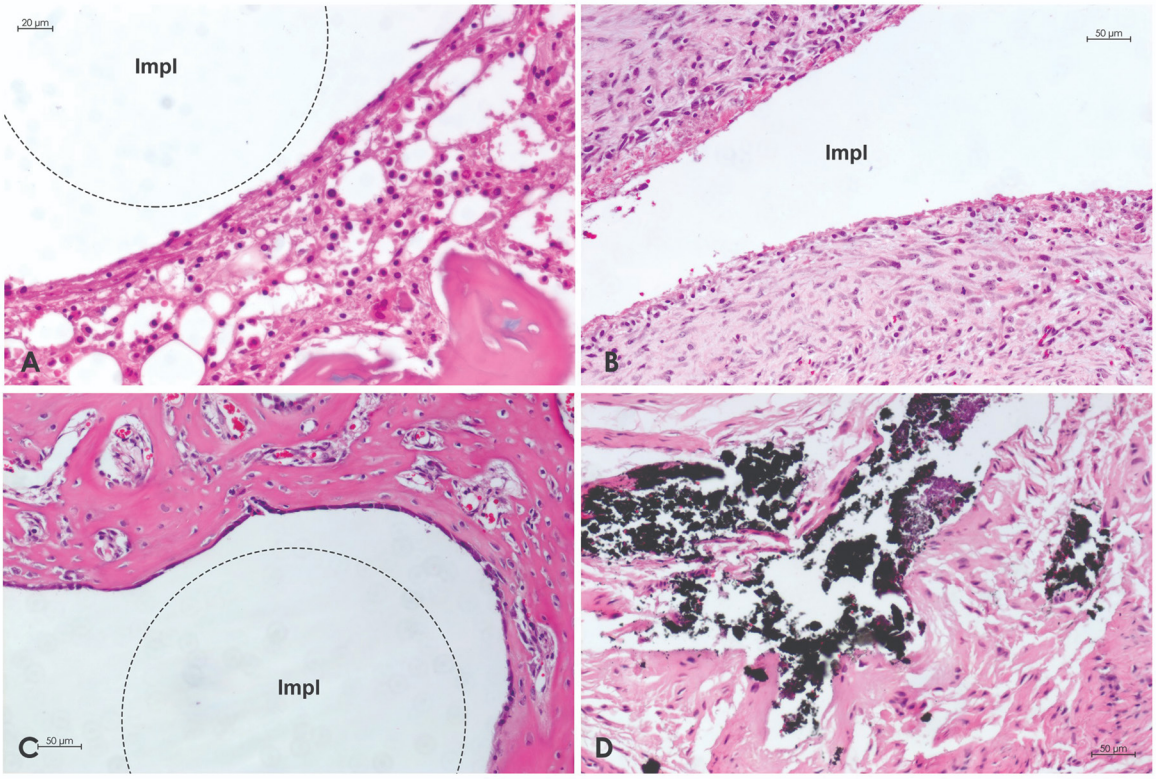

Fig. 2. Histological findings in the peri-implant zones of the studied animals. A – After 1 week of implantation, acute inflammation was still present around the implant (Ti group, ×4); B – prominent lymphomacrophagic infiltrate and fibrosis around the implant site after 2 weeks (TSPT group, ×200); C – peri-implant bone formation after 4 weeks in the TSPH group (×200); D – alumina coating debris with massive fibrosis and chronic inflammation (4 weeks, TSPTC, ×200). Notes: Impl, dashed circle – implant site. H&E staining.

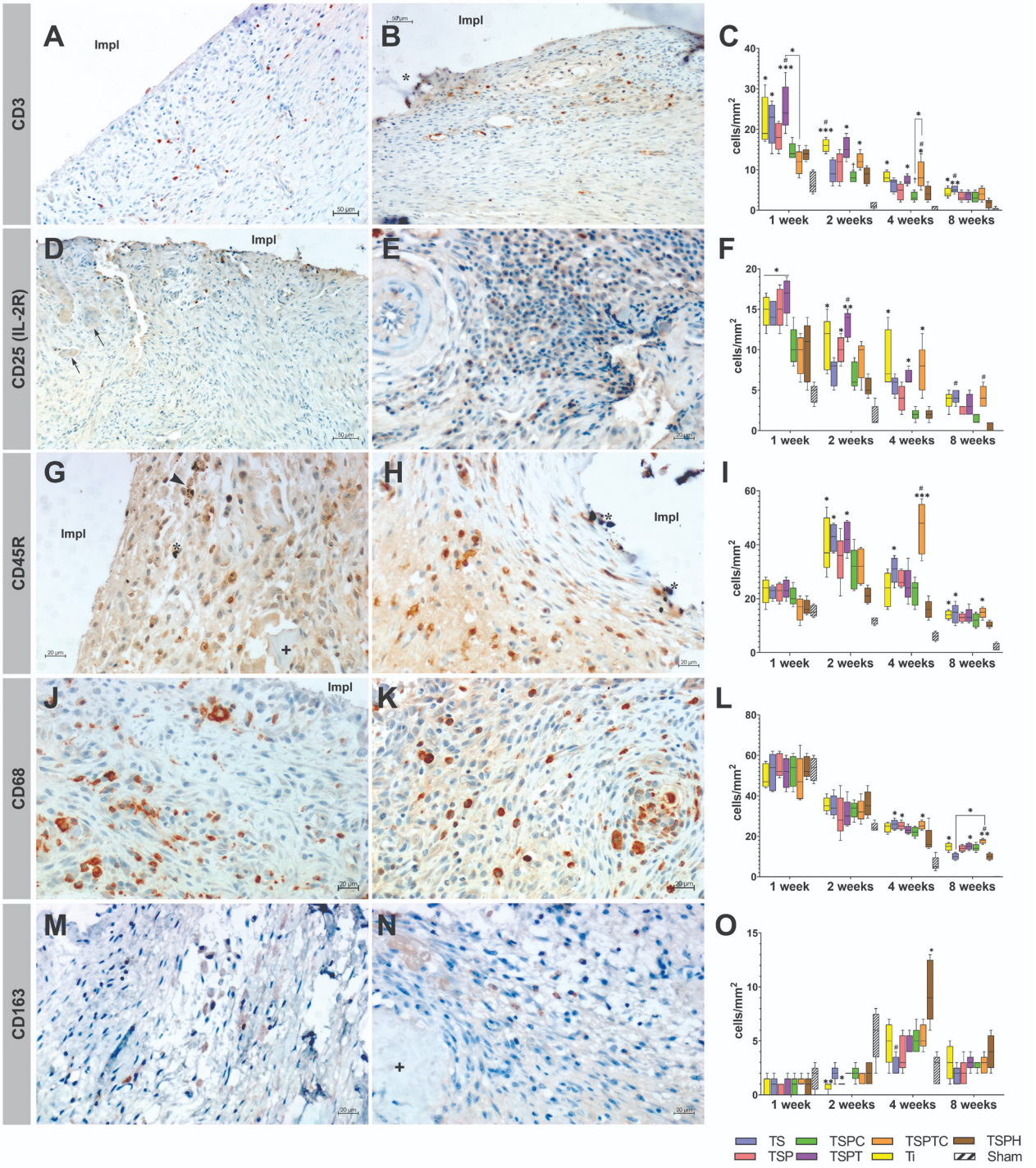

Fig. 3. Qualitative and quantitative immunohistochemical analyses of the peri-implant immune microenvironment. Representative micrographs (left/middle columns) and corresponding cellular density quantification (right column) over 8 weeks for: (A–C) T-cells (CD3); (D–F) activated T-cells (CD25/IL-2R); (G–I) B-cells (CD45R); (J–L) pan-macrophages (CD68); and (M–O) M2-polarized macrophages (CD163). Diffuse T-cell infiltration within the fibrous tissue after 2 weeks in the groups with Ti (A) and TSPC (B) implant surface modifications; expression of IL-2 receptor on lymphocytes of peri-implanted area around TS-modified implants after 2 (D) and 4 (E) weeks of exposure; diffuse B-cell infiltration after 2 weeks of TSPH (G) and TSPTC (H) implant exposure; appearance of macrophages in peri-implant areas of TSP (J) and TSPT (K) implant surfaces; M2-polarized macrophage occurrence around TSPH implants after 4 (M) and 8 (N) weeks of exposure. Histological keys: Impl – implant interface; * – coating particles; + – new bone formation; arrows – foreign body giant cells; arrowheads – lymphocytes. Statistical analysis: Box-and-whisker plots displaying the median (center line), 25th–75th percentiles (box), and min/max (whiskers). Significance markers: † – p<0.05, †† – p<0.001, ††† – p<0.0001 vs. uncoated Ti; # – p<0.05, ## – p<0.001 vs. TSPH (HAp); * – p<0.05, ** – p<0.001, *** – p<0.0001 vs. sham control. Brackets indicate significant differences between the experimental groups.

particles and in the necrotic zones.

Quantitative analysis of immune cell infiltration. At week 1, pan-MPH density (CD68-positivity) was uniformly high across all experimental groups (48.2 to 54.8 cells/mm², Fig. 3 L), indicating a generalized inflammatory response, irrespective of surface modification. No statistically significant intergroup differences were observed ($p>0.05$). By week 8, the TSPTC group exhibited a mean density of 17.6±1.1 cells/mm², which was significantly higher than that of the rough Ti group (TS, $p<0.05$) and TSPH group (10.0±1.6 cells/mm²; $p<0.05$).

The density of M2-polarized MPH at week 2 was 5.6±2.3 cells/mm² in the sham group, whereas that in the titanium-based implant groups ranged from 0.8-2.0 cells/mm² (Fig. 3 O). At week 4, the TSPH group exhibited a marked increase in $CD163^+$ cells (9.6±2.9 cells/mm²), significantly exceeding that of the TS group (2.6±0.9 cells/mm²; $p<0.05$). At week 8, the TSPH group maintained a density of 4.0±1.6 cells/mm², which remained significantly higher than that of the sham group ($p<0.05$).

T-cell infiltration at week 1 reached 25.4±5.6 cells/mm² in the TSPT group (Fig. 3 C). Concurrently, activated T-cells expressing the IL-2 receptor in the same group reached 16.6±2.3 cells/mm² (Fig. 3 F). At week 2, the $CD25^+$ cell density in the TSPT group remained elevated (13.2±1.6 cells/mm²). In contrast, the TSPH group exhibited a significantly lower $CD25^+$ cell occurrence at week 2 (5.4±1.1 cells/mm²; $p<0.05$). By week 8, $CD3^+$ cell infiltration in the TSPH group declined to 1.6±1.1 cells/mm², whereas the TS group retained higher values (5.2±0.8 cells/mm²). $CD25^+$ expression in the TSPTC group at week 8 (4.2±1.3 cells/mm²) was significantly higher than that in the TSPH group (0.4±0.5 cells/mm²; $p<0.05$).

CD45R-positive cells peaked at week 2 in the titanium-based groups, ranging from 40.0 to 42.6 cells/mm² (Fig. 3 I), significantly exceeding the sham values ($p<0.01$). At week 4, the TSPTC group demonstrated the highest $CD45R^+$ cell density (46.2±9.6 cells/mm²), which was significantly greater than that of the TSPH group (16.0±3.4 cells/mm²; $p<0.05$). By week 8, $CD45R^+$ cell occurrence declined in the TSPH group (10.4±1.1 cells/mm²), whereas the TSPT and TSPTC groups maintained higher numbers (21.6±2.3 and 24.2±3.1 cells/mm², respectively). The difference between the TSPH and TSPTC groups at week 8 remained significant ($p<0.05$).

Correlative analysis of surface drivers and cellular crosstalk. To elucidate the underlying drivers of the observed cellular responses and their interdependencies, we conducted correlative analyses relating surface characteristics to immune cell infiltration and explored the cellular crosstalk. Spearman's rank correlation analysis revealed no statistically significant associations between surface roughness (R_a) and immune cell density for any marker within the titanium-based groups at any time point ($p>0.05$).

In contrast, correlation analysis using the assigned bioactivity rank demonstrated significant negative correlations with adaptive immune cell populations. T-cells density showed moderate negative correlations with bioactivity rank at weeks 2 ($r=-0.46$; $p<0.05$), 4 ($r=-0.34$; $p<0.05$), and 8 ($r=-0.48$; $p<0.05$). Similarly, CD25 expression negatively correlated with increasing bioactivity rank at weeks 2 ($r=-0.59$; $p<0.05$), 4 ($r=-0.51$, $p<0.05$), and 8 ($r=-0.54$, $p<0.01$).

$CD45R^+$ cell density was negatively correlated with bioactivity rank at weeks 2 ($r=-0.66$; $p<0.0001$) and 8 ($r=-0.35$; $p<0.05$). Among innate immune markers, pan- MPH density demonstrated a weak negative correlation with the bioactivity rank at week 4 only ($r=-0.33$; $p<0.05$), whereas CD163 expression showed no significant correlation with the bioactivity rank at any time point.

Correlation matrix analysis based on the implant bioactivity rank demonstrated significant associations within the adaptive immune compartment. T-cell density correlated positively with $CD25^+$ activation status at weeks 2 ($r=0.47$; $p<0.05$), 4 ($r=0.90$; $p<0.0001$), and 8 ($r=0.77$; $p<0.01$). The $CD3^+$ and $CD45R^+$ populations were positively correlated at weeks 2 ($r=0.39$; $p<0.05$) and 8 ($r=0.36$; $p<0.05$). $CD45R^+$cell density correlated positively with MΦ occurrence at week 4 ($r=0.44$; $p<0.05$) and week 8 ($r=0.37$; $p<0.05$). No significant correlations were identified between M2-MΦs and the total number of MΦs or M2 and adaptive immune populations at any time point ($p>0.05$).

Discussion

Our study provides in vivo evidence demonstrating that the osseointegration of functional implant coatings is affected by complex osteoimmunological interactions, extending beyond the traditional macrophage-centric paradigm [24]. A notable finding was the demonstration of relative independence of inflammatory manifestations from surface topography: while Ti surfaces induced sustained activation of the adaptive immune system, the bioactive HAp ceramics actively suppressed this response, promoting immune quiescence and a marked shift towards a reparative M2 macrophage phenotype. Additionally, a distinct B-lymphocyte response was identified in association with coating instability, establishing a direct cellular link between mechanical failure, particle release, and immunogenic failure of implants. Furthermore, the pivotal role of macrophage polarization in facilitating reparative outcomes has been well documented.

Historically, titanium has been considered biologically inert, and biocompatibility studies have largely focused on the innate foreign body reaction [24]. However, our results align with emerging evidence from Harloff T. et al. [7] and others, challenging this view by demonstrating that titanium implants trigger a specific T cell-mediated response. We observed that all titanium-based groups, regardless of roughness, maintained elevated levels of activated T-cells ($CD3^+/CD25^+$) well into the chronic phase (week 8). This persistence can be attributed to the upregulation of the high-affinity IL-2 receptor α-chain (CD25). Once expressed, CD25 establishes a potent autocrine feedback loop, allowing T-cells to proliferate in response to their own cytokines and sustain the inflammatory response indefinitely [1]. Such persistent activation parallels

the significant fibrous encapsulation observed around Ti, TS, and TSP implants from the second week onwards, confirming a state of sustained chronic inflammation. This inflammatory response is driven by the release of titanium nano- and microparticles, TiO_2, and Ti^{2+} ions, which may trigger distinct immune mechanisms [18]. Specifically, persistent T-cell activation likely stems from the upstream activation of Toll-like receptors (TLRs) and the intracellular NFAT signaling pathways. As detailed by Shirazi S. et al., oxide surfaces trigger NF-κB [21], while concurrent calcium signaling activates NFAT, a transcription factor essential for CD25 gene expression [1].

Supporting this, we found a strong negative correlation between bioactivity rank and T-cell density, confirming our hypothesis that functional coatings act as immunological buffers. A bioactive HAp layer masks the underlying titanium substrate, effectively attenuating immune recognition and preventing the initial activation cascade of the TLRs and NF-κB pathways, as well as inhibiting the calcium-calcineurin-NFAT axis downstream. This suppression of early signaling inhibits the downstream activation of T-cells, thereby preventing the chronic inflammatory signaling cascade that could lead to aseptic loosening [2, 12, 29].

A key unexpected finding was the distinct immunogenic profile of the hybrid ("sandwich") titanium-alumina coating (TSPTC group). While Al_2O_3 is chemically inert and generally biocompatible [15], the mechanical instability of the hybrid coating led to the release of detached particles, as observed histologically at week 4 post-implantation. This event coincided with a notable increase in B-cell infiltration, which was not observed around the stable HAp or pure alumina coatings (TSPH and TSPC groups). This observation provides a cellular mechanism for the inflammation described by Kheder W. et al. [11] regarding the Ti particles. This suggests that the release of coating debris transitions the immune response from a generic foreign body reaction to a specific humoral attack, potentially involving antibody-mediated cytotoxicity and osteolysis [6, 28]. While B-lymphopoiesis is a normal feature of the regenerating bone marrow around the implant material, described as "myelointegration" [21], the dense B-cell clusters observed around the unstable coating groups within the fibrous layer were not homeostatic. Instead, they correlated strictly with detached coating particles, suggesting a shift from physiological myelointegration to pathological humoral response. This underscores a critical implant design principle: the immunomodulatory benefit of coating diminishes if mechanical stability is compromised, as detached coating particles trigger not only giant cell reactions but consequently potent specific immune response.

Bone healing acceleration relies on shifting the immune balance from adaptive immune activation to reparative M2 macrophage polarization. In this context, Shirazi et al. stated that nanotopography can act as a potent 'ally' in immunomodulation [21]; however, our results challenge this view. Consistent with established models, surface topography alone is insufficient to drive regeneration [6, 9, 23, 26] or to override the chronic adaptive immune response to titanium. Indeed, until the eighth week of implant exposure, titanium surfaces regardless the surface topography (Ti, TS, TSP, and TSPT), as well as alumina-based coatings, to a lesser extent, retained M2 polarization in a low level. This corresponds to the fibrosis development observed around these coatings at weeks 2-4 [4]. In contrast, the HAp coating induced a statistically significant increase in the number of M2-MPH at 4 weeks. These data suggest that surface chemistry should be prioritized over topography to ensure long-term immune quiescence. This increase in M2-MPH is functionally linked to the superior bone formation previously reported in this model [4], as M2-MΦs are established sources of osteogenic factors [20, 21]. The findings suggest that the osteoconductivity of hydroxyapatite (HAp) is not solely attributable to its intrinsic material properties but is also influenced by the downstream effects of its immunomodulatory capacity. By promoting a shift in the inflammatory environment towards an M2-polarization, the bioactive surface enhances the secretion of essential osteogenic cytokines, such as BMP-2 and VEGF, which are critical signals for the neoangiogenesis, recruitment and differentiation of mesenchymal stem cells into functional osteoblasts [14]. The absence of a correlation between total macrophage infiltration and M2 occurrence further underscores that biocompatibility is not characterized by the absence of MPH but by the effective modulation of their phenotype through surface chemistry. Additionally, the strong negative correlation observed between the coating bioactivity rank and adaptive immune activation reflects the fundamental differences in the surface physicochemical properties of the materials under investigation [8]. Unlike the passivated and electrically inert surfaces of titanium and alumina, which support only non-specific adsorption, hydroxyapatite exhibits dynamic ion-exchange capabilities and heterogeneous electrostatic domains that mimic native bone minerals [8].

The present study employed a rat femoral model, which, despite its established utility for osseointegration research, exhibits metabolic and immunological differences from human clinical conditions [22]. The observation period was confined to 8 weeks, which, while sufficient to capture the critical transition from acute to chronic inflammation, necessitates longer-term studies (ranging from 6 months to 1 year) to assess the durability of the benefits conferred by hydroxyapatite (HAp) coatings [13]. Furthermore, although immunohistochemistry offers precise spatial localization, it remains less comprehensive in terms of quantitative analysis compared to flow cytometry. Future investigations employing multiplex arrays could provide further insights into the specific cytokine profiles (e.g., IL-4, IL-10 versus TNF-α) that drive the cellular changes observed in this study.

Conclusions

1. Histological evaluation of the local bone tissue response to the investigated materials indicated that titanium implants with untreated surface were not immunologically

inert, as they elicited a persistent T-cell-mediated response and moderate inflammation, consistent with fibrous encapsulation. In contrast, bioactive hydroxyapatite coatings facilitated the downregulation of the inflammatory response and promoted early osteoinduction within four weeks.

2. The osteoconductivity of functional protective coatings depends on their ability to modulate the local inflammatory milieu. By actively suppressing adaptive immune activation and promoting M2-macrophage polarization, these coatings establish a specific pro-reparative microenvironment, which is essential for effective osteoconduction and osseointegration.

3. The mechanical instability of functional protective coatings induces a distinct immunogenic failure mode characterized by enhanced B-cell infiltration in response to coating debris, thereby negating the benefits of surface chemistry.

4. Optimizing implant surfaces necessitates a transition from purely topographic manipulation to "osteoimmunological" surface engineering, wherein stable bioactive chemistry is employed to modulate the crosstalk between innate and adaptive immunity.

References

[1] Abbas, A. K., Lichtman, A. H., & Pillai, S. (2020). *Basic immunology: Functions and disorders of the immune system* (6th ed., pp. 108-185). Elsevier.

[2] Anderson, J. M., Rodriguez, A., & Chang, D. T. (2008). Foreign body reaction to biomaterials. *Seminars in Immunology*, *20*(2), 86-100. doi: 10.1016/j.smim.2007.11.004

[3] Avery, D., Morandini, L., Sheakley, L., Grabiec, M., & Olivares-Navarrete, R. (2024). CD4+ and CD8+ T cells reduce inflammation and promote bone healing in response to titanium implants. *Acta Biomaterialia*, *179*, 385-397. doi: 10.1016/j.actbio.2024.03.022

[4] Bondarenko, O. O., Bozhko, A. H., Skoryk, M. A., Bondarenko, N. S., Shponka, I. S., & Loskutov, O. Y. (2024). Peri-implant osteogenesis on alumina-coated titanium implants in rat femur: Morphological and elemental analysis of implant surfaces. *Pathologia*, *21*(2), 132-140. doi: 10.14739/2310-1237.2024.2.306822

[5] Evans, J. T., Evans, J. P., Walker, R. W., Blom, A. W., Whitehouse, M. R., & Sayers, A. (2019). How long does a hip replacement last? A systematic review and meta-analysis of case series and national registry reports with more than 15 years of follow-up. *The Lancet*, *393*(10172), 647-654. doi: 10.1016/S0140-6736(18)31665-9

[6] Furlanetto, M., Castro, R., Silva, F., Pereira, J., Macedo, J., & Soares, S. (2025). Titanium particle impact on immune cells, cytokines, and inflammasomes: Helping to profile peri-implantitis–A systematic review. *Oral*, *5*(4), 80. doi: 10.3390/oral5040080

[7] Harloff, T., Hönle, W., Holzwarth, U., Bader, R., Thomas, P., & Schuh, A. (2010) Titanium allergy or not? "Impurity" of titanium implant materials. *Health*, *2*, 306-310. doi: 10.4236/health.2010.24045

[8] Hench, L. L. (1991). Bioceramics: From concept to clinic. *Journal of the American Ceramic Society*, *74*(7), 1487-1510. doi: 10.1111/j.1151-2916.1991.tb07132.x

[9] Hotchkiss, K. M., Reddy, G. B., Hyzy, S. L., Schwartz, Z., Boyan, B. D., & Olivares-Navarrete, R. (2016). Titanium surface characteristics, including topography and wettability, alter macrophage activation. *Acta Biomaterialia*, *31*, 425-434. doi: 10.1016/j.actbio.2015.12.003

[10] International Organization for Standardization. (2016). *Biological evaluation of medical devices – Part 6: Tests for local effects after implantation* (ISO 10993-6:2016). https://www.iso.org/standard/61089.html

[11] Kheder, W., Bouzid, A., Venkatachalam, T., Talaat, I. M., Elemam, N. M., Raju, T. K., … & Almas, K. (2023). Titanium particles modulate lymphocyte and macrophage polarization in peri-implant gingival tissues. *International Journal of Molecular Sciences*, *24*(14), 11644. doi: 10.3390/ijms241411644

[12] Landgraeber, S., Jäger, M., Jacobs, J. J., & Hallab, N. J. (2014). The pathology of orthopedic implant failure is mediated by innate immune system cytokines. *Mediators of inflammation*, *2014*, 185150. doi: 10.1155/2014/185150

[13] Laubach, M., Whyte, S., Chan, H. F., Frankenbach-Désor, T., Mayer-Wagner, S., Hildebrand, F., … & Hutmacher, D. W. (2024). Lost in translation: the lack of agreement between surgeons and scientists regarding biomaterials research and innovation for treating bone defects. *BMC medicine*, *22*(1), 517. doi: 10.1186/s12916-024-03734-z

[14] Liu, W., Liang, L., Liu, B., Zhao, D., Tian, Y., Huang, Q., & Wu, H. (2021). The response of macrophages and their osteogenic potential modulated by micro/nano-structured Ti surfaces. *Colloids and surfaces. B, Biointerfaces*, *205*, 111848. doi: 10.1016/j.colsurfb.2021.111848

[15] Matijosius, T., Bakute, N., Padgurskas, J., Kreivaitis, R., & Žunda, A. (2025). Corrosion and biocompatibility studies of bioceramic alumina coatings on aluminum alloy 6082. *ACS Applied Materials & Interfaces*, *17*(17), 24901–24917. doi: 10.1021/acsami.5c00532

[16] Moon, H. J., Gulati, K., Li, T., Moran, C. S., & Ivanovski, S. (2024). Inflammatory or reparative? Tuning macrophage polarization using anodized anisotropic nanoporous titanium implant surfaces. *Small Science*, *4*(10), 2400211. doi: 10.1002/smsc.202400211

[17] Niinomi, M., & Nakai, M. (2011). Titanium-based biomaterials for preventing stress shielding between implant devices and bone. *International Journal of Biomaterials*, *2011*, 836587. doi: 10.1155/2011/836587

[18] Pettersson, M., Almlin, S., Romanos, G. E., & Johansson, A. (2022). Ti Ions Induce IL-1β Release by Activation of the NLRP3 Inflammasome in a Human Macrophage Cell Line. *Inflammation*, *45*(5), 2027-2037. doi: 10.1007/s10753-022-01672-7

[19] Sanderson, T., Wild, G., Cull, A. M., Marston, J., & Zardin, G. (2019). Immunohistochemical and immunofluorescent techniques. In S. K. Suvarna, C. Layton, & J. D. Bancroft (Eds.), *Bancroft's theory and practice of histological techniques* (8th ed., pp. 337-394). Elsevier. doi: 10.1016/B978-0-7020-6864-5.00019-0

[20] Schlundt, C., Fischer, H., Bucher, C. H., Rendenbach, C., Duda, G. N., & Schmidt-Bleek, K. (2021). The multifaceted roles of macrophages in bone regeneration: A story of polarization, activation and time. *Acta biomaterialia*, *133*, 46-57. doi: 10.1016/j.actbio.2021.04.052

[21] Shirazi, S., Ravindran, S., & Cooper, L. F. (2022). Topography-mediated immunomodulation in osseointegration; Ally or Enemy. *Biomaterials*, *291*, 121903. doi: 10.1016/j.biomaterials.2022.121903

[22] Stein, M., Elefteriou, F., Busse, B., Fiedler, I. A., Kwon, R. Y., Farrell, E., … & Tuckermann, J. (2023). Why Animal Experiments Are Still Indispensable in Bone Research: A

Statement by the European Calcified Tissue Society. *Journal of bone and mineral research: the official journal of the American Society for Bone and Mineral Research*, *38*(8), 1045-1061. doi: 10.1002/jbmr.4868

[23] Tang, J., Tang, R., Chen, L., Shao, C., & Yi, L. (2025). Osteoimmunomodulatory effects of biomimetic porous carboxymethyl chitosan/alginate/hydroxyapatite composite hydrogel scaffolds. *International Journal of Biological Macromolecules*, *334* (Pt 1), 148694. doi: 10.1016/j.ijbiomac.2025.148694

[24] Trindade, R., Albrektsson, T., Tengvall, P., & Wennerberg, A. (2016). Foreign body reaction to biomaterials: On mechanisms for buildup and breakdown of osseointegration. *Clinical Implant Dentistry and Related Research*, *18*(1), 192-203. doi: 10.1111/cid.12274

[25] U.S. Food and Drug Administration. (2023). *Use of International Standard ISO 10993-1, "Biological evaluation of medical devices - Part 1: Evaluation and testing within a risk management process": Guidance for industry and Food and Drug Administration staff*. https://www.fda.gov/media/142959/download

[26] Vishwakarma, A., Bhise, N. S., Evangelista, M. B., Rouwkema, J., Dirks, M. R., Ciardelli, G., … & Ghaemmaghami, A. M. (2016). Engineering immunomodulatory biomaterials to tune the inflammatory response. *Trends in Biotechnology*, *34*(6), 470-482. doi: 10.1016/j.tibtech.2016.03.009

[27] Wang, H., Li, Y., Li, H., Yan, X., Jiang, Z., Feng, L., … & Li, G. (2025). T cell related osteoimmunology in fracture healing: Potential targets for augmenting bone regeneration. *Journal of orthopaedic translation*, *51*, 82-93. doi: 10.1016/j.jot.2024.12.004

[28] Wang, L. T., Juang, S. E., Lan, C. L., Huang, Y. H., & Chen, Y. W. (2025). Titanium implants trigger extra-periodontal T cell-mediated immunity. *Biomaterials Science*, *13*(6), 1543-1553. doi: 10.1039/d4bm00246f

[29] Yun, J. I., Yun, S. I., Kim, J. H., Kim, D. G., & Lee, D. W. (2025). Mediation of osseointegration, osteoimmunology, and osteoimmunologic integration by Tregs and macrophages: A narrative review. *International Journal of Molecular Sciences*, *26*(11), 5421. doi: 10.3390/ijms26115421

[30] Zangani, A., Faccioni, P., Pardo, A., Tomizioli, N., Zambotti, T., Beccherle, M., … & Zerman, N. (2024). Peri-implantitis: A comprehensive review of recent findings. *Journal of Applied Cosmetology*, *42*(2), 102-116. doi: 10.56609/jac.v42i2.396

ОСТЕОІМУНОМОДУЛЯЦІЯ ЗА ДОПОМОГОЮ ФУНКЦІОНАЛЬНО-ЗАХИСНИХ ПОКРИТТІВ: НАЛАШТУВАННЯ ВРОДЖЕНОГО ТА АДАПТИВНОГО ІМУНІТЕТУ ПРИ ОСТЕОІНТЕГРАЦІЇ ТИТАНОВИХ ІМПЛАНТАТІВ

Бондаренко О. О., Ролдугіна М. О., Бондаренко Н. С., Мальцев І. О., Лоскутов О. Є., Шпонька І. С.

Довгострокова клінічна надійність внутрішньокісткових імплантатів часто порушується асептичним розхитуванням, типом неспроможності імплантату, що викликаний хронічним запаленням і фіброзною інкапсуляцією. Сучасні дані свідчать, що остеоінтеграція ґрунтується на складних остеоімунологічних взаємодіях, а не лише на механічній фіксації. Метою цього дослідження було вивчення імуномодулюючих ефектів функціонально-захисних покриттів, зокрема біоактивного гідроксиапатиту (HAp) та біоінертного оксиду алюмінію (корунд, Al2O3), на взаємодію між вродженою та набутою імунною відповіддю. Використовувалася модель стегнової кістки щура (n=160) із сімома різними варіантами поверхонь імплантату, які відрізнялись шорсткістю (Ra 1,89-23,7 мкм) та хімічним складом. Збір періімплантної кісткової тканини проводили на 1, 2, 4 та 8 тижнях для відстеження переходу від гострої до хронічної стадії запалення. Методика включала комплексний імуногістохімічний (ІГХ) аналіз із використанням наступних маркерів: CD3 для Т-клітин, CD25 (рецептор інтерлейкіну-2) для активованих лімфоцитів, CD45R для В-клітин, CD68 для макрофагів загалом та CD163 для репаративного фенотипу М2 макрофагів. Статистична оцінка виконувалася з використанням непараметричного методу Крускала-Волліса з пост-хок корекцією Данна та рангової кореляції Спірмена для визначення співвідношення впливів топографії та хімічного складу. Періімплантне середовище титанових контрольних груп характеризувалося стійким Т-клітинозалежним запаленням; незалежно від шорсткості поверхні ці імплантати демонстрували підвищену щільність активованих Т-клітин (CD3+/CD25+), що зберігалася до восьмого тижня, підтверджуючи розвиток хронічного запалення. Встановлені біоактивні покриття HAp суттєво пригнічували активацію набутої імунної відповіді, сприяючи вираженому фенотиповому зсуву у бік репаративних М2 макрофагів (CD163+) і стимулюючи раннє формування грубоволокнистої кістки вже на четвертому тижні. У групі з гібридним покриттям оксид алюмінію-титан (TSPTC) спостерігався окремий імуногенний тип відмови: механічна нестабільність призводила до відшарування частинок покриття, що ініціювало інфільтрацію В-клітин (CD45R+), характерну для патологічної гуморальної реакції, а не фізіологічної мієлоінтеграції. Кореляційний аналіз не показав суттєвого зв'язку між шорсткістю поверхні та інфільтрацією імунними клітинами, тоді як зростання біоактивності мало негативний кореляційний зв'язок із щільністю клітин набутої імунної відповіді, підкреслюючи провідну роль хімічних властивостей поверхні порівняно з топографією у пригніченні запалення. Дані, що характеризуються закономірностями імунної міжклітинної взаємодії, показали позитивний зв'язок між щільністю Т-клітин та маркерами активації, у той час як шар HAp діяв як імунний буфер, ефективно маскуючи титановий для запобігання аутокринному посиленню запалення. Наше дослідження підкреслює, що стабільні функціонально-захисні покриття є критично важливими для налаштування періімплантатного імунного середовища, зокрема шляхом пригнічення хронічних сигналів набутої імунної відповіді та посилення поляризації М2 макрофагів, що створює про-репаративне мікросередовище, необхідне для довгострокової остеоінтеграції.

Ключові слова: *остеоімунологія, остеоінтеграція, функціонально-захисні покриття, титанові імплантати, поляризація макрофагів, рецептор інтерлейкіну-2.*

Author's contribution

Bondarenko O. O. – conceptualization, methodology, research, formal analysis, visualization, validation, writing of the original draft.
Rolduhina M. O. – data collection, writing of the original draft.
Bondarenko N. S. – conceptualization, formal analysis, validation, data visualization.
Maltsev I. O. – data analysis and interpretation, critical revision of the article.
Loskutov O. Y. – validation, project administration, supervision, data curation, supervision.
Shpon'ka I. S. – validation, project administration, supervision, resources, data curation, writing – review & editing.

DOI: 10.31393/morphology-journal-2026-33(1)-07 Reports of Morphology, Vol. 32, №1, Pages 47-54

ISSN 1818-1295 eISSN 2616-6194

REPORTS OF MORPHOLOGY

Official Journal of the Scientific Society of Anatomists, Histologists, Embryologists and Topographic Anatomists of Ukraine

journal homepage: https://morphology-journal.com

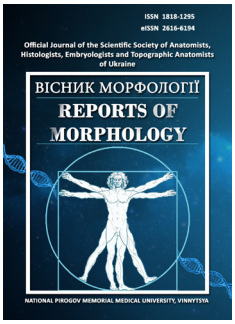

Changes in the density of soft tissues of the abdominal cavity organs and abdominal wall depending on body weight according to computed tomography data

Malyshevskyj I. O.[1], Khimich S. D.[2], Ivashchuk O. I.[3], Olkhomiak O. O.[2]

[1] Bukovina Clinical Oncology Center, Chernivtsi, Ukraine

[2] National Pirogov Memorial Medical University, Vinnytsya, Ukraine

[3] Bukovina State Medical University, Chernivtsi, Ukraine

ARTICLE INFO

Received: 10 July 2025

Accepted: 12 January 2026

UDC: 617.55:616-073.756.8

CORRESPONDING AUTHOR

e-mail: s-khimich@ukr.net

Khimich S. D

CONFLICT OF INTEREST

The authors have no conflicts of interest to declare.

FUNDING

Not applicable.

DATA SHARING

Data are available upon reasonable request to corresponding author.

Obesity is a common phenomenon and disease that requires continuous development of the assessment of morpho-functional data of obese people, including soft tissues. The aim of the study was to use computerized tomography data to determine the density of skin, subcutaneous tissue, and intra-abdominal adipose tissue in people with different body weights. Computerized tomography (CT) scans and tissue density analysis were evaluated in Housfield units (HU). To standardize the calculations, we selected CT scans performed at the level of the xiphoid process, the lower edge of the 12th rib, the navel, the upper point of the ilium, and at the level of the spina iliaca anterior superior in people with normal body weight (body mass index (BMI) 18.5-24.9), with excess body weight (BMI 25.0-29.9), grade I obesity (BMI 30.0-34.9), and grade II obesity (BMI 35.0-39.9). It has been determined that with an increase in body weight and degree of obesity, not only an increase in the thickness of subcutaneous adipose tissue and intraperitoneal fat is clearly visible in all "sections," but also a statistically significant decrease in skin density. If we take the average density of subcutaneous adipose tissue (-63.38 HU units) as a unit, the density of adipose tissue in people who are overweight decreases by 1.19 times, in people with grade I obesity – by 1.43 times, and in people with grade II obesity – by 1.62 times. Changes in the density of intraperitoneal fat are even more noticeable. Taking the density of intraperitoneal fat (-59.56 HU units) as a unit, the density of fiber in people with excess weight decreases by 1.24 times, in people with grade I obesity – by 1.46 times, and in people with grade II obesity – by 1.85 times ($p \leq 0.05$ between the indicators of people with normal weight and obesity). Therefore, with an increase in body weight, the density of skin, subcutaneous adipose tissue, and intraperitoneal fat in Housefield units decreases, and this difference is particularly significant between people with normal body weight and those with grade II obesity. Since the density of soft tissues decreases significantly with increasing body weight, the risk of iatrogenic (surgical) damage increases, as their resistance to mechanical damage decreases.

Keywords: *soft tissues, adipose tissue, skin, intraperitoneal fat, subcutaneous adipose tissue, obesity, computed tomography, diagnosis, tissue density, Housfield units.*

Introduction

According to WHO criteria, obesity is defined as a body mass index (BMI) of 30 kg/m² or higher, and is further classified as class 1 (30.0-34.9 kg/m²), class 2 (35.0-39.9 kg/m²), and class 3 (≥40.0 kg/m²) [29]. Obesity has become one of the most pressing global public health issues of the 21st century. Obesity has reached epidemic proportions worldwide: in 2022, more than 1 billion people were classified as obese, representing 13 % of the world's population [1]. Such dramatic trends have prompted experts to characterize obesity as a global epidemic, or even a "pandemic" in terms of its scale [12]. At the same time, according to some estimates, by 2030, more people will be overweight or obese than not [15]. It is also noteworthy that obese people are much more likely to develop type 2 diabetes, hypertension, and dyslipidemia – conditions

that together contribute to metabolic syndrome and lead to cardiovascular complications [23]. Patients with obesity have an increased incidence of surgical complications, mortality, wound infection, and wound drainage. In other words, there is strong evidence that there is a link between obesity and poor surgical outcomes. This is especially true for wound healing [20]. It is clear that the increase in the number of obese patients requires more frequent medical care and appropriate imaging [4]. And although obese patients face unique challenges in medical imaging and during surgical procedures, in recent years, medical equipment manufacturers, radiologists, and radiologists have recognized this problem and developed innovative methods to solve it. This is certainly a positive development. At the same time, the approaches to assessing tissue and organ density in obese people and people of normal weight, which is done in Housfield units [13], are practically the same. However, CT-based body composition analysis is increasingly becoming part of clinical practice [9], meaning it's a clinically necessary test.

Computed tomography (CT) and magnetic resonance imaging (MRI) are cross-sectional, non-invasive methods used to measure fat distribution in the abdominal cavity (visceral fat and subcutaneous fat components) and its correlation with various diseases and laboratory parameters [17]. By measuring body composition, such as the amount and location of fat, as well as the amount and quality of muscle, clinicians can obtain valuable information about the patient's physiological status [5].

The radio density of adipose tissue can be objectively measured using CT in Hounsfield units (HU) [8]. The mean CT-derived fat tissue radio density has been introduced as an indirect surrogate marker of fat tissue quality [14]; several potential factors have also been introduced, such as blood flow [12], adipocyte size [28], and lipid content [2]. Increased radio density of subcutaneous adipose tissue may indicate adipose tissue fibrosis [24].

In our opinion, the assessment of soft tissue density based on CT data is not only morphofunctionally significant, but may also be important in predicting the development and course of various inflammatory processes. The density of adipose tissue is particularly important in surgical interventions. It seems logical that as tissue density decreases, its resistance to damage decreases and, thus, the risk of trauma increases, which, in turn, leads to an increase in the frequency of surgical complications.

The goal is to use computed tomography to determine the density of the skin, subcutaneous tissue, and intra-abdominal adipose tissue in people of different body weights.

Materials and methods

Analysis of CT scans performed at the Bukovina Clinical Oncology Center (Chernivtsi), the "Oktet" computer tomography office (Chernivtsi), the commercial non-profit enterprise "Sokyrianska Hospital" (Sokyriany), the communal institution "Vyzhnytska Central District Hospital" (Vyzhnytsia), and the "St. Luke Clinic" (Chernivtsi) on Optima CT 540, Somaton go. Up, Brilliance 64, and Aquilion Lightning during 2024-2025, was performed using the Micro Dicom computer program, 2025 (DICOM Viever 2025.1 (64 bit) Bild 3321, unlicensed for commercial use) on an Intel CORE I3 9th Gen computer device. The CT scans presented were performed on the recommendation of doctors for medical reasons to establish or verify various diagnoses. Patients did not receive any additional radiological exposure. Patients were informed that the results of their studies could be used for scientific research, for which informed consent was obtained (protocol No. 1, dated 28.11.2025, of the ethical review by the Expert Commission of the Bukovina Clinical Oncology Center of the Ministry of Health of Ukraine on the absence of violations of ethical standards and generally accepted legislative acts).

Tissue density analysis was performed using the above-mentioned Hounsfield units (HU) [13]. Housfield units (HU) are a dimensionless unit that is universally used in computed tomography to express CT numbers in a standardized and convenient form. Housfield units are obtained by linear transformation of the measured attenuation coefficients. This conversion is based on arbitrarily defined radio densities of air and pure water:

• the radio density of distilled water at standard temperature and pressure (STP) is 0 HU;

• the radio density of air at normal temperature is 1000 HU.

There are no equivalents to Hounsfield units in any other form of structural imaging.

Typical values:

• air: -1000 HU;
• bone (cortical): >1000 HU;
• bone (trabecular): 300 to 800 HU;
• brain (gray matter): 40 HU[11];
• brain (white matter): 30 HU[11];
• subcutaneous fat: from -100 to -115 HU[10];
• liver: 45-50 HU[10];
• lungs: from -950 to -650 HU[12];
• metal: >3000 HU;
• muscles: from 45 to 50 HU[10];
• kidney cortex: from 25 to 30 HU[10];
• spleen: from 40 to 45 HU[10];
• water: 0 HU (by definition).

To standardize the calculations, we selected CT scans performed at the level of the xiphoid process, the lower edge of the 12th rib, the navel, the upper point of the ilium, and at the level of the spina iliaca anterior superior in people with normal body weight (BMI 18.5-24.9), with excess body weight (BMI 25.0-29.9), grade I obesity (class I) (BMI 30.0-34.9), and grade II obesity (class II) (BMI 35.0-39.9).

If the "skeletotopic points" of the sections are clear, then the sections at the level of the navel were chosen because of the possibility of reproducing measurements between observers (researchers) using CT scanning of a single section passing through the navel (which is easily detectable) and can be used in oncology as a prognostic tool for measuring the characteristics of the host organism [25]. Moreover, some

authors believe that computed tomography of the abdominal cavity at the level of the navel is the most accurate diagnostic method for assessing abdominal adipose tissue [23].

By moving the cursor, measurements of subcutaneous fat thickness were taken and 36 determinations of HU units of skin, subcutaneous fat, and fat deposits in the abdominal cavity were made on each of the five “slices”. The data were entered into tables for statistical and mathematical processing and graphing. For illustration, we present CT “slices” of patients with normal body weight, overweight, and obesity of I and II degrees at the navel level (Figs. 1-4).

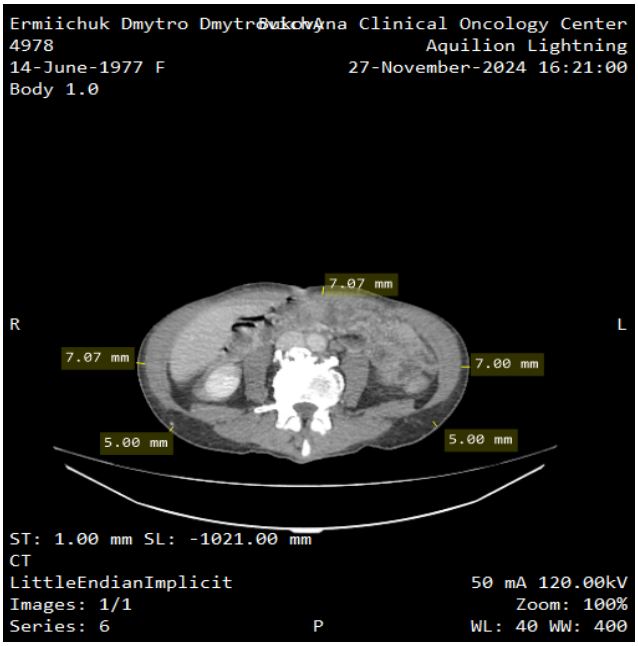

Fig. 1. CT scan of patient E., 47 years old with normal body weight, performed at the level of the navel. The thickness of the subcutaneous fat tissue is from 5.0 to 7.07 mm.

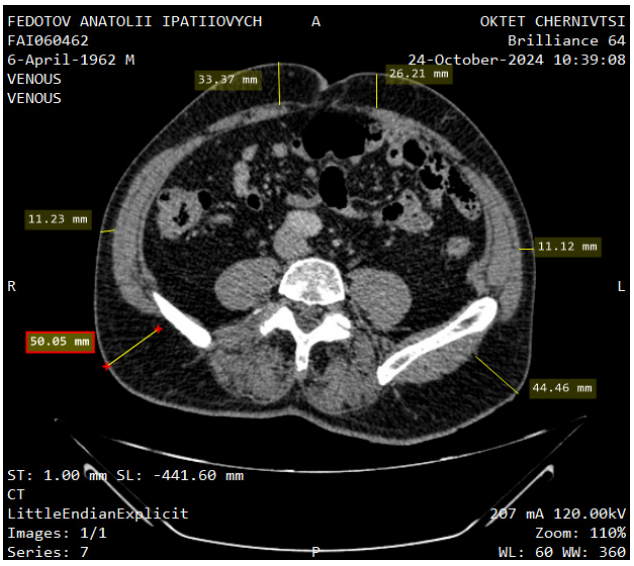

Fig. 2. CT scan of patient F., 62 years old with excess body weight, performed at the navel level. Subcutaneous fat thickness from 11.12 to 50.05 mm.

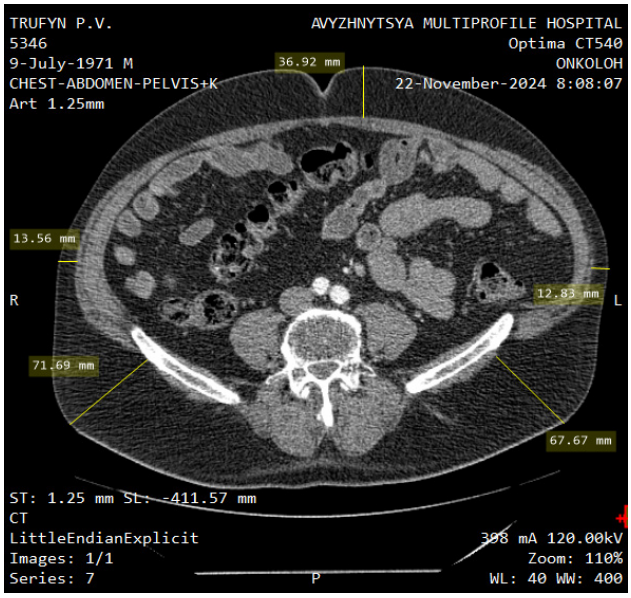

Fig. 3. CT scan of patient T., 53 years old with grade I obesity, performed at the navel level. The thickness of the subcutaneous fat tissue ranges from 12.83 to 71.69 mm.

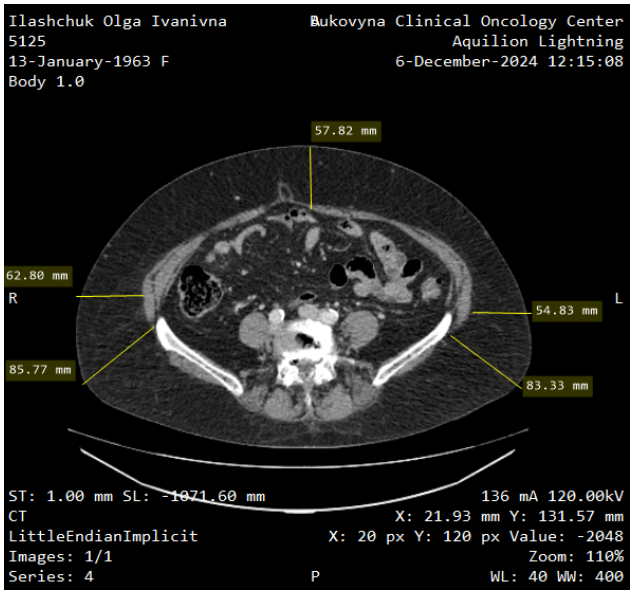

Fig. 4. CT scan of patient I., 62 years old with grade II obesity, performed at the navel level. The thickness of the subcutaneous fat tissue ranges from 54.83 to 85.77 mm.

Statistical processing of the obtained results was performed using packages of applied computer programs for variational-statistical analysis of medical and biological examination data and was carried out using the spreadsheet processor “Office Excel 2013” (product number 00216-40000-00000-AA905) and the Statistica 6 software package.

Results

The results of Housfield unit measurements in patients with normal body weight, overweight, grade I obesity, and grade II obesity are presented in Tables 1-4.

Table 1. Average Housefield unit (HU) measurements in patients with normal body weight (n=36).

Level	Skin	Subcutaneous tissue	Internal fat	Subcutaneous tissue thickness (mm)
Sword-shaped process	34.43±8.21	-54.70±11.87	-61.90±10.54	4.000-5.830
Lower edge of the 12th rib	27.54±7.01	-69.90±12.32	-48.44±6.56	4.240-5.110
Navel level	43.05±9.33	-62.80±10.76	-58.01±7.88	5.000-7.070
Upper edge of the ilium	25.77±8.02	-63.05±9.88	-52,88±6,66	4.000-13.42
Spina iliaca anterior superior	52.05±12.35	-66.96±10.16	-76.60±12.54	3.030-11,170
On average:	36.57	-63.38	-59.56	

Table 2. Average measurements of Housfield units (HU) in overweight patients (n=36).

Level	Skin	Subcutaneous tissue	Internal fat	Subcutaneous tissue thickness (mm)
Sword-shaped process	13.02±3.02	-69.07±10.54	-75.89±9.54	6.010-7.920
Lower edge of the 12th rib	26.75±4.54	-77.88±11.21	-65.21±7.88	6.340-7.150
Navel level	19.65±3.78	-78.67±10.98	-73.11±10.32	7.120-7.140
Upper edge of the ilium	24.31±4.22	-69.78±8.78	-81.12±13.22	6.770-15.450
Spina iliaca anterior superior	31.15±5.44	-83.23±12.02	-75.45±10.88	5.430-13.230
On average:	22.97	-75.73	-74.16	

Table 3. Average measurements of Housfield units (HU) in patients (n=36) with grade I obesity.

Level	Skin	Subcutaneous tissue	Internal fat	Subcutaneous tissue thickness (mm)
Sword-shaped process	-10.21±2.56	-96.90±13.54	-83.95±9.88	14.34-31.93
Lower edge of the 12th rib	-14.03±3.48	-83.80±12.02	-83.79±8.76	15.96-45.98
Navel level	-17.78±5.24	-91.56±13.04	-93.29±10.42	15.10-50.97
Upper edge of the ilium	6.110±1.080	-85.54±12.45	-98.83±12.34	25.39-42.79
Spina iliaca anterior superior	-8.820±1.460	-95.04±14.22	-76.19±7.78	28.37-51.42
On average:	-8.950	-90.57	-86.81	

Table 4. Average measurements of Housfield units (HU) in patients (n=36) with grade II obesity.

Level	Skin	Subcutaneous tissue	Internal fat	Subcutaneous tissue thickness (mm)
Sword-shaped process	-22.32±5.46	-98.76±11.22	-95.20±9.54	16.02-49.60
Lower edge of the 12th rib	-16.20±54.22	-105.3±14.1	-119.5±15.3	19.37-30.19
Navel level	-19.80±4.68	-108.7±14.7	-106.6±14.6	32.01-93.04
Upper edge of the ilium	-6.040±0.680	-105.0±12.8	-118.2±15.1	19.48-103.7
Spina iliaca anterior superior	-20.79±5.36	-97.09±10.54	-110.6±13.7	42.96-107.0
On average	-17.04	-103.0	-110.0	

The decrease in the average Housefield unit (HU) measurements in overweight patients compared to people with normal weight was mainly statistically insignificant ($p \geq 0.05$), although a corresponding trend was observed. At the same time, a statistically significant difference in the reduction in measurements was found between patients with grade I obesity and people with normal body weight ($p \leq 0.05$), as well as between patients with grade II obesity and examined patients with normal body weight ($p \leq 0.01$).

For clarity, we constructed graphs of changes in the density of the corresponding tissues in patients with different body weights (Figs. 5-7).

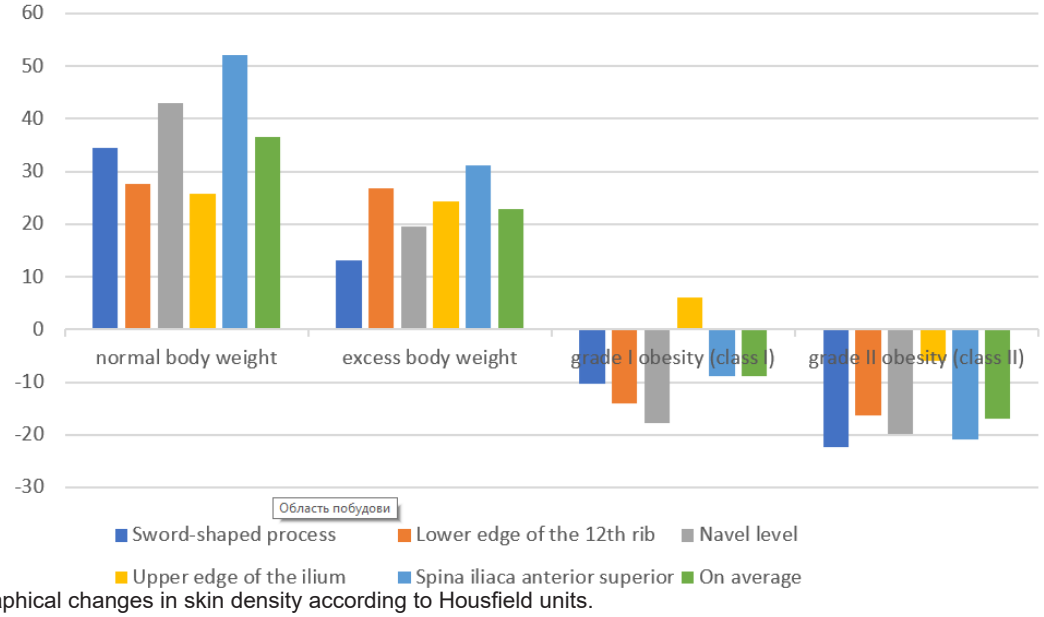

Fig. 5. Graphical changes in skin density according to Housfield units.

Fig. 6. Graphical changes in subcutaneous fat density according to Housfield units.

Fig. 7. Graphical changes in the density of intraperitoneal adipose tissue according to Housfield units.

Discussion

The literature has repeatedly pointed out the importance of determining the area of fat on CT cross-sections or studying the volume of subcutaneous fat and intraperitoneal deposits [18, 26], as well as the importance of CT values and their relationship to the distribution of adipose tissue and anthropometric indicators [11]. M. Pop and M. Mărușteri [21] indicate that the reference interval for visceral fat was determined as (-121.86:-84.18 HU), and the reference interval for subcutaneous fat as (-122.98:-93.21 HU), with a statistically significant difference between them. It should be remembered that higher radio density of adipose tissue in any location may reflect increased levels of local and systemic inflammation and other changes, such as increased vascularization [6, 7]. However, such data are relevant when comparing the results obtained in a single group of people (with the same body weight). The question arises whether there are changes in tissue density with an increase in body weight.

As can be seen from the tables and graphs we have presented, with an increase in body weight (degree of obesity), not only is there a clear increase in the thickness of subcutaneous adipose tissue and intra-abdominal fat in all “sections,” but there is also a statistically significant decrease in skin density.

In general, according to our surveys, the density of subcutaneous adipose tissue corresponds to the density of intraperitoneal fat in each category of people of the corresponding body weight, and their fluctuations are not statistically significant. However, to determine the level of change in fat tissue density between people of different body weights, we proposed a subcutaneous intraperitoneal fat density index (PFI), which was calculated using the formula PFI=SCF/IAF×100 %, where PFI (peritoneal fat index) is the peritoneal fat index, SCF (subcutaneous fat) is subcutaneous fat, and IAF (intra-abdominal fat) is intra-abdominal fat. After processing the data and substituting it into the formula, we obtained the corresponding results. Accordingly, the PFI in people with normal body weight was 106.4 units; in people who were overweight, it was 102.1 units; in people with grade I obesity, it was 104.3 units; and in people with grade II obesity, it was 93.62 units. As we can see, the index is not indicative in people with normal weight, overweight, and grade I obesity, but it decreases in people with grade II obesity ($p \leq 0.05$).

If we take the density of subcutaneous adipose tissue (-63.38 HU) as a unit, then the density of adipose tissue in people who are overweight will be reduced by 1.19 times, in people with grade I obesity – by 1.43 times, and in people with grade II obesity, it will be reduced by 1.62 times. Changes in the density of intraperitoneal fat are even more noticeable. If the density of intraperitoneal fat (-59.56 HU) is taken as a unit, then the density of fat in people who are overweight is reduced by a factor of 1.24, in people with grade I obesity by a factor of 1.46, and in people with grade II obesity – 1.85 times (in both cases, the value $p \leq 0.05$ between the indicators of people with normal weight and obesity).

Since the density of soft tissues decreases significantly with an increase in body weight, the risk of iatrogenic (surgical) damage increases, especially in patients with oncological pathology, as their resistance to mechanical damage decreases.

Considering that weight loss in general is a poor prognostic factor for some types of cancer [3], and that increased radio density of both subcutaneous and visceral adipose tissue is associated with a poor prognosis for cancer patients [10, 16, 19], it should be agreed that determining the radio density of adipose tissue based on computed tomography data obtained before surgery makes it possible to some extent to predict surgical difficulties [30]. At the same time, taking into account the characteristics of density at different degrees of obesity will have a significant impact on the overall conclusion of clinicians.

Conclusions

It has been proven that with an increase in body weight, the density of skin, subcutaneous adipose tissue, and intraperitoneal fat in Housefield units decreases, with this difference being particularly significant between people with normal body weight and those with grade II obesity.

References

[1] Ahmed, S. K., & Mohammed, R. A. (2025). Obesity: Prevalence, causes, consequences, management, preventive strategies and future research directions. *Metabolism Open*, *27*, 100375. doi: 10.1016/j.metop.2025.100375

[2] Baba, S., Jacene, H. A., Engles, J. M., Honda, H., & Wahl, R. L. (2010). CT Hounsfield units of brown adipose tissue increase with activation: preclinical and clinical studies. *Journal of Nuclear Medicine*, *51*(2), 246-250. doi: 10.2967/jnumed.109.068775

[3] Besutti, G., Ottone, M., Bonelli, E., Canovi, S., Farì, R., Farioli, F., ... & Giorgi Rossi, P. (2025). Inverse Association of Longitudinal Variations in Fat Tissue Radiodensity and Area. *Diagnostics*, *15*(13), 1662. doi: 10.3390/diagnostics15131662

[4] Biswas, S. (2023). Challenges in Imaging the Obese Patients. *Series of Clinical and Medical Case Reports and Reviews*, *1*, 6-12. doi: 10.54178/2993-3579.v1i1a1994

[5] Carla, M. M., Heymsfield, P. B., & Heymsfield, S. B. (2014). Lean tissue imaging: a new era for nutritional assessment and intervention. *Journal of Parenteral and Enteral Nutrition*, *38*(8), 940-953. doi: 10.1177/0148607114550189

[6] Coussens, L. M., & Werb, Z. (2002). Inflammation and cancer. *Nature*, *420*(6917), 860-867. doi: 10.1038/nature01322

[7] Deng, T., Lyon, C. J., Bergin, S., Caligiuri, M. A., & Hsueh, W. A. (2016). Obesity, inflammation, and cancer. *Annual Review of Pathology: Mechanisms of Disease*, *11*(1), 421-449. *doi: 10.1146/annurev-pathol-012615-044359*

[8] Ebadi, M., Dunichand-Hoedl, A. R., Rider, E., Kneteman, N. M., Shapiro, J., Bigam, D., … & Montano-Loza, A. J. (2022). Higher subcutaneous adipose tissue radiodensity is associated with increased mortality in patients with cirrhosis. *JHEP Reports*, *4*(7), 100495. doi: 10.1016/j.jhepr.2022.100495

[9] Fehrenbach, U., Hosse, C., Wienbrandt, W., Walter-Rittel, T., Kolck, J., Auer, T. A., … & Geisel, D. (2025). Concordance between single-slice abdominal computed tomography-based and bioelectrical impedance-based analysis of body composition in a prospective study. *European Radiology*, 1-12. doi: 10.1007/s00330-025-11746-3

[10] Feliciano, E. M. C., Winkels, R. M., Meyerhardt, J. A., Prado, C. M., Afman, L. A., & Caan, B. J. (2021). Abdominal adipose tissue radiodensity is associated with survival after colorectal cancer. *The American Journal of Clinical Nutrition*, *114*(6), 1917-1924. doi: 10.1093/ajcn/nqab285

[11] Ferland, M., Després, J.-P., Tremblay, A., Pinault, S., Nadeau, A., Moorjani, S., … & Bouchard, C. (1989). Assessment of adipose tissue distribution by computed axial tomography in obese women: Association with body density and anthropometric measurements. *British Journal of Nutrition*, *61*(2), 139-148. doi: 10.1079/BJN19890104

[12] Gifford, A., Walker, R. C., Towse, T. F., & Welch, E. B. (2015). Correlations between quantitative fat-water magnetic resonance imaging and computed tomography in human subcutaneous white adipose tissue. *J Med Imaging (Bellingham)*, *2*(4), 046001-046001. doi: 10.1117/1.JMI.2.4.046001

[13] Greenway, K., & Bell, D. (2022). *Hounsfield unit. Reference article, Radiopaedia. org*. https://radiopaedia.org/articles/hounsfield-unit

[14] Hanley, C., Shields, K. J., Matthews, K. A., Brooks, M. A., Janssen, I., Budoff, M. J., … & El Khoudary, S. R. (2018). Associations of cardiovascular fat radiodensity and vascular calcification in midlife women: The SWAN cardiovascular fat ancillary study. *Atherosclerosis*, *279*, 114-121. doi: 10.1016/j.atherosclerosis.2018.09.001

[15] Kelly, T., Yang, W., Chen, C. S., Reynolds, K., & He J. (2008). Global Burden of Obesity in 2005 and Projections to 2030. *International Journal of Obesity*, *32*(9), 1431-1437. doi: 10.1038/ijo.2008.102

[16] Machado, M. A., Moraes, T. F., Anjos, B. H., Alencar, N. R., Chang, T. M. C., Santana, B. C., ... & Netto, E. M. (2024). Association between increased Subcutaneous Adipose Tissue Radiodensity and cancer mortality: Automated computation, comparison of cancer types, gender, and scanner bias. *Applied Radiation and Isotopes*, *205*, 111181 doi: 10.1016/j.apradiso.2024.111181

[17] Micklesfield, L. K., Goedecke, J. H., Punyanitya, M., Wilson, K. E., & Kelly, T. L. (2012). Dual-Energy X-Ray Performs as Well as Clinical Computed Tomography for the Measurement of Visceral Fat. *Obesity (Silver Spring), 20*(5), 1109-1114. doi: 10.1038/oby.2011.367

[18] Nemoto, M., Yeernuer, T., Masutani, Y., Nomura, Y., Hanaoka, S., Miki, S., ... & Ohtomo, K. (2014). Development of automatic visceral fat volume calculation software for CT volume data. *Journal of Obesity*, *2014*(1), 495084. *doi: 10.1155/2014/495084*

[19] Pellegrini, M., Besutti, G., Ottone, M., Canovi, S., Bonelli, E., Venturelli, F., ... & El Ghoch, M. (2023). Abdominal fat characteristics and mortality in rectal cancer: a retrospective study. *Nutrients*, *15*(2), 374. doi: 10.3390/nu15020374

[20] Pierpont, Y. N., Dinh, T. P., Salas, R. E., Johnson, E. L., Wright, T. G., Robson, M. C., & Payne, W. G. (2014). Obesity and surgical wound healing: a current review. *International Scholarly Research Notices*, *2014*(1), 638936. doi: 10.1155/2014/638936

[21] Pop, M., & Măruşteri, M. (2023). Fat Hounsfield Unit Reference Interval Derived through an Indirect Method. *Diagnostics (Basel)*, *13*(11), 1913. doi: 10.3390/diagnostics13111913

[22] Powell-Wiley, T. M., Poirier, P., Burke, L. E., Després, J. P., Gordon-Larsen, P., Lavie, C. J., & American Heart Association Council on Lifestyle and Cardiometabolic Health; Council on Cardiovascular and Stroke Nursing; Council on Clinical Cardiology; Council on Epidemiology and Prevention; and Stroke Council. (2021). Obesity and cardiovascular disease: a scientific statement from the American heart association. *Circulation*, *143*(21), e984-e1010. doi **:**10.1161/CIR.000000000000097

[23] Ryo, M., Kishida, K., Nakamura, N., Yoshizumi, T., Funahashi, T., & Shimomura, L. (2014). Clinical significance of visceral adiposity assessed by computer tomography: A Japanese perspective. *World J Radiol*, *6*(7), 409-416. doi: 10.4329/wjr.v6.i7.409

[24] Tilves, C., Zmuda, J. M., Kuipers, A. L., Carr, J. J., Terry, J. G., Wheeler, V., … & Miljkovic, I. (2020). Associations of thigh and abdominal adipose tissue radiodensity with glucose and insulin in nondiabetic African-ancestry men. *Obesity (Silver Spring)*, *28*(2), 404-411. doi: 10.1002/oby.22695

[25] Sottier, D., Petit, J.-M., Guiu, S., Hamza, S., Benhamiche, H., Hillon, P., … & Guiu, B. (2013). Quantification of the visceral and subcutaneous fat by computed tomography: Interobserver correlation of a single slice technique. *Diagnostic and Interventional Imaging*, *94*(9), 879-884. doi: 10.1016/j.diii.2013.04.006

[26] Villegas-Valle, R. C., Lim, U., Maskarinec, G., Franke, A. A., Ernst, T., Fan, B., … & Shepherd, J. A. (2021). Metabolic syndrome screening using visceral adipose tissue (VAT) from opportunistic MRI locations in a multi-ethnic population. *Obesity research & clinical practice*, *15*(3), 227-234. doi: 10.1016/j.orcp.2021.03.007

[27] Westbury, S., Oyebode, O., van Rens, T., & Barber. T. M. (2023). Obesity Stigma: Causes, Consequences, and Potential Solutions. *Current Obesity Reports*, *12*(1), 10-23. doi: 10.1007/s13679-023-00495-3

[28] Weyer, C., Foley, J. E., Bogardus, C., Tataranni, P. A., & Pratley, R. E. (2000). Enlarged subcutaneous abdominal adipocyte size, but not obesity itself, predicts type II diabetes independent of insulin resistance. *Diabetologia*, *43*(12), 1498-1506. doi: 10.1007/s001250051560

[29] Yao, Z., Dardari, Z. A., Razavi, A. C., Silver, N., Jelwan, Y., Erhabor, J., … & Blaha, M. J. (2025). Prevalence of clinical obesity versus BMI-defined obesity among US adults: a cohort study. *The Lancet Diabetes & Endocrinology*, *13*, (8), 647-649. doi: 10.1016/S2213-8587(25)00159-7

[30] Zoabi, A., Bentov-Arava, E., Sultan, A., Elia, A., Shalev, O., Orevi, M., … & Margulis, K. (2023). Adipose tissue composition determines its computed tomography radiodensity. *European Radiology*, *34*(3), 1635-1644. doi: 10.1007/s00330-023-09911-7

ЗМІНИ ЩІЛЬНОСТІ М'ЯКИХ ТКАНИН ОРГАНІВ ЧЕРЕВНОЇ ПОРОЖНИНИ ТА ЧЕРЕВНОЇ СТІНКИ В ЗАЛЕЖНОСТІ ВІД МАСИ ТІЛА ЗА ДАНИМИ КОМП'ЮТЕРНОЇ ТОМОГРАФІЇ

Малишевський І. О., Хіміч С. Д., Іващук О. І., Ольхомяк О. О.

Ожиріння є поширеним явищем та хворобою, що потребує постійного розвитку оцінки морфофункціональних показників організму людей з ожирінням, в тому числі м'яких тканин. Мета дослідження – за даними комп'ютерної томографії провести визначення щільності шкіри, підшкірної клітковини та внутрішньоочеревинної жирової тканини у людей з різною масою тіла. Аналіз комп'ютерних томограм (КТ) та аналіз щільності тканин оцінювали в одиницях Хаусфілда (HU). Для стандартизації обчислень нами були відібрані КТ скани, котрі були виконані на рівні мечеподібного відростка, нижнього краю 12-го ребра, пупка, верхньої точки клубової кістки та на рівні spina iliaca anterior superior у людей з нормальною масою тіла (індекс маси тіла (ІМТ) 18,5-24,9), з надлишковою масою тіла (ІМТ 25,0-29,9), ожирінням І ступеня (ІМТ 30,0-34,9) та ожирінням ІІ ступеня (ІМТ 35,0-39,9). Визначено, що з ростом маси тіла та ступеня ожиріння, чітко прослідковується на всіх «зрізах» не тільки збільшення товщини підшкірно-жирової клітковини та внутрішньоочеревинного жиру, але й видно статистично достовірне зменшення щільності шкіри. Якщо взяти середню величину щільності підшкірно-жирової клітковини (-63,38 одиниць HU) за одиницю, то щільність клітковини у людей із зайвою масою тіла зменшується у 1,19 рази, у людей із І ступенем ожиріння – у 1,43 рази, а у людей із ІІ ступенем ожиріння – у 1,62 рази. Зміни щільності

внутрішньо-очеревинного жиру ще помітніші. Взявши величину щільності внутрішньо-очеревинного жиру (-59,56 одиниць HU) за одиницю, то щільність клітковини у людей із зайвою масою тіла зменшується у 1,24 рази, у людей із I ступенем ожиріння – у 1,46 рази, а у людей із II ступенем ожиріння – у 1,85 рази (p≤0,05 між показниками людей з нормальною масою тіла та ожирінням). Отже, зі збільшенням маси тіла щільність шкіри, підшкірно-жирової клітковини та внутрішньоочеревинного жиру за одиницями Хаусфілда зменшується. Така відмінність особливо суттєва між людьми з нормальною масою тіла та ожирінням II ступеня. Оскільки щільність м'яких тканин зі збільшенням маси тіла вірогідно зменшується, то зростає ризик ятрогенних (хірургічних) ушкоджень, адже зменшується стійкість їх до механічних ушкоджень.

Ключові слова: *м'які тканини, жирова тканина, шкіра, внутрішньоочеревинний жир, підшкірно-жирова клітковина, ожиріння, комп'ютерна томографія, діагностика, щільність тканин, одиниці Хаусфілда.*

Author's contribution

Malyshevskyj I. O. – collection of tomograms, data visualization, analysis of obtained data, project administration, resources, writing of the original draft text.

Khimich S. D. – research concept and methodology, literature review, manuscript editing.

Ivashchuk O. I. – software.

Olkhomiak O. O. – data visualization.

DOI: 10.31393/morphology-journal-2026-33(1)-08 Reports of Morphology, Vol. 32, №1, Pages 55-63

ISSN 1818-1295 eISSN 2616-6194

REPORTS OF MORPHOLOGY

Official Journal of the Scientific Society of Anatomists, Histologists, Embryologists and Topographic Anatomists of Ukraine

journal homepage: https://morphology-journal.com

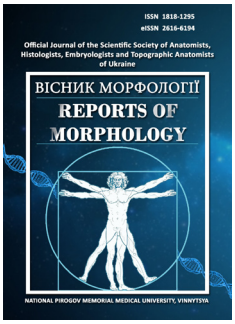

Modelling of the linear dimensions of dental arches in Ukrainian young men and young women with physiological occlusion and a wide facial type depending on the characteristics of Burstone cephalometric indicators and computed tomography tooth dimensions

Orlovskyi I. V., Beliaiev E. V., Yur A. M., Zakalata T. R., Isakova N. M., Romashkina O. A., Ruban M. M.

National Pirogov Memorial Medical University, Vinnytsya, Ukraine

ARTICLE INFO

Received: 7 August 2025

Accepted: 20 January 2026

UDC: 616.314-073.75:616.314.2-007.2:519.876.5

CORRESPONDING AUTHOR

e-mail: antilitsoooo@gmail.com

Orlovskyi I. V.

CONFLICT OF INTEREST

The authors have no conflicts of interest to declare.

FUNDING

Not applicable.

DATA SHARING

Data are available upon reasonable request to corresponding author.

The variability of the linear parameters of dental arches may be determined by craniofacial characteristics and tooth sizes. Conducting a study that will allow a more accurate description of the interaction, i.e., the relationships of these three structures within a specific population, will make it possible to increase the validity of orthodontic diagnosis and treatment. The selection of Burstone cephalometric parameters is the most appropriate, given the limited number of studies using this analysis in the Ukrainian population. The aim of the study – development and analysis of regression models of the linear dimensions of dental arches in Ukrainian young men and young women with physiological occlusion and a wide facial type depending on the characteristics of Burstone cephalometric indicators and computed tomography tooth dimensions. On primary computed tomography scans and cephalograms of 25 Ukrainian young men and 25 young women with physiological occlusion and a wide facial type, obtained from the databank of the Research Center and the Department of Pediatric Dentistry of the National Pirogov Memorial Medical University, Vinnytsia, measurements of linear and angular indicators by the Burstone method and the dimensions of teeth and dental arches were performed. Regression models of dental arch dimensions depending on cephalometric indicators and computed tomography tooth dimensions were built using the licensed package "Statistica 6.0". It was established that in young men and young women with physiological occlusion and a wide facial type, all 18 possible significant models of linear parameters necessary for constructing the correct shape of dental arches were built depending on the characteristics of Burstone cephalometric indicators and computed tomography tooth dimensions, with a coefficient of determination (R^2) greater than 0.6 (in young men R^2= from 0.829 to 0.980, $p<0.001$ in all cases; in young women R^2= from 0.680 to 0.962, $p<0.001$ in all cases). Analysis of the frequency of inclusion of computed tomography tooth dimensions and Burstone cephalometric indicators in the models showed: in young men, cephalometric indicators were included most often (23.70 %), the width of the crown part of the corresponding teeth in the mesiodistal plane (20.74 %), and the width of the crown part of the corresponding teeth in the vestibulo-oral plane (17.04 %); in young women, cephalometric indicators were included most often (27.21 %), the width of the crown part of the corresponding teeth in the mesiodistal plane (13.24 %), the width of the crown part of the corresponding teeth in the vestibulo-oral plane (11.03 %), and the width of the cervical part of the corresponding teeth in the vestibulo-oral plane (10.29 %). Analysis of the frequency of inclusion of the corresponding teeth in the models showed: in young men, maxillary lateral incisors and canines were included most often (13.59 % each), maxillary central incisors (11.65 %), and mandibular canines (10.68 %); in young women, maxillary central incisors were included most often (23.23 %), mandibular canines (14.14 %), mandibular lateral

incisors (13.13 %), maxillary lateral incisors (12.12 %), mandibular central incisors (11.11 %), and maxillary canines (10.10 %).
Keywords: *dentistry, Burstone cephalometry, computed tomography dimensions of teeth and dental arches, young men and young women, facial type, physiological occlusion, regression analysis.*

Introduction

Malocclusion is the third most common pathology of the oral cavity, after caries and periodontal diseases. The global prevalence of malocclusion is 54.83 %, with the highest rates in Asia at 61.81 % and Europe at 61.50 %, and the lowest in Africa at 32.50 %. Regional differences were also noted in the prevalence of anterior open bite – in Africa the prevalence is 18.60 %, whereas in Europe it is 4.46 %. Deep bite, conversely, was most frequent in Europe – 33.08 % and the rarest in Africa – 6.30 % [8]. A meta-analysis of 11 studies including a total of more than 13 thousand individuals showed that the prevalence of Class I malocclusion was 56 %, Class II – 31 %, Class III – 11 %, with the most frequently detected traits being crowding (41%), increased overjet (34 %), negative overjet (13 %), crossbite (11 %), anterior open bite (7 %), and diastemas (4 %) [18].

Data from a survey of 1144 schoolchildren in Turkey showed that normal occlusion was observed in only 2.6 % of children. Most frequently, the examined individuals had Class I malocclusion – 53.3 %, Class II – 20.8 %, and Class III – 7.4 %. In addition, anterior crossbite was found in 6.5 %, posterior crossbite in 10 % – deep bite in 22.6 %, and open bite in 2.3 %. It is important to note that onychophagia was recorded in 41% of children, which is considered one of the causes of malocclusion development [3]. In Saudi Arabia, the prevalence of malocclusion is 72 %, with the prevalence of each class at the following levels: Class I – 66.51 %, Class II – 17.70 %, Class III – 15.79 % [10].

Examination of 1960 children aged 3-5 years in North-Eastern Italy revealed that 3.7 % of them had crossbite. Specifically, anterior crossbite was present in 3.3 %, posterior right crossbite in 3.7 %, posterior left crossbite in 2.9 %, and bilateral crossbite in 0.6 %. No statistically significant differences in prevalence distribution by age or sex were found by the researchers [12].

A review of 721 children in India revealed that the prevalence of anterior crossbite was 26.7 %. In particular, in 11.4 % of patients with anterior crossbite it was combined with posterior crossbite. 62 % of patients had unilateral involvement and 38% had bilateral involvement. Mandibular shift was also noted in 48.19 % of cases, gingival recession in 22.3 %, and mobility of the lower incisors in 6.2 % [26].

In Vietnam, the prevalence of malocclusion is 60.7 %, specifically Class I was present in 19 %, Class II in 31 %, and Class III in 10.7 %. An analysis of various harmful habits found that finger sucking was associated with Class I (OR 3.28) and Class II (OR 3.22), lip biting – with Class II (OR 4.37) and Class III (OR 6.83), tongue thrusting increased the likelihood of Class I (OR 5.25) and Class II (OR 6.42), and mouth breathing was associated with a higher likelihood of Class II (OR 2.71) [28].

In China, among children aged 3-5 years (a total of 2335 children examined), the prevalence of malocclusion was 83.9 %. The most frequently detected traits were deep bite (63.7 %), increased overjet (33.9 %), midline deviation (26.6 %), anterior crossbite (8.0 %), and anterior crowding (6.5 %). No statistically significant differences by gender were found [30].

A long-term study was conducted by Finnish scientists. A total of 1964 individuals born in 1966 participated, who at the end of the study were 46 years old. During the examination, 39.5 % had signs of malocclusion. The most frequently detected traits were crossbite (17.9 %), deep bite ≥6 mm (11.7 %), and increased overjet ≥6 mm (9.7 %). These results show that orthodontic disorders are a frequent phenomenon, even in a cohort of individuals who had been treated in childhood [16].

Orthodontic pathologies (such as malocclusion), unlike other oral diseases, require long-term and costly treatment. In England, NHS expenditure on primary orthodontic services is approximately £250 million per year. 7.6 % of treatments ended in early termination, corresponding to approximately £2.3 million in expenditure, 5.2 % of cases ended with “residual need” according to IOTN (expenditure about £1.6 million), and due to missing data another £13.2 million. Thus, in total 44 % of expenditure is potentially inefficient [22]. This, in particular, encourages initiating orthodontic treatment as early as possible, which will subsequently reduce its cost [24], and will satisfy the patient’s aesthetic outcome [29]. Therefore, there is a need for a more thorough assessment of data concerning individuals of young age.

The aim of the study – development and analysis of regression models of the linear dimensions of dental arches in Ukrainian young men and young women with physiological occlusion and a wide facial type depending on the characteristics of Burstone cephalometric indicators and computed tomography tooth dimensions.

Materials and methods

Primary computed tomography scans and cephalograms of 25 Ukrainian young men (aged 17 to 21 years) and 25 Ukrainian young women (aged 16 to 20 years) with physiological occlusion and a wide facial type were obtained from the databank of the Research Center and the Department of Pediatric Dentistry of the National Pirogov Memorial Medical University, Vinnytsya. Computed tomography (using the dental cone-beam computed tomography scanner Planmeca ProMax 3D Mid, Finland) and cephalometric radiographic (using the dental cone-beam computed tomography scanner Veraviewepocs 3D Morita, Japan) examinations were performed on the basis of the

principle of voluntary informed consent at the private dental clinic “Vinintermed” and at the “Planmeca 3D Maxillofacial Diagnostic Center”. The Bioethics Committee of the National Pirogov Memorial Medical University, Vinnytsya (Protocol No. 6 dated 07.05.2025) established that the conducted studies do not contradict the basic bioethical standards of the Declaration of Helsinki, the Council of Europe Convention on Human Rights and Biomedicine (1977), relevant WHO provisions, and the laws of Ukraine.

Measurements of cephalometric parameters were performed according to the method of Burstone C. J. [7] in the OnyxCeph³™ application, version 3DPro (Image Instruments GmbH, Germany), on cephalograms obtained in a standard manner and created in the 3D Slicer v5.4.0 software with points marked on 3D objects.

According to this methodology, the following were determined: cranial base indicators and horizontal skeletal indicators (Fig. 1); vertical skeletal and dental indicators (Fig. 2); intermaxillary indicators (Fig. 3); dentoalveolar indicators (Fig. 4).

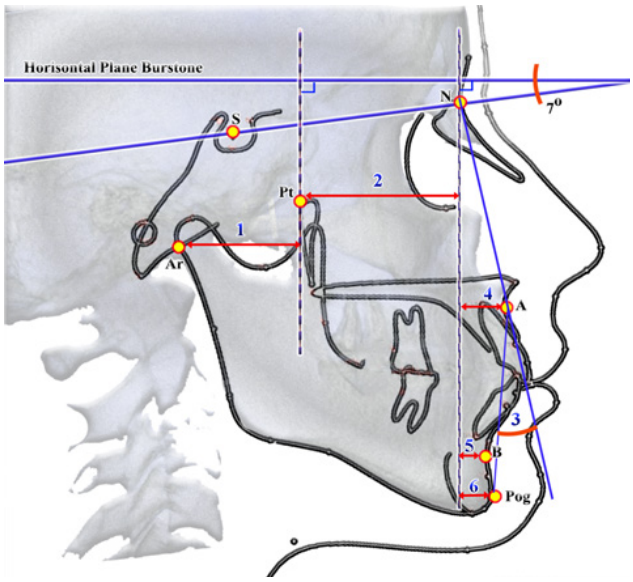

Fig. 1. Cranial base indicators and horizontal skeletal indicators according to the Burstone method. 1 – distance Ar-Pt (mm); 2 – distance Pt-N (mm); 3 – angle N-A-Pog (°); 4 – distance N-A (mm); 5 – distance N-B (mm); 6 – distance N-Pog (mm).

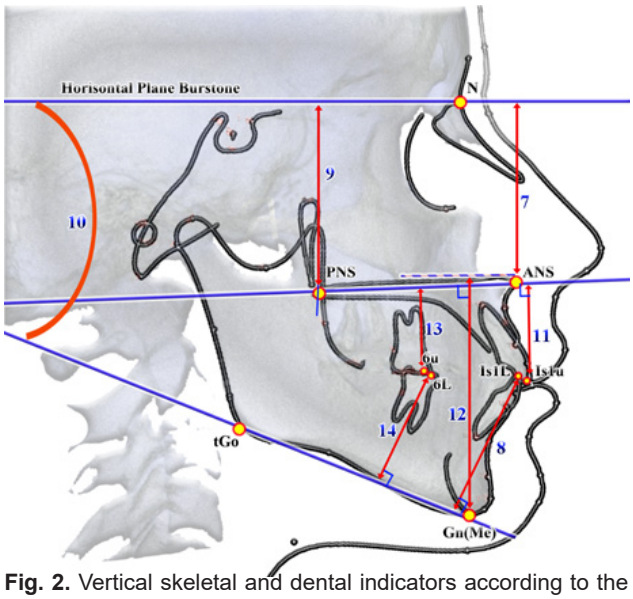

Fig. 2. Vertical skeletal and dental indicators according to the Burstone method. 7 – distance N-ANS (mm); 8 – distance ANS-Gn (mm); 9 – distance PNS-N (mm); 10 – angle MP-HP (°); 11 – distance 1u-NF (mm); 12 – distance 1l-MP (mm); 13 – distance 6u-NF (mm); 14 – distance 6l-MP (mm).

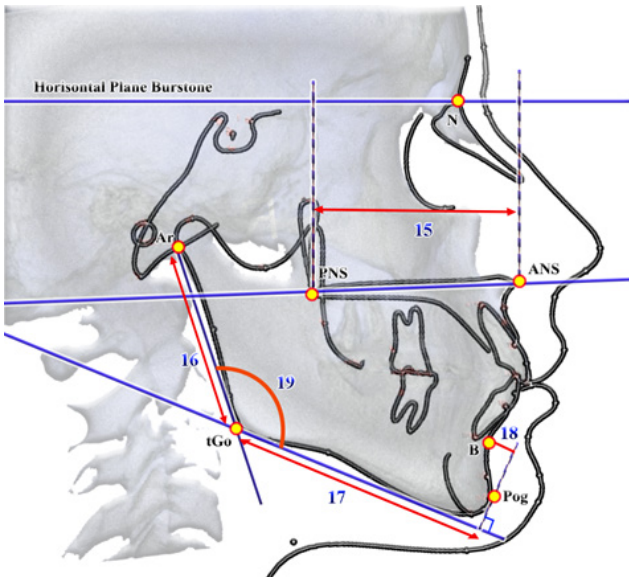

Fig. 3. Intermaxillary indicators according to the method. 15 – distance ANS-PNS (mm); 16 – distance Ar-Go (mm); 17 – distance Go-Pog (mm); 18 – distance B-Pog (mm); 19 – angle arGoMe/ArGoGn (Ar-Go_Gn) (°).

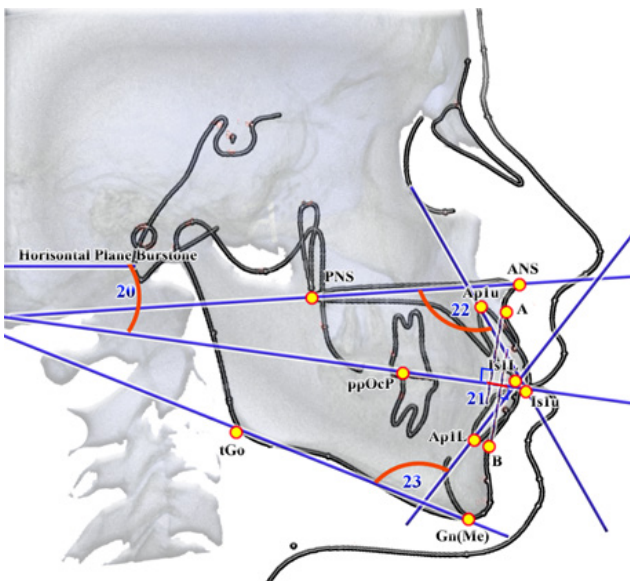

Fig. 4. Dentoalveolar indicators according to the method. 20 – angle OP-HP **(°)**; 21 – distance A-B (mm); 22 – angle Max1-SpP/Max1-NF (Max1-NF) (°); 23 – angle Mand1-MeGo/Mand1-Mp (Mand1-MP) (°).

Morphometric assessment of teeth and dental arches was performed using the software applications i-Dixel One Volume Viewer (Ver.1.5.0) J Morita Mfg. Cor and Planmeca Romexis Viewer (ver. 3.8.3.R 15.12.14) Planmeca OY.

Tooth morphometry included determination of the following distances (mm) [23]: the width and length of the crown part of the corresponding teeth in the mesiodistal (MdK and MdLK, respectively) and vestibulo-oral (VoK and VoLK, respectively) planes; the width of the cervical part of the corresponding teeth in the mesiodistal (MdC) and vestibulo-oral (VoC) planes; the length of the root part of the corresponding teeth in the mesiodistal (MdLR) and vestibulo-oral (VoLR) planes; and the length of the corresponding teeth (MdLD).

Since previous studies did not reveal significant differences or trends when comparing computed tomography dimensions of homonymous teeth on the right and left sides of the maxilla and mandible [19], we used mean values for the corresponding teeth: 11 or 41 – maxillary or mandibular central incisors, 12 or 42 – maxillary or mandibular lateral incisors, 13 or 43 – maxillary or mandibular canines, 14 or 44 – maxillary or mandibular first premolars, 15 or 45 – maxillary or mandibular second premolars, 16 or 46 – maxillary or mandibular first molars.

Dental arch morphometry included determination of the following distances (mm) [23]: in the transverse plane – PonM, PonPr, VestBM, 13_23Bugr, 13_23Apx, 33_43Bugr, 33_43Apx, mapex_6, napx_6, dapx_6, dapx_46, and mapx_46; in the sagittal plane – DL_C, DL_F, and DL_S; in the vertical plane – GL_1, GL_2, and GL_3.

Using the licensed statistical package “Statistica 6.0”, stepwise regression analysis was applied to model the linear dimensions of dental arches depending on the characteristics of Burstone cephalometric indicators and computed tomography tooth dimensions.

Results

In *young men* with physiological occlusion and a wide facial type, regression models (with a coefficient of determination R^2>0.60) of the linear dimensions required to construct the correct shape of dental arches depending on the characteristics of Burstone cephalometric indicators and computed tomography tooth dimensions take the form of the following linear equations:

distance PonPr= 8.495 + 2.199×MdK12 + 0.661×MdLK43 + 2.573×VoK11 - 0.989×MdLK11 - 1.932×VoK42 + 1.400×VoK44 - 0.763×VoK14 + 0.167×1l-MP (R^2=0.947, $F_{(8.16)}$=35.73, p<0.001, Std.Error of estimate=0.588);

distance PonM= 27.81 + 2.165×VoK15 + 0.172×ANS-Gn - 0.197×Ar-Pt + 0.255×Go-Pog - 0.221×Mand1-MP - 0.667×B-Pog + 0.426×VoLK13 (R^2=0.922, $F_{(7.17)}$=28.89, p<0.001, Std.Error of estimate=0.807);

distance 13_23Bugr= -15.00 + 1.717×MdK12 + 0.420×MdLD15 + 0.941×VoLK41 + 1.895×VoK11 - 0.532×MdLD45 + 1.290×VoK16 + 0.446×VoLR11 + 0.332×B-Pog - 0.136×1u-NF (R^2=0.978, $F_{(9.15)}$=74.56, p<0.001, Std.Error of estimate=0.400);

distance 13_23Apx= 15.98 + 0.529×N-ANS - 2.975×MdC42 + 2.918×MdK15 - 0.860×MdLR42 - 1.145×MdLK13 + 0.467×MdLD14 - 0.597×VoK14 (R^2=0.913, $F_{(7.16)}$=24.01, p<0.001, Std.Error of estimate=0.830);

distance VestBM= 68.74 + 2.209×VoK15 - 0.305×Ar-Go_Gn - 0.213×Mand1-MP + 1.603×MdK15 + 0.458×1l-MP - 0.331×VoLR11 (R^2=0.938, $F_{(6.18)}$=45.06, p<0.001, Std.Error of estimate=0.786);

distance napx_6= -20.79 + 0.871×PNS-N + 3.620×VoC43 - 8.172×MdK42 + 0.175×Max1-NF - 1.072×VoLR41 + 0.925×VoLR43 + 3.046×VoC11 - 0.651×MdLR11 (R^2=0.942, $F_{(8.16)}$=32.36, p<0.001, Std.Error of estimate=0.951);

distance dapx_6= 0.156 + 4.432×VoC13 + 2.283×MdK46 - 0.539×MdLD42 + 0.582×MdLD13 - 2.408×VoK12 + 0.436×N-A + 2.931×VoK44 - 3.047×VoC41 (R^2=0.928, $F_{(8.16)}$=25.83, p<0.001, Std.Error of estimate=1.447);

distance mapex_6= -30.13 + 3.863×MdK45 + 1.863×MdK12 + 5.909×MdK15 + 3.338×MdC41 + 0.179×Go-Pog - 1.066×VoLK41 - 1.787×MdK14 (R^2=0.946, $F_{(7.17)}$=42.33, p<0.001, Std.Error of estimate=0.969);

distance 33_43Bugr= -4.076 + 3.659×MdK42 - 0.085×N-A-Pog + 1.417×MdK12 - 1.190×MdK14 + 0.419×MdLD43 - 0.434×MdLD13 + 1.488×VoK41 (R^2=0.829, $F_{(7.17)}$=11.78, p<0.001, Std.Error of estimate=0.784);

distance 33_43Apx= 4.671 - 0.565×A-B + 1.296×MdLK43 - 0.678×MdLK42 - 0.723×MdLD44 + 2.910×VoC12 + 2.225×MdC41 + 0.425×MdLD14 - 0.437×VoLR43 (R^2=0.859, $F_{(8.16)}$=12.18, p<0.001, Std.Error of estimate=1.036);

distance mapx_46= -12.98 + 4.249×MdK16 + 1.009×MdLD43 + 1.573×VoK16 - 0.265×Pt-N - 1.271×VoLR12 + 1.879×VoC43 - 0.911×VoLK13 + 0.096×Ar-Go (R^2=0.955, $F_{(8.15)}$=39.58, p<0.001, Std.Error of estimate=0.751);

distance dapx_46= 14.29 - 0.211×Mand1-MP + 2.306×VoK16 + 2.572×MdC12 + 3.420×MdK16 + 0.211×N-A - 1.874×MdK46 + 0.335×MdLD13 (R^2=0.926, $F_{(7.16)}$=28.51, p<0.001, Std.Error of estimate=0.970);

distance DL_C= -16.35 + 1.882×MdK11 + 0.434×VoLK13 + 0.161×1l-MP - 0.522×VoK46 + 0.083×Pt-N - 0.200×VoLK41 + 0.389×VoK12 (R^2=0.950, $F_{(7.17)}$=46.24, p<0.001, Std.Error of estimate=0.337);

distance DL_F= -23.88 + 2.616×MdK11 + 1.881×VoK12 + 0.513×VoLK13 + 0.817×MdK44 - 0.195×MdLR13 + 1.095×MdK15 - 0.704×VoK45 + 0.427×VoK14 - 1.075×VoC41 + 0.026×MP-HP (R^2=0.980, $F_{(10.14)}$=67.98, p<0.001, Std.Error of estimate=0.281);

distance DL_S= -7.963 + 3.007×MdK11 - 0.358×MdLR12 + 0.255×VoLK11 + 0.903×VoK12 + 0.562×MdLK13 + 0.537×VoK14 + 0.043×N-A-Pog (R^2=0.964, $F_{(7.17)}$=65.23, p<0.001, Std.Error of estimate=0.417);

distance GL_1= -17.53 + 0.366×N-A-Pog - 2.153×VoLR12 + 3.097×MdK13 + 1.129×VoLR43 - 1.729×MdK43 + 0.156×Max1-NF + 0.276×1l-MP (R^2=0.889, $F_{(7.17)}$=19.51, p<0.001, Std.Error of estimate=1.023);

distance GL_2= 32.80 + 1.817×MdK13 - 0.386×Ar-Go - 3.960×VoK46 + 2.526×MdK43 - 1.029×MdLR12 +

0.886×MdLD15 + 1.489×VoK45 (R^2=0.870, $F_{(7.17)}$=16.30, p<0.001, Std.Error of estimate=1.219);

distance GL_3= 17.92 + 0.679×6u-NF - 0.329×Ar-Pt + 1.444×MdK13 - 3.542×MdK16 + 1.117×MdLK11 + 2.318×MdK14 - 0.386×MdLK41 (R^2=0.900, $F_{(7.17)}$=21.87, p<0.001, Std.Error of estimate=0.792);

where, here and in the following equations, R^2 – coefficient of determination; $F_{(!)}$=! – critical $_{(!)}$ and obtained (!) Fisher's test value; p – confidence level; Std.Error of estimate – standard error of estimate.

In *young women* with physiological occlusion and a wide facial type, regression models (with a coefficient of determination R^2>0.60) of the linear dimensions required to construct the correct shape of dental arches depending on the characteristics of Burstone cephalometric indicators and computed tomography tooth dimensions take the form of the following linear equations:

distance PonPr= 3.131 + 2.881×MdK11 + 2.410×VoK11 - 2.941×VoK41 - 0.336×A-B + 1.006×MdC11 (R^2=0.693, $F_{(5.19)}$=8.60, p<0.001, Std.Error of estimate=1.349);

distance PonM= 9.226 + 2.564×MdK11 + 0.144×1u-NF + 1.071×MdLD11 - 0.725×MdLD41 - 2.732×VoC41 + 5.039×VoC42 - 2.530×VoK13 + 0.141×Ar-Go (R^2=0.852, $F_{(8.16)}$=11.55, p<0.001, Std.Error of estimate=1.163);

distance 13_23Bugr= 10.88 + 2.428×MdK11 + 2.690×VoC12 - 0.221×A-B - 0.616×VoLK42 + 0.320×B-Pog - 0.099×Max1-NF - 0.021×MdC43 (R^2=0.955, $F_{(7.17)}$=51.10, p<0.001, Std.Error of estimate=0.496);

distance 13_23Apx= 16.87 + 4.673×MdK12 + 0.053×MdC43 + 5.397×MdK11 - 6.750×MdK43 - 0.635×VoLR41 + 1.045×VoC43 - 2.323×MdC11 + 0.434×B-Pog - 1.788×MdC13 (R^2=0.962, $F_{(9.15)}$=42.74, p<0.001, Std.Error of estimate=0.682);

distance VestBM= -11.36 + 0.903×MdLD11 - 3.687×VoC41 + 5.056×MdK42 + 1.998×VoLK43 + 7.303×VoC43 - 7.480×VoK43 + 0.888×MdLK43 + 1.853×MdK16 - 0.971×VoLK11 + 0.173×Ar-Pt (R^2=0.945, $F_{(10.14)}$=24.27, p<0.001, Std.Error of estimate=0.804);

distance napx_6= 3.182 + 0.664×1u-NF - 0.246×Go-Pog - 1.448×MdLR12 + 0.594×MdLD14 + 1.312×MdLK42 + 0.324×Ar-Pt - 1.040×MdK46+ 1.640×VoLK13+ 0.754×MdLD44 (R^2=0.944, $F_{(9.15)}$=27.90, p<0.001, Std.Error of estimate=1.092);

distance dapx_6= -41.46 + 5.752×VoC12 + 1.143×Ar-Pt + 0.895×MdLD15 - 1.132×MdLR13 + 2.581×MdLD42 - 1.668×MdLD41 + 0.832×B-Pog (R^2=0.854, $F_{(7.17)}$=14.16, p<0.001, Std.Error of estimate=2.121);

distance mapex_6= 12.84 + 2.773×MdLK11 + 1.443×MdLD12 + 0.411×ANS-PNS - 3.963×MdK44 - 1.224×VoLR41 + 0.900×MdLD45 - 0.759×MdLD11 (R^2=0.900, $F_{(7.17)}$=21.86, p<0.001, Std.Error of estimate=1.326);

distance 33_43Bugr= 2.621 - 1.873×VoK45 + 2.840×VoC12 + 1.733×MdK16 - 1.467×MdK46 + 0.119×Max1-NF + 1.114×VoC43 (R^2=0.680, $F_{(6.18)}$=6.38, p<0.001, Std.Error of estimate=1.514);

distance 33_43Apx= -19.93 - 1.830×MdLK42 + 3.774×MdC42 + 0.552×Ar-Pt + 1.212×MdLK13 + 1.513×VoK11 - 0.136×N-A-Pog + 0.169×MP-HP (R^2=0.878, $F_{(7.17)}$=17.41, p<0.001, Std.Error of estimate=1.164);

distance mapx_46= 34.20 + 3.075×MdK11 - 0.050×MdC43 + 0.198×N-Pog + 0.830×B-Pog - 2.164×VoLK42 + 1.421×VoK45 - 0.213×1I-MP (R^2=0.885, $F_{(7.16)}$=17.59, p<0.001, Std.Error of estimate=1.304);

distance dapx_46= 35.68 + 0.683×N-Pog + 1.017×VoLR11 + 2.790×MdC12 - 0.568×N-A - 0.807×MdLR43 + 0.581×MdLR41 (R^2=0.938, $F_{(6.17)}$=43.02, p<0.001, Std.Error of estimate=1.210);

distance DL_C= -7.984 + 0.102×Max1-NF + 0.855×VoK12 + 0.588×MdK46 - 0.037×Ar-Go_Gn - 0.199×6u-NF + 0.079×Pt-N - 0.072× OP-HP (R^2=0.898, $F_{(7.17)}$=21.47, p<0.001, Std.Error of estimate=0.451);

distance DL_F= -11.70 + 3.009×VoC12 + 1.101×MdK16 - 0.465×B-Pog + 0.184×Pt-N - 0.724×MdLK42 + 0.473×MdLK11 - 0.080×N-B - 0.707×VoK11 + 1.396×MdC13 - 0.139×N-ANS (R^2=0.936, $F_{(10.14)}$=20.45, p<0.001, Std.Error of estimate=0.544);

distance DL_S= -18.19 + 3.162×VoC12 + 1.807×MdK16 + 1.819×VoK41 - 1.456×MdC12 + 0.067×Mand1-MP + 0.880×VoK15 - 0.601×VoK45 (R^2=0.931, $F_{(7.17)}$=32.70, p<0.001, Std.Error of estimate=0.576);

distance GL_1= 23.17 - 0.382×OP-HP - 0.907×VoLR11 + 0.485×VoLR13 - 1.714×MdC42 + 1.652×MdK11 - 2.020×MdK13 + 0.399×VoLK11 (R^2=0.871, $F_{(7.17)}$=16.45, p<0.001, Std.Error of estimate=0.778);

distance GL_2= 10.70 - 1.244×VoLK43 + 0.398×6u-NF + 1.690×VoC43 - 2.783×VoK41 + 1.318×VoLK42 - 0.815×MdLD11 + 0.422×VoLR13 + 0.422×VoK11 (R^2=0.827, $F_{(8.16)}$=9.58, p<0.001, Std.Error of estimate=1.342);

distance GL_3= 0.688 + 0.559×VoLR43 + 5.103×VoC42 - 3.367×VoK41 + 0.335×6u-NF + 1.085×MdLK12 + 1.105×MdC11 - 0.735×MdLK42 - 2.400×VoC13 + 0.158×N-A-Pog (R^2=0.929, $F_{(9.15)}$=21.87, p<0.001, Std.Error of estimate=0.752).

Discussion

Thus, in *young men* with physiological occlusion and a wide facial type, all 18 possible significant (p<0.001 in all cases) models of linear parameters required to construct the correct shape of dental arches were built depending on the characteristics of *Burstone* cephalometric indicators and computed tomography tooth dimensions, with a coefficient of determination greater than 0.6 (respectively R^2= from 0.829 to 0.980).

When analyzing the frequency of inclusion of *Burstone* cephalometric indicators and computed tomography tooth dimensions in the regression equations in *young men* with physiological occlusion and a wide facial type, the following percentages of inclusion of these indicators into the models were established: cephalometric indicators (23.70 %), width of the crown part of the corresponding teeth in the mesiodistal plane (20.74 %), width of the crown part of the corresponding teeth in the vestibulo-oral plane (17.04 %), length of the

corresponding teeth (8.89 %), length of the crown part of the corresponding teeth in the mesiodistal and vestibulo-oral planes and length of the root part of the corresponding teeth in the vestibulo-oral plane (5.93 % each), width of the cervical part of the corresponding teeth in the vestibulo-oral plane (5.19 %), length of the root part of the corresponding teeth in the mesiodistal plane (3.70 %), width of the cervical part of the corresponding teeth in the mesiodistal plane (2.96 %).

When analyzing the frequency of inclusion of the corresponding teeth in the regression equations in *young men* with physiological occlusion and a wide facial type, the following percentages of inclusion of these indicators into the models were established: maxillary incisors (25.25 % of all variables, including 11.65 % central incisors and 13.59 % lateral incisors), mandibular incisors (16.51 % of all variables, including 9.71 % central incisors and 6.80 % lateral incisors), maxillary canines (13.59 %), mandibular canines (10.68 %), maxillary premolars (16.51 % of all variables, including 8.74 % first and 7.77 % second), mandibular premolars (7.76 % of all variables, including 3.88 % first and 3.88 % second), maxillary first molars (5.83 %), mandibular first molars (3.88 %).

In *young women* with physiological occlusion and a wide facial type, all 18 possible significant ($p<0.001$ in all cases) models of linear parameters required to construct the correct shape of dental arches were also built depending on the characteristics of *Burstone* cephalometric indicators and computed tomography tooth dimensions, with a coefficient of determination greater than 0.6 (respectively R^2= from 0.680 to 0.962).

When analyzing the frequency of inclusion of *Burstone* cephalometric indicators and computed tomography tooth dimensions in the regression equations in *young women* with physiological occlusion and a wide facial type, the following percentages of inclusion of these indicators into the models were established: cephalometric indicators (27.21 %), width of the crown part of the corresponding teeth in the mesiodistal plane (13.24 %), width of the crown part of the corresponding teeth in the vestibulo-oral plane (11.03 %), width of the cervical part of the corresponding teeth in the vestibulo-oral plane (10.29 %), length of the corresponding teeth and width of the cervical part of the corresponding teeth in the mesiodistal plane (8.82 % each), length of the crown part of the corresponding teeth in the mesiodistal plane (6.62 %), length of the crown part of the corresponding teeth in the vestibulo-oral plane (5.88 %), length of the root part of the corresponding teeth in the vestibulo-oral plane (5.15 %), length of the root part of the corresponding teeth in the mesiodistal plane (2.94 %).

When analyzing the frequency of inclusion of the corresponding teeth in the regression equations in *young women* with physiological occlusion and a wide facial type, the following percentages of inclusion of these indicators into the models were established: maxillary incisors (35.35 % of all variables, including 23.23 % central incisors and 12.12 % lateral incisors), mandibular incisors (24.24 % of all variables, including 11.11 % central incisors and 13.13 % lateral incisors), maxillary canines (10.10 %), mandibular canines (14.14 %), maxillary premolars (3.03 % of all independent variables, including 1.01 % first and 2.02 % second), mandibular premolars (6.06 % of all variables, including 2.02 % first and 4.04 % second), maxillary first molars (4.04 %), mandibular first molars (3.03 %).

The studies most closely related in topic to our research are the works performed by Brotskyi N. O. and co-authors, which, in addition, were also conducted in a Ukrainian population corresponding to our age category. However, in his studies a cephalometric analysis method according to Ricketts was used. In one of the studies, the correlation between cephalometric indicators and the dimensions of teeth and dental arches was assessed. Without taking facial type into account, the proportion of associations with maxillary tooth dimensions was 7.76 % in young men and 9.39 % in young women, with mandibular tooth dimensions – 9.39 % in young men and 8.98% in young women, with dental arch dimensions 24.60 % in young men and 10.32% in young women [4]. In another study, regression models of linear dimensions required to construct the correct shape of dental arches were built. For young men and young women, all 18 possible significant models ($p<0,001$) with a coefficient of determination >0,6 were constructed. The variables most frequently included in the models were, in young men, teleradiometric indicators (27.35 %), the width of the crown part in the mesio-distal direction (20.51 %) and in the vestibulo-oral direction (17.09 %), the distance from the incisal edge to the root apex (11.11 %); in young women, teleradiometric indicators (37.50 %), crown width in the mesio-distal direction (18.75 %), the width of the enamel-dentin junction and the distance from the incisal edge to the root apex (8.04 % each) [5]. In the most recent work, correlations between teleradiometric indicators according to Ricketts and CT dimensions of teeth and dental arches were analyzed. Correlations between teleradiometric indicators and tooth dimensions were of moderate strength and amounted to r from 0.32 to 0.50 [6].

Assessment of cephalometric and dento-maxillary indicators in a sample of 113 individuals with Class III malocclusion did not reveal any statistically significant associations between the magnitude of anterior Bolton discrepancy and cephalometric indicators, such as SNA ($r=-0,046$; $p=0,629$), ANB ($r=-0,089$; $p=0,348$) and others [1]. The results of another similar study showed manifestations of sexual dimorphism, in particular, in men most linear arch dimensions were statistically significantly larger than in women ($p<0.05$), although no such differences were found for the Bolton ratio [21].

Assessment of 100 plaster models (50 men and 50 women) showed the presence of moderately strong associations between crown diameters and dental arch length, with coefficients up to 0.60-0.62 for mandibular arch length and up to 0,68 between maxillary arch length and individual crown diameters [2].

When analyzing plaster models of mixed dentition

(100 models of boys and girls aged 7-10 years), low but significant inverse associations were found between the mesio-distal diameters of certain teeth and the magnitude of the arch "space deficiency". In girls, for the maxilla r=-0.383 (p=0.001) for 11 and r=-0.383 (p=0.001) for 21 were found, for the mandible r=-0.341 (p=0.004) for 42, and in boys for the mandible r=-0.369 (p=0.038) for 46 [9].

In an Egyptian sample of children aged 11-16 years, in the mandible a significant direct association was found between AP and AL (r=0.641; p=0.006) and between CMWT and AL (r=0.618; p=0.008). At the same time, for the maxilla no significant associations were established [11]. In another study with a similar age sample, the TS-ALD index in the maxilla had moderate direct associations with arch length (r=0.241; p=0.031), anterior arch length (r=0.315; p=0.004), and intermolar width (r=0.325; p=0.003), and in the mandible inverse correlations with the mandibular plane angle (r=-0.287; p=0.048) [13].

F. A. Kareem and co-authors established that the upper arch perimeter is most strongly associated with arch length (r=0.769), intermolar width (r=0.670) and intercanine width (r=0.640), whereas in the mandible the perimeter correlates more strongly with intermolar width (r=0.708) and intercanine width (r=0.684), and the association with arch length was weaker (r=0.273) [14].

S. Singh and G. Shivaprakash [25], during statistical analysis, found a significant inverse association between mandibular crowding and effective mandibular length (r=-0.290; p=0.025), pronounced direct correlations between maxillary and mandibular crowding (r=0.640; p=0.001) and between effective maxillary and mandibular lengths (r=0.555; p=0.001).

The obtained data are of great interest for practical orthodontics, as indicated by the results of clinical cases in which knowledge obtained in research is successfully applied [15, 17, 20, 27].

Conclusion

1. In young men and young women with physiological occlusion and a wide facial type, all 18 possible significant ($p<0.001$) models of the linear dimensions of dental arches were built depending on the characteristics of Burstone cephalometric indicators and computed tomography tooth dimensions (in young men R^2= from 0.829 to 0.980; in young women R^2= from 0.680 to 0.962).

2. When analyzing the frequency of inclusion of Burstone cephalometric indicators and computed tomography tooth dimensions in the models, the most frequently included variables in young men were cephalometric indicators (23.70 %), the width of the crown part of the corresponding teeth in the mesiodistal plane (20.74 %), and the width of the crown part of the corresponding teeth in the vestibulo-oral plane (17.04 %); whereas in young women – cephalometric indicators (27.21 %), the width of the crown part of the corresponding teeth in the mesiodistal plane (13.24 %), the width of the crown part of the corresponding teeth in the vestibulo-oral plane (11.03 %), and the width of the cervical part of the corresponding teeth in the vestibulo-oral plane (10.29 %).

3. When analyzing the frequency of inclusion of the corresponding teeth in the models, the most frequently included in young men were maxillary lateral incisors and canines (13.59 % each), maxillary central incisors (11.65 %), and mandibular canines (10.68 %); whereas in young women – maxillary central incisors (23.23 %), mandibular canines (14.14 %), mandibular lateral incisors (13.13 %), maxillary lateral incisors (12.12 %), mandibular central incisors (11.11 %), and maxillary canines (10.10 %).

References

[1] Aktürk, E. S., Müftüoğlu, Ö., & Memikoğlu, T. U. T. (2022). Anterior Tooth Size Discrepancy in Class III Surgical Patients. T*urkish Journal of Orthodontics, 35*(3), 186-191. doi: 10.5152/TurkJOrthod.2022.21202

[2] Alt, K. W., Honrath, N., Weykamp, M., Grönebaum, P., Nicklisch, N., & Vach, W. (2024). The correlation of tooth sizes and jaw dimensions with biological sex and stature in a contemporary central European population. *Biology, 13*(8), 569. doi: 10.3390/biology13080569

[3] Atasever İşler, A. A., Hezenci, Y., & Bulut, M. (2025). Prevalence of orthodontic malocclusion in children aged 10–12: an epidemiological study. *BMC Oral Health, 25*(1), 249. doi: 10.1186/s12903-025-05650-x

[4] Brotskyi, N. O. (2025). Correlations between Ricketts "internal structure" cephalometric parameters and tooth and dental arch dimensions in Ukrainian young men and women with physiological occlusion, with and without consideration of facial type. *Вісник Вінницького національного медичного університету=Reports of Vinnytsia National Medical University, 29*(4), 572-580. doi: 10.31393/reports-vnmedical-2025-29(4)-03

[5] Brotskyi, N. O., Dmitriev, M. O., Arshynnikov, R. S., Drachuk, N. V., Popova, O. I., Moskalenko, V. B., & Ruban, M. M. (2024). Models of linear dimensions necessary for constructing the correct shape of the dental arch in boys and girls with a wide face type depending on the characteristics of teleradiometric indicators. *Вісник Вінницького національного медичного університету=Reports of Vinnytsia National Medical University, 28*(4), 613-619. doi: 10.31393/reports-vnmedical-2024-28(4)-06

[6] Brotskyi, N. O., Dmitriev, M. O., Beliaiev, E. V., Piliponova, V. V., & Kyrychenko, I. M. (2025). Correlations of teleradiometric "dental" indicators according to the Ricketts method with the sizes of teeth and dental arches in Ukrainian young men and young women with physiological occlusion without and taking into account the type of face. *Вісник Вінницького національного медичного університету=Reports of Vinnytsia National Medical University, 29*(1), 19-28. doi: 10.31393/reports-vnmedical-2025-29(1)-03

[7] Burstone, C. J., James, R. B., Legan, H., Murphy, G. A., & Norton, L. A. (1979). Cephalometrics for orthognathic surgery. *J Oral Surg*, (36), 269-277. PMID: 273073

[8] Chen, H., Lin, L., Chen, J., & Huang, F. (2024, July). Prevalence of malocclusion traits in primary dentition, 2010-2024: a systematic review. In *Healthcare* (Vol. 12, No. 13, p. 1321). MDPI. doi: 10.3390/healthcare12131321

[9] Daoud, R., Bencze, M. A., Albu, C. C., Teodorescu, E., Dragomirescu, A. O., Vasilache, A., ... & Ionescu, E. (2021). Implications of permanent teeth dimensions and arch lengths on dental crowding during the mixed dentition period. *Applied Sciences, 11*(17), 8004. doi: 10.3390/app11178004

[10] Devanna, R., Felemban, N. H., Althomali, Y., Battepati, P. M., Alfawzan, A. A., & Gupta, P. (2021). Prevalence of malocclusion among children of the Kingdom of Saudi Arabia–A systematic review and meta-analysis. *The Saudi Dental Journal, 33*(8), 826-834. doi: 10.1016/j.sdentj.2021.09.005

[11] Elhiny, O. A., Sharaf, R. F., Abou Elyazied, M., Radwan, E., & Salem, G. A. (2021). The relationship between tooth size, arch length and arch perimeter in Egyptians. *Bali Medical Journal, 10*(3), 1056-1060. doi: 10.15562/bmj.v10i3.2618

[12] Ferro, R., Besostri, A., Olivieri, A., Quinzi, V., & Scibetta, D. (2016). Prevalence of cross-bite in a sample of Italian preschoolers. *Eur J Paediatr Dent, 17*(1), 307-309. PMID: 28045319

[13] García-Gil, M., Alarcón, J. A., Cacho, A., Yañez-Vico, R., Palma-Fernández, J. C., & Martin, C. (2023). Association between eruption sequence of posterior teeth, dental crowding, arch dimensions, incisor inclination, and skeletal growth pattern. *Children, 10*(4), 674. doi: 10.3390/children10040674

[14] Kareem, F. A., Rauf, A. M., Noori, A. J., & Ali Mahmood, T. M. (2020). Prediction of the dental arch perimeter in a Kurdish sample in Sulaimani City based on other linear dental arch measurements as a malocclusion preventive measure. *Computational and Mathematical Methods in Medicine, 2020*(1), 8869996. doi: 10.1155/2020/8869996

[15] Kochar, G. D. (2021). Management of Tooth Size Arch Perimeter Discrepancy: An Indian Board of Orthodontics Case Report. J*ournal of Indian Orthodontic Society, 55*(3), 310-314. doi: 10.1177/03015742211026217

[16] Krooks, L., Pirttiniemi, P., Kanavakis, G., & Lähdesmäki, R. (2016). Prevalence of malocclusion traits and orthodontic treatment in a Finnish adult population. *Acta Odontologica Scandinavica, 74*(5), 362-367. doi: 10.3109/00016357.2016.1151547

[17] Lim, H. J., Kim, Y., Park, J. H., Lee, N. K., Kim, K. B., & Kook, Y. A. (2022). Cephalometric and model evaluations after molar distalization using modified C-palatal plates in patients with severe arch length discrepancy. *American Journal of Orthodontics and Dentofacial Orthopedics, 162*(6), 870-880. doi: 10.1016/j.ajodo.2021.07.024

[18] Londono, J., Ghasemi, S., Moghaddasi, N., Baninajarian, H., Fahimipour, A., Hashemi, S., ... & Dashti, M. (2023). Prevalence of malocclusion in Turkish children and adolescents: A systematic review and meta-analysis. *Clinical and experimental dental research, 9*(4), 689-700. doi: 10.1002/cre2.771

[19] Marchenko, A. V., Gunas, I. V., Petrushanko, T. O., Serebrennikova, O. A., & Trofimenko, Yu. Yu. (2017). Computer-tomographic characteristics of root length incisors and canines of the upper and lower jaws in boys and girls with different craniotypes and physiological bite. *Wiadomosci Lekarskie (Warsaw, Poland: 1960), 70*(3 pt 1), 499-502. PMID: 28711896

[20] Nugraha, A. P., Putri, D. A., Salim, A., Narmada, I. B., Triwardhani, A., Ardani, I. G. A. W., ... & Pramusita, A. (2025). Arch Length Discrepancy Analysis Comparison with the Huckaba and Moyers Method in Angle Class I Malocclusion in Surabayan Children with Mixed Dentition during the Growth and Development Phase: A Retrospective Cross-Sectional Study in Universitas Airlangga Dental Hospital. *European Journal of Dentistry*. Online ahead of print. doi: 10.1055/s-0045-1807732

[21] Omar, H., Alhajrasi, M., Felemban, N., & Hassan, A. (2018). Dental arch dimensions, form and tooth size ratio among a Saudi sample. *Saudi medical journal, 39*(1), 86-91. doi: 10.15537/smj.2018.1.21035

[22] Price, J., Whittaker, W., Birch, S., Brocklehurst, P., & Tickle, M. (2017). Socioeconomic disparities in orthodontic treatment outcomes and expenditure on orthodontics in England's state-funded National Health Service: a retrospective observational study. *BMC Oral Health, 17*(1), 123. doi: 10.1186/s12903-017-0414-1

[23] Ryabov, T. V., Shinkaruk-Dykovytska, M. M., Kotsyura, O. O., Koliadenko, S. V., Belik, N. V., Piliponova, V. V., & Gunas, I. V. (2024). Correlations of teleroentgenometric indicators according to the Steiner method with the dimensions of teeth and dental arches in young men and young women with a physiological bite without taking into account the type of face. *Вісник Вінницького національного медичного університету=Reports of Vinnytsia National Medical University, 28*(3), 410-419. doi: 10.31393/reports-vnmedical-2024-28(3)-07

[24] Schneider-Moser, U. E., & Moser, L. (2022). Very early orthodontic treatment: when, why and how?. *Dental press journal of orthodontics, 27*, e22spe2. doi: 10.1590/2177-6709.27.2.e22spe2

[25] Singh, S., & Shivaprakash, G. (2017). To evaluate the correlation between skeletal and dental parameters to the amount of crowding in class II div. 1 malocclusions. *Journal of clinical and diagnostic research: JCDR, 11*(9), ZC22-ZC27. doi: 10.7860/JCDR/2017/27675.10566

[26] Vithanaarachchi, S. N., & Nawarathna, L. S. (2017). Prevalence of anterior cross bite in preadolescent orthodontic patients attending an orthodontic clinic. *Ceylon Medical Journal, 62*(3), 189-192. doi: 10.4038/cmj.v62i3.8523

[27] Volovic, J., Badirli, S., Ahmad, S., Leavitt, L., Mason, T., Bhamidipalli, S. S., ... & Turkkahraman, H. (2023). A novel machine learning model for predicting orthodontic treatment duration. *Diagnostics, 13*(17), 2740. doi: 10.3390/diagnostics13172740

[28] Vu, D. A., Vu, H. M., Nguyen, Q. T., & Vu, H. M. (2024). Malocclusion among children in Vietnam: Prevalence and associations with different habits. *Journal of oral biology and craniofacial research, 14*(2), 112-115. doi: 10.1016/j.jobcr.2024.01.007

[29] Yao, J., Li, D. D., Yang, Y. Q., McGrath, C. P. J., & Mattheos, N. (2016). What are patients' expectations of orthodontic treatment: a systematic review. *BMC oral health, 16*(1), 19. doi: 10.1186/s12903-016-0182-3

[30] Zhou, X., Zhang, Y., Wang, Y., Zhang, H., Chen, L., & Liu, Y. (2017). Prevalence of malocclusion in 3-to 5-year-old children in Shanghai, China. *International journal of environmental research and public health, 14*(3), 328. doi: 10.3390/ijerph14030328

МОДЕЛЮВАННЯ ЛІНІЙНИХ РОЗМІРІВ ЗУБНИХ ДУГ В УКРАЇНСЬКИХ ЮНАКІВ І ДІВЧАТ ІЗ ФІЗІОЛОГІЧНИМ ПРИКУСОМ І ШИРОКИМ ТИПОМ ОБЛИЧЧЯ В ЗАЛЕЖНОСТІ ВІД ОСОБЛИВОСТЕЙ ТЕЛЕРЕНТГЕНОГРАФІЧНИХ ПОКАЗНИКІВ ЗА МЕТОДОМ BURSTONE ТА КОМП'ЮТЕРНО-ТОМОГРАФІЧНИХ РОЗМІРІВ ЗУБІВ

Орловський І. В., Беляєв Е. В., Юр А. М., Закалата Т. Р., Ісакова Н. М., Ромашкіна О. А., Рубан М. М.

Варіабельність лінійних параметрів зубних дуг може бути зумовлена краніофаціальними особливостями та розмірами зубів. Проведення дослідження, що дозволить точніше описати взаємодію, тобто, взаємозв'язки цих трьох структур у межах специфічної популяції, дозволить підвищити обґрунтованість ортодонтичної діагностики та лікування. Вибір телерентгенометричних показників за Burstone є найбільш доцільним, зважаючи на малочисельність досліджень з використанням цього аналізу на українській популяції. Мета дослідження – розробка та аналіз регресійних моделей лінійних розмірів зубних дуг в українських юнаків і дівчат із фізіологічним прикусом із широким типом обличчя в залежності від особливостей телерентгенографічних показників за методом Burstone та комп'ютерно-томографічних розмірів зубів. На первинних комп'ютерних томограмах та телерентгенограмах 25 українських юнаків і 25 дівчат із фізіологічним прикусом і широким типом обличчя, що були отримані з банку даних науково-дослідного центру та кафедри стоматології дитячого віку Вінницького національного медичного університету ім. М. І. Пирогова, проведено вимірювання лінійних і кутових показників за методом Burstone та розмірів зубів і зубних дуг. Регресійні моделі розмірів зубних дуг в залежності від телерентгенометричних показників і комп'ютерно-томографічних розмірів зубів побудовані за допомогою ліцензійного пакету «Statistica 6.0». Встановлено, що в юнаків і дівчат із фізіологічним прикусом і широким типом обличчя побудовані усі 18 можливих достовірних моделей лінійних параметрів необхідних для побудови коректної форми зубних дуг в залежності від особливостей телерентгенометричних показників за методом Burstone та комп'ютерно-томографічних розмірів зубів із коефіцієнтом детермінації (R^2) більшим 0,6 (в юнаків R^2= від 0,829 до 0,980, $p<0,001$ в усіх випадках; дівчат R^2= від 0,680 до 0,962, $p<0,001$ в усіх випадках). Аналіз частоти входження до моделей комп'ютерно-томографічних розмірів зубів і телерентгенометричних показників за методом Burstone показав: в юнаків найбільш часто входять телерентгенометричні показники (23,70 %), ширина коронкової частини відповідних зубів у мезіо-дистальній площині (20,74 %) та ширина коронкової частини відповідних зубів у вестибуло-оральній площині (17,04 %); у дівчат найбільш часто входять телерентгенометричні показники (27,21 %), ширина коронкової частини відповідних зубів у мезіо-дистальній площині (13,24 %), ширина коронкової частини відповідних зубів у вестибуло-оральній площині (11,03 %) та ширина пришийкової частини відповідних зубів у вестибуло-оральній площині (10,29 %). Аналіз частоти входження до моделей відповідних зубів показав: в юнаків найбільш часто входять верхні бічні різці й ікла (по 13.59 %), верхні присередні різці (11,65 %) та нижні ікла (10,68 %); у дівчат найбільш часто входять верхні присередні різці (23,23 %), нижні ікла (14,14 %), нижні бічні різці (13,13 %), верхні бічні різці (12,12 %), нижні присередні різці (11,11 %) та верхні ікла (10,10 %).

Ключові слова: *стоматологія, цефалометрія за методом Burstone, комп'ютерно-томографічні розміри зубів і зубних дуг, юнаки та дівчата, тип обличчя, фізіологічний прикус, регресійний аналіз.*

Author's contribution

Orlovskyi I. V. – research, methodology and writing of the original draft, formal analysis.
Beliaiev E. V. – conceptualization, supervision.
Yur A. M. – review writing and editing.
Zakalata T. R. – review writing and editing.
Isakova N. M. – data visualization.
Romashkina O. A. – validation.
Ruban M. M. – software.

DOI: 10.31393/morphology-journal-2026-32(1)-09 Reports of Morphology, Vol. 32, №1, Pages 64-70

ISSN 1818-1295 eISSN 2616-6194

REPORTS OF MORPHOLOGY

Official Journal of the Scientific Society of Anatomists, Histologists, Embryologists and Topographic Anatomists of Ukraine

journal homepage: https://morphology-journal.com

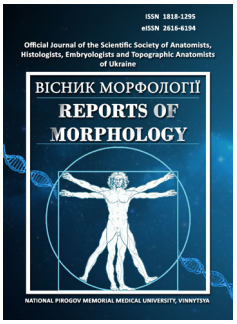

Morphological changes in the extraorgan vascular bed of the pineal gland of rats under conditions of chronic stress

Pshychenko V. V.[1,2], Cherno V. S.[1], Naidich O. V.[2], Bondar A. O.[2], Yulevych O. I.[2], Ovcharenko H. V.[3]

[1] Petro Mohyla Black Sea National University, Mykolaiv, Ukraine
[2] Mykolaiv National Agrarian University, Mykolaiv, Ukraine
[3] Odesa State Agrarian University, Odesa, Ukraine

ARTICLE INFO
Received: 19 August 2025
Accepted: 26 January 2026

UDC: 591.481.3

CORRESPONDING AUTHOR
e-mail: pshychenko85@gmail.com
Pshychenko V. V.

CONFLICT OF INTEREST
The authors have no conflicts of interest to declare.

FUNDING
This study was a part of the research project "Molecular-genetic and morphological features of reparative bone regeneration using functional-protective coatings of implant materials" with governmental funding, state number of registration 0119U101119.

DATA SHARING
Data are available upon reasonable request to corresponding author.

Modern Ukrainian society has been in conditions of active military operations for several years, which have caused disruption of sleep patterns, lack of proper rest, and a sense of security, which has led to a state of chronic stress. The main role in protecting the body from stress factors, regulating sleep, and implementing adaptive reactions belongs to the pineal gland and the hormone it synthesizes – melatonin. However, prolonged exposure to stress factors leads to disruption of the functional activity of the pineal gland, which manifests itself not only at the cellular level but also in the state of the vascular bed. The aim of the work was to study morphological changes in the state of the extraorgan vascular bed and rheological properties of the pineal gland blood under conditions of chronic stress. The study was conducted on 12 adult white male Wistar line rats, which were divided into control and experimental groups. Animals in the control group were kept under normal vivarium conditions without the influence of additional factors. Animals in the experimental group were subjected to chronic stress by forced swimming for 60 minutes a day for 10 days. To study the state of the vascular bed of the pineal gland, morphological, morphometric, and statistical research methods were used. During the study, morphological manifestations of extraorgan blood circulation disorders in the pineal gland were detected, manifested by changes in the rheological properties of the blood and the restructuring of the walls of venous and arterial blood vessels. It was established that violations of the rheological properties of blood in venous vessels were manifested by blood separation, aggregation and lysis of erythrocytes and stasis, and in arterial vessels – by the practically absence of erythrocytes in the lumen of the vessels. Morphological changes in the state of the vascular wall in the veins were manifested by endothelial cell hypertrophy, stretching and thinning of the vascular wall, and its ruptures. In arterial type vessels, hypertrophy and edema of endothelial cells and spasm of muscle cell membranes were detected. Thus, the detected morphological changes indicate impaired blood circulation and slowing of blood flow, which leads to hypoxia of the pineal gland parenchyma.

Keywords: *chronic stress, pineal gland, blood vessels, rheological properties of blood.*

Introduction

The conditions of the modern reality of Ukrainian society, which has been in conditions of active military operations for several years, are characterized by socio-economic difficulties and uncertainty of the situation, which undoubtedly affects the state of mental health of the population [9, 14]. In addition, all these factors, against the background of the sounds of explosions, sirens, sleep disturbances, lack of proper rest and a sense of security, cause a state of constant stress in all segments of the population [20, 22, 23]. It is known that chronic stress, in its various manifestations, remodels brain homeostasis, which negatively affects the psychological state, is accompanied by depressive disorders, cerebral circulation disorders, premature brain aging and atrophy, which ultimately leads to functional and morphological restructuring of all body systems, the development of various diseases, impaired cognitive functions and a decrease in the quality of life [26, 29]. The main role in protecting the body from stress factors, regulating sleep, and implementing

adaptive reactions belongs to the organ of the central neuroendocrine system – the pineal gland and the hormone it synthesizes – melatonin [6, 8]. It is known that melatonin has a wide spectrum of biological activity, is a universal adaptogen that has a protective effect on all organs under stress and slows down the development of pathological changes in the body [18, 19, 30]. Therefore, prolonged exposure to stress factors leads to pineal dysfunction, which is accompanied by a decrease in melatonin secretion, sleep disorders and neurological disorders [2, 7, 24].

In recent years, an increasing number of scientific publications have been devoted to the study of changes in the morpho-functional features of the pineal gland under the influence of pathological factors, including stress [21]. At the same time, there are few among them that consider and investigate the morphological manifestations of changes in the vascular bed and rheological properties of the blood of the pineal gland, which arise against the background of chronic stress and can lead to inhibition of the functional activity of the organ and psychoneurological disorders [12, 13].

Therefore, *the aim* of our study was to study morphological changes in the vascular bed and rheological properties of pineal gland blood under conditions of chronic stress.

Materials and methods

The results of this work are a fragment of the research topic of the Department of Morphology and Public Health of the Petro Mohyla Black Sea National University of the Ministry of Education and Science of Ukraine “The influence of environmentally hazardous factors on the mechanisms of development of civilization diseases and their correction with physiologically active substances”, state registration number 0124U002163.

All stages of the study, manipulative interventions and euthanasia of animals were carried out in compliance with the requirements and general principles of work with experimental animals in accordance with the following standards: Council of Europe Convention on Bioethics (1997); European Convention for the Protection of Vertebrate Animals Used for Experimental and Other Scientific Purposes, General Ethical Principles of Experiments on Animals, approved by the First National Congress of Ukraine on Bioethics (2001); Law of Ukraine “On the Protection of Animals from Cruelty” (2006) and other international treaties and current national legislation in the field of biomedical research. The study was conducted according to a protocol approved by the Bioethics Commission of the Petro Mohyla Black Sea National University (Protocol No. 4 dated June 24, 2024).

The experimental study involved 12 sexually mature laboratory rats of the Wistar line, weighing 200-220 g. The choice of males for the study was due to the absence of cyclic fluctuations in blood plasma melatonin levels compared to females, in which the content of this hormone, and therefore the morphological and functional state of the pineal gland, is determined by the phase of the ovarian cycle [16, 27].

The experimental animals were kept in standard vivarium conditions throughout the study and had free access to food and clean water. Artificial lighting sources were not used in the vivarium, since the pineal gland, which is the main source of endogenous melatonin, reacts to changes in light levels with morpho-functional restructuring, which is accompanied by fluctuations in the level of the hormone in the blood plasma [11, 15]. Therefore, the research was performed under natural lighting typical of the autumn-winter period.

To study the effect of chronic stress on the state of the vascular bed of the pineal gland, two groups of animals were formed: control and experimental. Each group included six rats, which is the minimum acceptable norm for the number of animals required for statistical research. The animals in the control group were kept in standard vivarium conditions and were not exposed to additional factors, since any, even minor, changes in maintenance or manipulation are a stressful factor for the animals and can cause morphological changes in the pineal gland, which is responsible for the start of the stress response and adaptation processes. The animals in the experimental group were simulated to experience chronic stress through forced swimming. For this purpose, the rats were placed in a tank with 10 liters of water for 1 hour. The water temperature was maintained within 28-30 °C, and the room temperature was 25 °C [3]. One-time training sessions were carried out for 10 days.

Rats from the control and experimental groups were removed from the experiment simultaneously, on the 1st day after the last forced swim, by performing a single-stage decapitation under thiopental anesthesia, which was administered intraperitoneally at a rate of 25 mg/kg of animal weight. After the decapitation procedure was completed, the animals’ skulls were scalped with subsequent removal of its vault along with the dura mater. Then the brain was separated together with the pia mater from the base of the skull and fixed in 10 % neutral formalin solution for 20 hours. After washing the fixed material and isolating the pineal gland, dehydration was carried out in alcohols of increasing concentration. Using standard methods, the obtained material was embedded in paraffin blocks, from which sections 5-6 μm thick were made on a semi-automatic rotary microtome “Microm” (Germany) and stained with hematoxylin and eosin in accordance with generally accepted methods. The obtained histological preparations of the pineal gland were studied and photographed at a magnification of ×10 binoculars, ×10, ×20, ×40 objective lenses of a microscope of the “Carl Zeiss” brand (Germany). Photo documentation of the research results was performed using a Canon digital camera.

To assess the morpho-functional state of the blood vessel wall of the pineal gland, the area of the endothelial cell nuclei was determined by measuring their large and small diameters. Morphometric measurements were performed using a screw-type ocular micrometer MOV 1-16 at an objective magnification of ×40.

Statistical calculations were performed on a personal computer using the “STATISTICA 10” software for computers

with the Windows operating system. The numerical data obtained during morphometric measurements were processed using standard statistical methods, calculating the arithmetic mean, standard error of the arithmetic mean, and standard square deviation. The results are presented as M±m. Student's t-test was used to assess the significance of differences between groups. The difference was considered significant when the numerical parameters between the control and experimental groups differed at a level of value not less than $p<0.05$.

Results

Histological studies of pineal gland preparations showed that in the control group of animals, extra-organ blood vessels had an intact appearance and uniform blood distribution. It was found that the walls of blood vessels were characterized by a typical three-layer structure and consisted of intima, media, and adventitia. The intima was represented by evenly spaced endothelial cells. The nuclei of endothelial cells were characterized by predominantly round shape. According to the results of morphometric measurements, it was found that the average area of the nuclei of endothelial cells of large-caliber venous vessels was 12.69±0.43 μm^2, and of arterial vessels – 18.06±0.52 μm^2. The middle layer of blood vessels consisted of layers of smooth muscle cells, the number of which depended on the caliber and type of vessel. As the diameter of the arteries increased, the number of muscle cell layers increased accordingly. The middle layer of venous vessels, in addition to smooth muscle cells, contained elastic fibers. The adventitia was formed by loose connective tissue. It should be noted that the walls of blood vessels of both arterial and venous types were not thickened and without ruptures (Fig. 1).

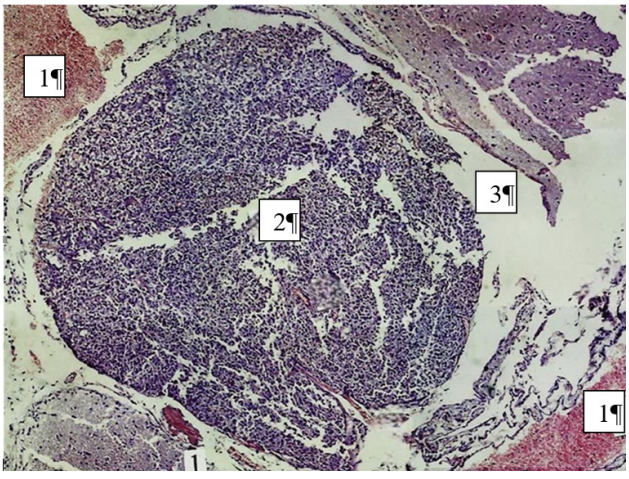

Fig. 1. Micrograph of the pineal gland of laboratory rats of the control group: 1 –extraorgan blood vessels; 2 – pineal gland; 3 – subarachnoid space. Staining: hematoxylin and eosin, ×100.

During microscopic examination of the preparations of rats of the experimental group, it was found that daily forced swimming for 10 days causes pathological changes in the blood vessels of the pineal gland, as an organ that plays a major role in ensuring the adaptation of the organism in response to the influence of stress factors, which leads to its morphological restructuring and changes in functional activity. Thus, during the light-optical study of extra-organ blood vessels, we detected morphological manifestations of changes in the structure of their walls and disturbances in the morphological manifestations of the rheological properties of blood.

In the lumen of large-diameter extra-organ veins, a fairly clear separation of blood into plasma and erythrocyte mass is noted. Moreover, it should be noted that the plasma component of the blood acquired a pronounced eosinophilic color and a homogeneous appearance, which may indicate coagulation of blood plasma proteins. Upon further examination of the erythrocyte mass, it was found that it was a conglomerate formed by single isolated erythrocytes with varying degrees of staining. Some erythrocytes were bright red, while others were pale pink. In some places in the studied conglomerate, clumps of adhered erythrocytes were found, the gaps between which were practically indistinguishable. In such vessels, adhered erythrocytes blocked the lumen of the venous vessel, which was accompanied by blood stasis. When examining extra-organ vessels of the venous type of small diameter, manifestations of erythrocyte aggregation were also detected. The wall of such blood vessels and endothelial cells underwent changes. Endothelial cells were arranged chaotically, which led to an increase in the distance between neighboring endothelial cells, thinning of the vascular wall, and the appearance of defects and ruptures, as a result of which blood plasma and single erythrocytes entered the extravascular space (Fig. 2). Ruptures of the vascular wall were also found in large diameter veins.

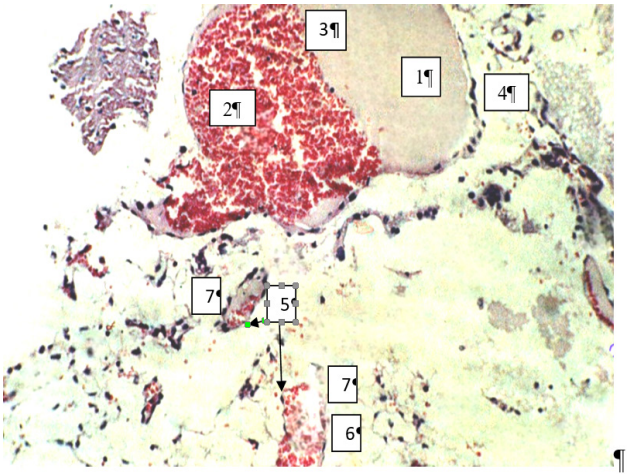

Fig. 2. Micrograph of extraorgan blood vessels of the pineal gland of venous type during chronic stress in rats: 1 – large diameter vein; 2 – erythrocyte mass; 3 – blood separation; 4 – vein wall; 5 – small diameter veins; 6 – nature of the distribution of blood elements in small veins; 7 – rupture of the venous vascular wall. Staining: hematoxylin and eosin, ×200.

In addition, in venous vessels, morphological manifestations of impaired rheological properties of blood

were detected, which were manifested by the phenomena of erythrocyte lysis, which appeared on histological preparations in the form of a pale pink homogeneous mass. It was established that such an erythrocyte mass occupied either the central zone of the blood vessel lumen or was closely adjacent to the vessel wall, which was in contact with the capsule of the pineal gland. It was found that the blood plasma in such vessels appeared transparent, indicating the absence of protein coagulation. It was found that the lumens of blood vessels in certain places had expansions of different sizes, formed exclusively in the wall that was not adjacent to the organ capsule. In such areas of the venous wall, its thickening and the reaction of the endothelial layer are noted, in the form of convergence of adjacent endothelial cells and an increase in the size of their nuclei (Fig. 3). Further histological examination revealed that the nuclei of endothelial cells of venous vessels acquired an oval shape, and their average area was 15.96±0.61 μm^2, which exceeded the control values by 25.77 % ($p<0.05$) and indicated edema and hypertrophy.

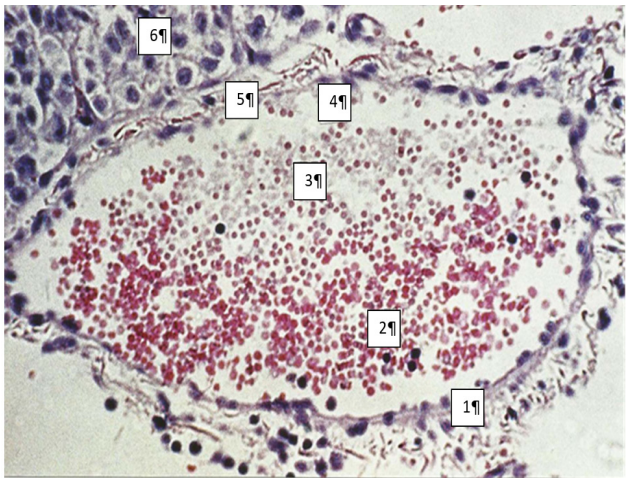

Fig. 3. Micrograph of a longitudinal section of a venous-type vessel adjacent to the pineal gland capsule of a rat under chronic stress: 1 – wall of an extraorgan vein; 2 – intact erythrocytes; 3 – lysis of erythrocytes; 4 – convergence of adjacent endothelial cells; 5 – pineal gland capsule; 6 – pineal gland parenchyma. Staining: hematoxylin and eosin, ×400.

When studying extra-organ vessels of the pineal gland of arterial type of different diameters, we also found signs of hemocirculatory disorders. It was found that the arterial vessels appeared ischemic. There were practically no erythrocytes in their lumens. Only single arterioles were filled with erythrocytes. It was found that the hemorrhage of arterial vessels on longitudinal sections was expressed over a significant area (Fig. 4).

It is also necessary to note morphological changes in the structures of the vascular wall of arterioles. The reaction of endothelial cells was primarily observed. They had an elongated shape, appeared hypertrophied with sharply enlarged dark nuclei filled with heterochromatin. It was found that the area of endothelial cell nuclei increased by 30.73 %

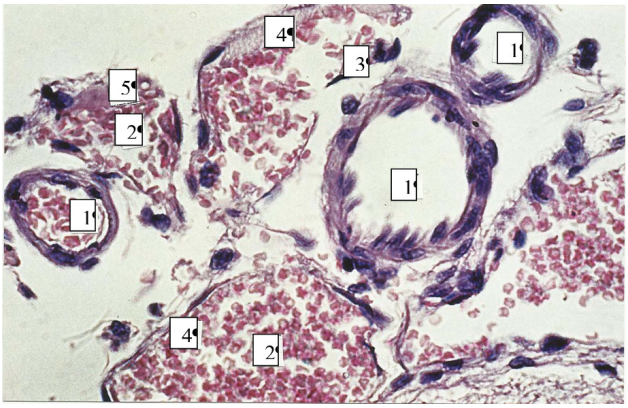

Fig. 4. Micrograph of extraorgan blood vessels of the pineal gland of rats under chronic stress: 1 – arteriole lumens; 2 – vein lumen; 3 – ruptures of the vein wall; 4 – erythrocyte adhesion; 5 – erythrocyte lysis in the parietal zone. Staining: hematoxylin and eosin, ×400.

($p<0.05$) compared to the control values and amounted to 23.61±0.82 μm^2. It was noted that the nuclei of endothelial cells protruded into the lumen of the blood vessel. Along with this, it is necessary to note changes in the muscular layer of the blood vessel wall. The smooth muscle elements of the media were in a state of spasm, which was accompanied by a decrease in the lumen of the vessel.

Discussion

The presented study was aimed at supplementing data on pathological changes in the vascular bed of the pineal gland and the rheological properties of blood in laboratory Wistar rats under conditions of chronic stress, since information on the state of the vascular bed in the domestic and foreign literary sources we have reviewed is sparse, which is due to both the small size of the gland and the complex topographic features of its location in the brain, which complicates atraumatic access to it [5, 10, 17]. In addition, there is no data in the literature on the state of endothelial cells of the pineal gland vessels, which play an important role in maintaining vascular wall tone and ensuring adaptation to hemodynamic changes [25, 28].

The morphological studies conducted showed that chronic stress simulated by forced swimming was accompanied in experimental animals by pronounced disorders of extra-organ blood circulation in the pineal gland, which were manifested both at the level of venous and arterial links. Thus, in the extra-organ venous bed we detected pathomorphological changes in the rheological properties of blood, manifested by blood separation, aggregation and lysis of erythrocytes and stasis, which indicates impaired blood circulation and slowing of blood flow [4, 12]. Disturbances in the rheological properties of blood led to morphological changes in the structure of the venous vessel wall, manifested by hypertrophy of endothelial cells, an increase in the distance between adjacent cells, stretching and thinning of the vascular wall and its ruptures, which contributed to the development of plasmorrhagia and

edema [12, 13].

Manifestations of chronic stress were also detected in extra-organ vessels of the arterial type and were manifested by the almost complete absence of erythrocytes in the lumens of the vessels, which indicates impaired oxygen transport, the development of hypoxia of pinealocytes and a decrease in the functional activity of the organ [12, 13]. Given the anatomical features of the pineal gland's location in the brain and its close connection with it, insufficient oxygen supply to the gland can lead to hypoxia, brain damage, and decreased brain function [1]. The impact of chronic stress was also accompanied by pathomorphological changes in the arterial vessel wall. It was found that the nuclei of endothelial cells were edematous, and as a result increased in size relative to the control group by 30.73 %. The nuclei of endothelial cells were dark because they were filled with functionally inactive heterochromatin, which stains well with basic dyes. Morphological changes in the muscular layer of the arterial wall, under conditions of chronic exposure to stress factors, were manifested by spasm and a decrease in the lumen of the corresponding vessel, which leads to impaired hemocirculation and ischemia.

Thus, the results obtained by us coincide with the results of scientific works of other researchers who studied the influence of chronic stress of various genesis on the state of the pineal gland and indicate that the prolonged exposure to stress factors is accompanied by pathological changes in the morphology of the wall of the blood vessels of the pineal gland, impaired rheological properties of blood and blood circulation, which leads to hypoxia of the organ parenchyma, changes in the structural and functional properties of pineal cells, their apoptosis, a decrease in the activity of the organ and disruption of adaptive processes [12, 13].

This experimental article differs from those published in this field in that it is the first to describe and analyze changes in the vascular bed of the pineal gland of laboratory Wistar rats under conditions of chronic stress caused by excessive physical exertion. The morphological analysis performed may be one of the criteria for assessing the functional state of the pineal gland under the influence of pathological factors in animals, which are most often used in experimental studies.

Conclusions

1. Chronic exposure to stress factors leads to pathomorphological changes in the condition of the walls of extra-organ blood vessels. In venous vessels, changes in the endothelium were detected, which were manifested by hypertrophy of endothelial cells, an increase in the distance between adjacent cells, stretching and thinning of the vascular wall and its ruptures, which contributed to the development of plasmorrhagia and edemaIn arterial type vessels, hypertrophy and edema of endothelial cells and spasm of muscle cells were detected, which was accompanied by a decrease in the lumen of the arterial vessel, which can lead to impaired blood outflow and ischemia of the pineal gland tissue.

2. Morphological changes in the rheological properties of blood in extra-organ venous vessels have been identified in the form of blood separation, aggregation and lysis of erythrocytes, and stasis, which indicates impaired blood circulation and slowing of blood flow.

3. In extra-organ vessels of the arterial type, manifestations of chronic stress were detected in the form of the practically absence of erythrocytes in the lumens, which indicates a violation of oxygen transport, the development of hypoxia of pinealocytes and a violation of the functional activity of the pineal gland.

References

[1] Adingupu, D. D., Soroush, A., Hansen, A., Twomey, R., & Dunn, J. F. (2023). Brain hypoxia, neurocognitive impairment, and quality of life in people post-COVID-19. *Journal of Neurology*, *270*(7), 3303-3314. doi: 10.1007/s00415-023-11767-2.

[2] Ahmad, S. B., Ali, A., Bila, M., Rashid, S. M., Wani, A. B., Bhat, R. R., & Rehman, M. U. (2023). Melatonin and Health: Insights of Melatonin Action, Biological Functions, and Associated Disorders. *Cellular and Molecular Neurobiology*, *43*(6), 2437-2458. doi: 10.1007/s10571-023-01324-w

[3] Alexa, A. I., Zamfir, C. L, Bogdănici, C. M., Oancea, A., Mașțaleru, A., Abdulan, I. M., … & Leon, M. M. (2023). The Impact of Chronic Stress on Behavior and Body Mass in New Animal Models. *Brain Sciences*, *13*(10), 1492. doi: 10.3390/brainsci13101492

[4] Barshtein, G., Zelig, O., Gural, A., Arbell, D., & Yedgar, S. (2022) Determination of red blood cell adhesion to vascular endothelial cells: A critical role for blood plasma. *Colloids Surf B Biointerfaces*, *210*, 112226. doi: 10.1016/j.colsurfb.2021.112226

[5] Bruno, F., Arrigoni, F., Maggialetti, N., Natella, R., Reginelli, A., Di Cesare E., … & Barile, A. (2019). Neuroimaging in emergency: a review of possible role of pineal gland disease. *Gland Surgery*, *8*(2), 133-140. doi: 10.21037/gs.2019.01.02

[6] Chen, J. Y., Li, T., Wang, J. L, Wang, Z. L, Zhang, Y., & Zang, L. Q. (2022). Protective Effects and Mechanisms of Melatonin on Stress Myocardial Injury in Rats. *Journal of Cardiovascular Pharmacology*, *80*(3), 417-429. doi: 10.1097/FJC.0000000000001312

[7] da Estrela, C., McGrath, J., Booij, L, & Gouin, J. P. (2021). Heart Rate Variability, Sleep Quality, and Depression in the Context of Chronic Stress. *Annals of Behavioral Medicine*, *55*(2), 155-164. doi: 10.1093/abm/kaaa039

[8] Favero, G., Bonomini, F., & Rezzani, R. (2021). Pineal Gland Tumors: A Review. *Cancers (Basel)*, *13*(7), 1547. doi: 10.3390/cancers13071547

[9] Fornaro, M., Ricci, C., Zotti, N., Caiazza, C., Viacava, L, Rubinshtain, Tal. A., … & de Bartolomeis, A. (2025). Mental health during the 2022 Russo-Ukrainian War: A scoping review and unmet needs. *Journal of Affective Disorders*, *373*, 12-27. doi: 10.1016/j.jad.2024.12.047

[10] Gallo, C. C., Nishino, F. A., do Amaral, F. G., & Cipolla-Neto, J. (2022). Pinealectomy in Rats. *Methods in molecular biology*, *2550*, 45-51. doi: 10.1007/978-1-0716-2593-4_7

[11] Giudice, A., Crispo, A., Grimaldi, M., Polo, A., Bimonte, S., Capunzo, M., … & Montella, M. (2018). The Effect of Light Exposure at Night (LAN) on Carcinogenesis via Decreased Nocturnal Melatonin Synthesis. *Molecules*, *23*(6), 1308.

doi: 10.3390/molecules23061308
[12] Hryntsova, N., Hodorová, I., Mikhaylik, J., & Romanyuk, A. (2022). A Response of the Pineal Gland in Sexually Mature Rats under Long-term Exposure to Heavy Metal Salts. *Prague Medical Report*, *123*(4), 225-242. doi: 10.14712/23362936.2022.21
[13] Hryntsova, N. (2022). Реадаптаційні перебудови епіфіза статевозрілих щурів після впливу на організм клітинного зневоднення [Readaptational adjustments of mature rat's epiphysis after influence on the cellular dehydration]. *Екологічні науки=Environmental Sciences*, *1*(40), 50-54. doi: 10.32846/2306-9716/2022.eco.1-40.9
[14] Limone, P., Toto, G. A., & Messina, G. (2022). Impact of the COVID-19 pandemic and the Russia-Ukraine war on stress and anxiety in students: A systematic review. *Frontiers in Psychiatry*, *13*, 1081013. doi: 10.3389/fpsyt.2022.1081013
[15] Lu, J., Zou, R., Yang, Y., Bai, X., Wei, W., Ding, R., & Hua, X. (2024). Association between nocturnal light exposure and melatonin in humans: a meta-analysis. *Environmental Science and Pollution Research*, *31*(3), 3425-3434. doi: 10.1007/s11356-023-31502-8
[16] Meers, J. M., & Nowakowski, S. (2020). Sleep, premenstrual mood disorder, and women's health. *Current Opinion in Psychology*, *34*, 43-49. doi: 10.1016/j.copsyc.2019.09.003
[17] Mohammadi, S., & Zahmatkesh, M. (2023). A surgical modification in the technique of rat pinealectomy. *Anatomical Science International*, *98*(2), 164-175. doi: 10.1007/s12565-022-00683-6
[18] Peruri, A., Morgan, A., D'Souza, A. A., Mellon, B., Hung, C. W., Kayal, G., … & Roballo, K. C. S. (2022). Pineal gland from the cell culture to animal models: a review. *Life (Basel)*, *12*(7), 1057. doi: 10.3390/life12071057
[19] Pishak, V. P., Kryvchanska, M. I., Riznichuk, M. O., Bulyk, O. R., & Lukan, Y. R. (2022). Мелатонін: біологічна роль та оптимізація його застосування [Melatonin: biological role and optimization of its application]. *Буковинський медичний вісник=Bukovinian Medical Herald*, *26*(2), 86-90 doi: 10.24061/2413-0737.XXVI.2.102.2022.16
[20] Pomortseva, S. P., & Deputatov, V. O. (2025). Стресостійкість як адаптаційний ресурс особистості в умовах воєнного стану [Resilience as an adaptive resource of personality in conditions of martial law]. *Габітус=Habitus*, *75*(2), 50-53. doi: 10.32782/hbts.75.2.7
[21] Shawky, H. A., Abdel Hafez, S. M. N., Hasan, N. A. K., Elbassuoni, E., Abdelbaky, F. A. F., & AboBakr, A. H. S. A. (2023). Changes in Rat Adrenal Cortex and Pineal Gland in Inverted Light–Dark Cycle: A Biochemical, Histological, and Immunohistochemical Study. *Microscopy and Microanalysis*, *29*(6), 2037-2052. doi: 10.1093/micmic/ozad101
[22] Shkodina, A. D., Zhyvotovska, A. I., & Boiko, D. I. (2022). Sleep and armed conflict: future complications of war in Ukraine. *Rev Neurol (Paris)*, *78*(9), 869-871. doi: 10.1016/j.neurol.2022.09.002
[23] Shuliakova, M., & Ratsyborynska-Polyakova, N. (2024). Вплив хронічного стресу на організм людини та роль психоедукації у редукції його психічних проявів [The impact of chronic stress on the human body and the role of psychoeducation in reducing its mental manifestations]. *Психосоматична медицина та загальна практика=Psychosomatic Medicine and General Practice*, *9*(1), 1-6. doi: 10.26766/pmgp.v9i1.490
[24] Song J. (2019). Pineal gland dysfunction in Alzheimer's disease: relationship with the immune-pineal axis, sleep disturbance, and neurogenesis. *Molecular Neurodegeneration*, *14*(1), 28. doi: 10.1186/s13024-019-0330-8
[25] Sukriti, S., Tauseef, M., Yazbeck, P., & Mehta, D. (2014) Mechanisms regulating endothelial permeability. *Pulmonary circulation*, *4*(4), 535-551. doi: 10.1086/677356
[26] Vakulenko, L. O., Prokopiv, M. M., & Haystruk, N. A. (2024). Передчасне старіння головного мозку як наслідок хронічного стресу [Premature aging of the brain as a consequence of chronic stress]. *Український неврологічний журнал=Ukrainian Neurological Journal*, *4*, 60-63. doi: 10.30978/UNJ2024-4-60
[27] Vidafar, P., & Spitschan, M. (2023). Light on Shedding: A Review of Sex and Menstrual Cycle Differences in the Physiological Effects of Light in Humans. *Journal of Biological Rhythms*, *38*(1), 15-33. doi: 10.1177/07487304221126785
[28] Viunitska, L. V., Gavrilenko, T. I., Pidgaina, O. A., Lomakovskyi, O. M., Rasputniak, O. V., & Zavadetska, O. P. (2023). Дисфункція ендотелію при стресі [Endothelial dysfunction under stress]. *Український ревматологічний журнал=Ukrainian journal of rheumatology*, *94*(4), 52-60. doi: 10.32471/rheumatology.2707-6970.94.18340
[29] Yang, L., Guo, C., Zheng, Z., Dong, Y., Xie, Q., Lv, Z., … & Cui, Y. (2025). Stress dynamically modulates neuronal autophagy to gate depression onset. *Nature*, *641*(8062), 427-437. doi: 10.1038/s41586-025-08807-4
[30] Zhang, H., Wei, M., Sun, N., Wang, H., & Fan, H. (2022). Melatonin attenuates chronic stress-induced hippocampal inflammatory response and apoptosis by inhibiting ADAM17/TNF-α axis. *Food and Chemical Toxicology*, *169*, 113441. doi: 10.1016/j.fct.2022.113441

МОРФОЛОГІЧНІ ЗМІНИ ЕКСТРАОРГАННОГО СУДИННОГО РУСЛА ШИШКОПОДІБНОЇ ЗАЛОЗИ ЩУРІВ ЗА УМОВ ХРОНІЧНОГО СТРЕСУ

Пшиченко В. В., Черно В. С., Найдіч О. В., Бондар А. О., Юлевич О. І. Овчаренко Г. В.

Сучасне українське суспільство вже декілька років перебуває в умовах активних військових дій, які стали причиною порушення режиму сну, відсутності повноцінного відпочинку та почуття безпеки, що спричинило стан хронічного стресу. Головна роль у захисті організму від стресових факторів, регуляції сну та здійсненні адаптаційних реакцій належить шишкоподібній залозі та гормону, який вона синтезує – мелатоніну. Однак, тривалий вплив стресових факторів призводить до порушення функціональної активності шишкоподібної залози, що проявляється не тільки на клітинному рівні, а і на стані судинного русла. Метою роботи було вивчення морфологічних змін стану екстраорганного судинного русла та реологічних властивостей крові шишкоподібної залози за умов хронічного стресу. Дослідження проводилося на 12 дорослих білих щурах-самцях лінії Вістар, які були розподілені на контрольну і дослідну групи. Тварини контрольної групи перебували за звичайних умов віварію без впливу додаткових факторів. Тваринам дослідної групи моделювали хронічний стрес шляхом примусового плавання по 60 хвилин на добу впродовж 10 діб. Для дослідження стану судинного русла шишкоподібної залози використовували морфологічні, морфометричні та статистичні методи

дослідження. В ході проведення дослідження були виявлені морфологічні прояви порушення екстраорганного кровообігу у шишкоподібній залозі, що виявлялися змінами реологічних властивостей крові та перебудовою стінок кровоносних судин венозного і артеріального типу. Встановлено, що порушення реологічних властивостей крові у судинах венозного типу проявлялися сепарацією крові, агрегацією і лізисом еритроцитів та стазом, а у судинах артеріального типу – практичною відсутністю еритроцитів у просвітах судин. Морфологічні зміни стану судинної стінки у венах проявлялися гіпертрофією ендотеліоцитів, розтягуванням і потоншенням судинної стінки та її розривами. У судинах артеріального типу виявлена гіпертрофія і набряк клітин ендотелію та спазм клітин м'язової оболонки. Таким чином, виявлені морфологічні зміни свідчать про порушення циркуляції крові та уповільнення кровотоку, що призводить до гіпоксії паренхіми шишкоподібної залози.

Ключові слова: *хронічний стрес, шишкоподібна залоза, кровоносні судини, реологічні властивості крові.*

Author's contribution
Pshychenko V. V. – data visualization, methodology and original project writing.
Cherno V. S. – conceptualization, formal analysis, and validation.
Naidich O. V. – administration of the project.
Bondar A. O. – research, software.
Yulevych O. I. – writing and editing a review.
Ovcharenko H. V. – resource.

DOI: 10.31393/morphology-journal-2026-33(1)-10 Reports of Morphology, Vol. 32, №1, Pages 71-78

ISSN 1818-1295 eISSN 2616-6194

REPORTS OF MORPHOLOGY

Official Journal of the Scientific Society of Anatomists, Histologists, Embryologists and Topographic Anatomists of Ukraine

journal homepage: https://morphology-journal.com

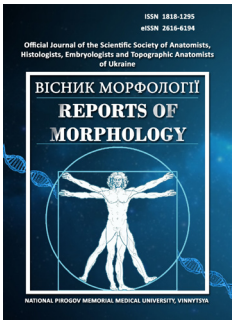

Morphological analysis of dry adult mandible as an initial approach in sex determination

Prasetiowati L.[1,2], Sakina S.[1], Dewi R. K.[2,3]

[1] Department of Anatomy, Histology and Pharmacology, Faculty of Medicine, University Airlangga, Surabaya, Indonesia

[2] Faculty of Health, Medicine and Natural Sciences (FIKKIA), University Airlangga, Banyuwangi, Indonesia

[3] Department of Forensic Medicine and Medicolegal, Faculty of Medicine, University Airlangga, Surabaya, Indonesia

ARTICLE INFO

Received: 10 August 2025

Accepted: 29 January 2026

UDC: 611.716-091:340.6-055.1/-055.2

CORRESPONDING AUTHOR

e-mail: lucky-p@fk.unair.ac.id

Prasetiowati L.

CONFLICT OF INTEREST

The authors have no conflicts of interest to declare.

FUNDING

The financial support for this study was provided by an internal basic research grant (PDU) from Universitas Airlangga, Indonesia.

DATA SHARING

Data are available upon reasonable request to corresponding author.

Sex determination from skeletal remains is a crucial step in forensic identification, particularly in cases involving incomplete or fragmented remains such as those encountered in mass disasters. Among skeletal elements, the mandible is frequently preserved due to its high resistance to environmental damage. The mandible is the largest and the most robust bone of the facial skeleton. It provides attachment for major masticatory muscles. Mandible also displays distinct morphological traits that are valuable for sex determination. Several non-metric mandibular features have been reported to demonstrate sexual dimorphism. However, the predictive accuracy of these traits varies considerably among different populations due to genetic, functional, and environmental influences. Moreover, studies investigating non-metric mandibular characteristics in the Indonesian population remain limited. Therefore, this study aimed to analyse nonmetric mandibular characteristics in adult Indonesian individuals and evaluated their effectiveness for sex determination. A cross-sectional study was conducted on mandibles of 49 adult (30 males and 19 females) from an Indonesian population. Eight non-metric parameters were observed, including chin shape, chin profile, mandibular ramus shape, mandibular ramus profile, posterior mandibular ramus flexure, gonial angle divergence, muscle marking, and the presence of antegonial notch. Statistical analysis was performed using appropriate software, SPSS version 22.0. The frequency of occurrence of each variable was calculated. Sexual differences were analysed using the Chi-square test and the significance level was set at $p<0.05$. Then, discriminant function analysis was performed to assess the combined predictive accuracy of the significant traits. As a result, four morphological traits demonstrated significant sexual dimorphism, including chin shape ($p<0.05$), posterior mandibular ramus flexure ($p<0.001$), gonial angle divergence($p<0.001$), and muscle markings ($p<0.001$). Based on the discriminant function analysis, the accuracy of prediction for sex determination was 86.7 % in males and 78.9 %, in female, with the overall total predictive accuracy was 83.7 %. The obtained data emphasize that several nonmetric morphological mandibular traits include chin shape, posterior mandibular ramus flexure, gonial angle divergence, and muscle markings, demonstrate marked sexual dimorphism and can therefore serve as an initial approach for sex determination in Indonesian population. The combined assessment of multiple non-metric features improves predictive accuracy and offers a practical screening tool in forensic context, particularly when skeletal remains are incomplete or fragmented.

Keywords: *forensic anthropology, human rights, mandible, non-metric morphology, sexual dimorphism.*

Introduction

The identification of victims from skeletal remains is essential in cases of mass fatalities, including accidents, explosions, and natural disasters. Under such circumstances, forensic investigations are often limited to incomplete or fragmented skeletal remains. Skeletal identification represents a major challenge in forensic medicine and

requires multidisciplinary expertise encompassing anatomy, radiology, archaeology, dentistry, and related fields. This process is fundamental for subsequent investigations aimed at establishing key biological profiles, including sex, age, stature, and ancestry. Among these parameters, sex determination constitutes the primary and most critical step, as the accurate estimation of age and stature is dependent on sex-specific characteristics [1].

Sex determination from skeletal remains can achieve an accuracy of up to 100 % when the entire skeleton is available [18]. The accuracy decreases to approximately 95 % when only the pelvic bones are examined, 92 % when analysis is limited to the cranium, and increases to 98 % when both the pelvis and cranium are assessed together [18]. In cases where a complete cranium is unavailable, the mandible serves as an essential source for sex determination. Its high resistance to bacterial degradation, extreme heat, and other environmental insults makes it one of the skeletal elements most likely to be preserved and suitable for analysis [5].

The mandible is the largest and strongest skull bone that forms the lower third of face. It has a curved body anteriorly, while posteriorly it extends into two rami that bears the coronoid and condylar processes [10]. Each condylar process articulates with temporal fossa to form the temporomandibular joint, that enables mandibular movement, essential for chewing and digestion. The mandible is the attachment site of masticatory muscles, including the masseter, temporalis, lateral pterygoid and medial pterygoid muscles [26]. Variations in geographical origin and dietary habits influence the shape of the mandible, consequently its morphological characteristics vary among different ethnic groups [9].

Sex determination from the mandible can be performed through metric and non-metric approaches. There have been many attempts to establish metric method for the determination of the mandibles of males and females [7, 11, 20, 28]. However, it requires completed, well-preserved specimens and precise measurement tools. In contrast, non-metric analysis relies on morphological traits and offers practical advantages, as they can be applied rapidly, do not require specialized equipment, and remain applicable even in fragmented or incomplete mandibles.

Previous studies have demonstrated that several non-metric mandibular traits exhibit statistically significant sexual dimorphism, such as posterior mandibular ramus flexure, the shape of the chin, the shape of mandible base, antegonial notch, gonial angle, muscle marking, surface of mandible, and the shape of coronoid process [8, 13, 14, 15]. However, the reported predictive accuracy of these traits varies considerably across studies and populations. S. Shivaprakash and A. G. Vijaykumar [22]age, stature and ethnic background. The identification of human skeletal remains is considered an initial step in forensic investigations and is crucial for further analysis. Objective-Determination of sex by using mandibular ramus posterior flexure. Materials and methods-The study was conducted on 104 adult mandibles, which were obtained from the mandibles available in the department of anatomy, Kasturba Medical College, Mangalore and from the students of 1 st year MBBS. Results-Using Mandibular ramus posterior flexure, out of 104 mandibles, we could determined the morphological sex in 79 mandibles with 76% accuracy rate and sex was misclassified in 25 mandibles. In the present study, overall predictive of accuracy of (76% estimated sexual differences by analysing posterior mandibular ramus flexure, finding 80% accuracy for males and 71 % for females in Indian population. Another study in Jordanian population demonstrated that the posterior mandibular ramus flexure had more accurately diagnostic for female (94,6 %), than for male (47,6 %) [4]. V. Saini [19] evaluated four traits (chin shape, gonial flaring, shape of lower border, and muscular attachment) and reported that the roughness of muscular attachments was the most reliable indicator for sex estimation, achieving the highest classification accuracy of 83.59 %. Other authors analysed the combination of the chin shape, the presence of an antegonial notch, and divergence of the gonial angle and found that Thai male mandible were distinguishable from female counterpart with an approximate 70 % accuracy rate [12].

It is important to note that accuracy in determining sex is variable and the degree of sexual dimorphism in mandibles is different for each population. Therefore, this *study aimed* to assess selected nonmetric mandibular characteristics and evaluated their effectiveness for sex determination in adult Indonesian population.

Materials and methods

This was a cross-sectional study that involved 49 dried human mandibles, 30 males and 19 females, obtained from the Department of Anatomy Histology and Pharmacology, Faculty of Medicine, Universitas Airlangga, Surabaya, Indonesia. The availability of the identified dry mandible with known sex in the institutional collection limited the sample size. The study was approved by the Research Ethics Committee of Rumah Sakit Universitas Airlangga, and registration number is 103/KEP/2024. Mandibles with pathological conditions such as fractures or defects, broken condylar or coronoid processes, broken and damaged mandibular angles were excluded from the study [14].

When analysing the mandibles, the examiner did not know the sex of the mandible reported in the corresponding identification, making this a blind study. For sexual identification of mandibles, eight non-metric parameters were selected. The protocol derived from Deana N. F. and Alves N. [8] (modified) was carried out to observe these features:

- chin shape was analysed from anterior and inferior view: bilobate, square, or pointed (Fig. 1a – c);
- chin profile was analysed according to protrusion of the chin from lateral view: vertical or prominent (Fig. 1d – e);
- mandibular ramus shape was analysed at the midpoint of the ramus: pinched or wide (Fig. 2a – b);
- mandibular ramus profile was analysed according to the curvature of the ramus against the mandibular body:

vertical, slanted, or inverted (Fig. 2c – e);
- posterior mandibular ramus flexure: flexure or straight (Fig. 3a – b);
- gonial angle divergence was analysed by observing the angle curves inward or outward: everted, straight, or inverted (Fig. 3c – e);
- muscle marking was analysed according to the surface of the ramus: rough/more prominent or smooth (Fig. 4a – b);
- presence of antegonial notch at the inferior border of mandible: present or absent (Fig. 4c – d).

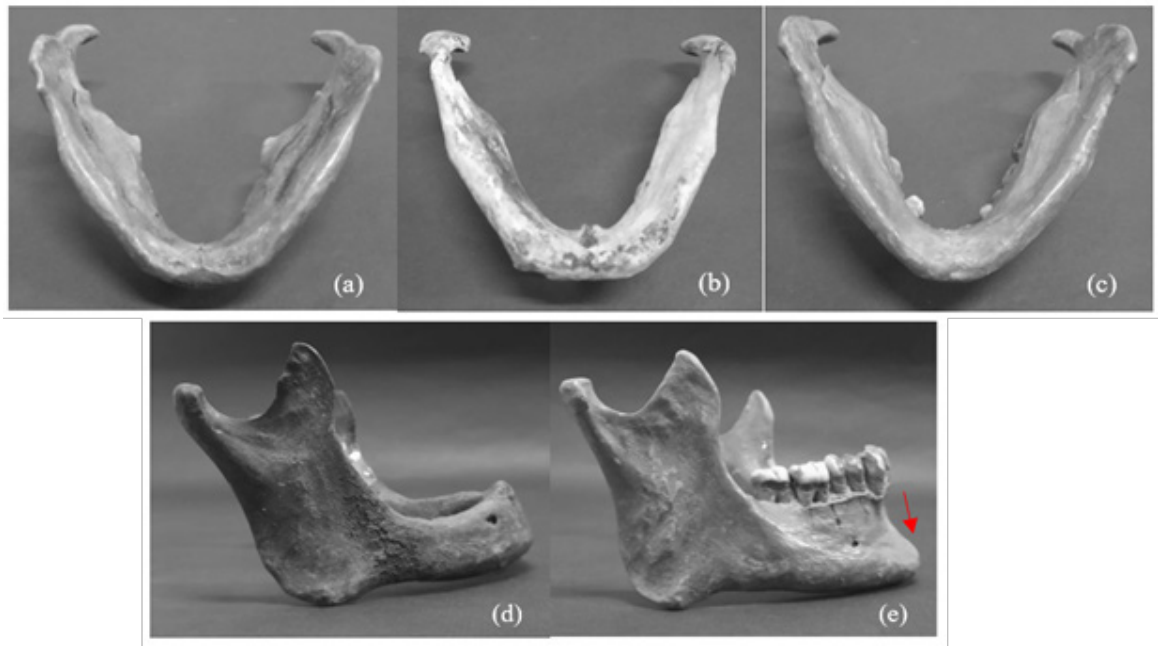

Fig. 1. Chin shape: (a) bilobate; (b) square; and (c) pointed. Chin profile: (d) vertical and (e) prominent (red arrow).

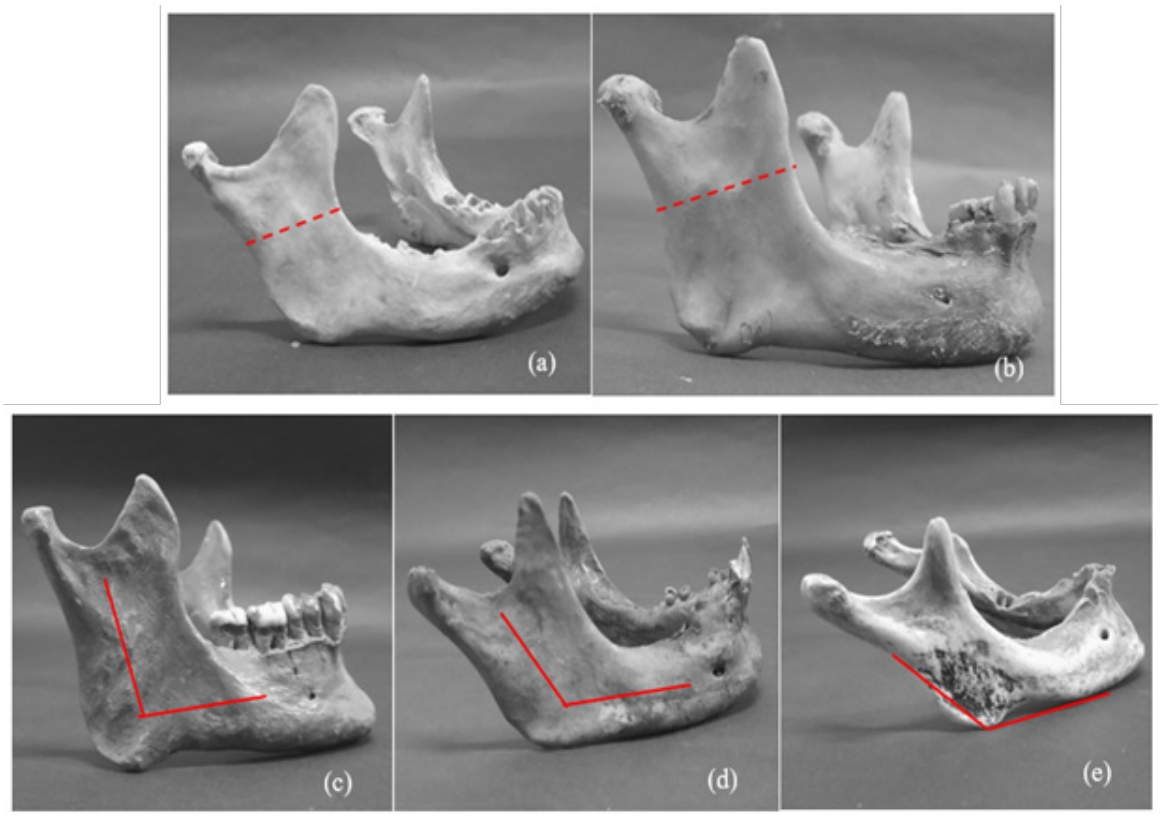

Fig. 2. Mandibular ramus shape: (a) pinched and (b) wide. Mandibular ramus profile: (c) vertical; (d) slanted; and (e) inverted.

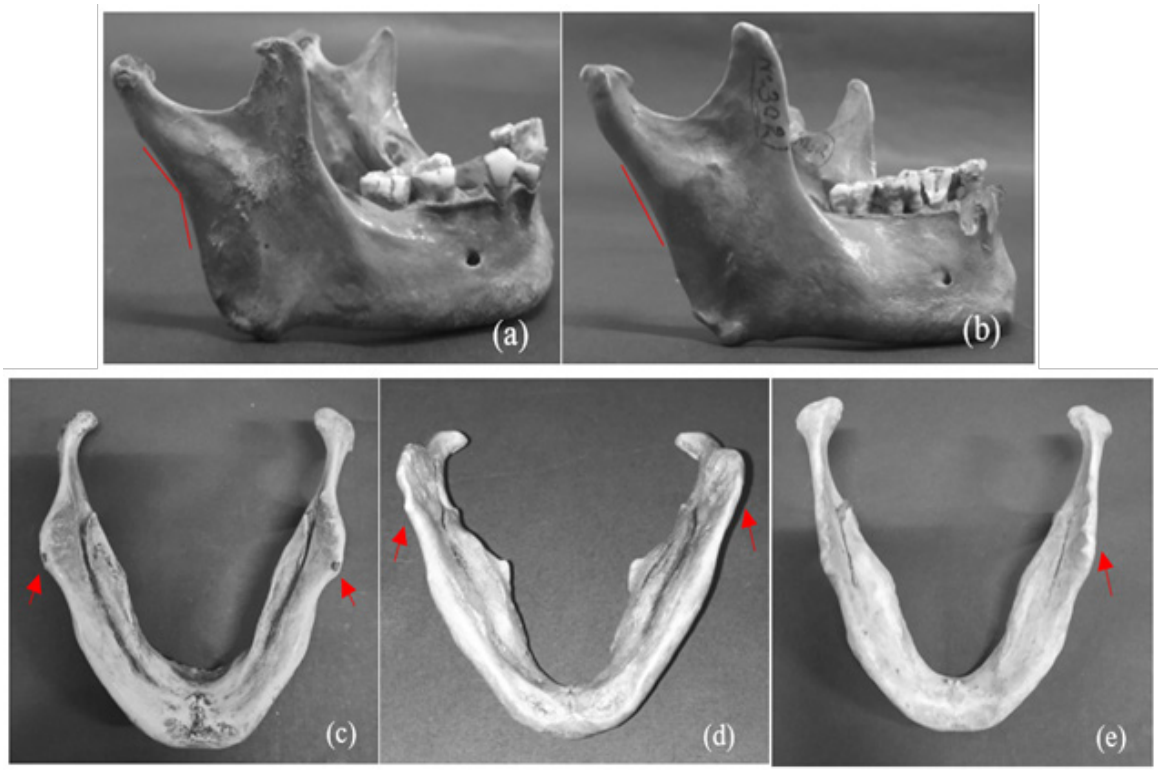

Fig. 3. Posterior mandibular ramus flexure: (a) flexure and (b) straight. Gonial angle divergence: (c) everted; (d) straight; and (e) inverted.

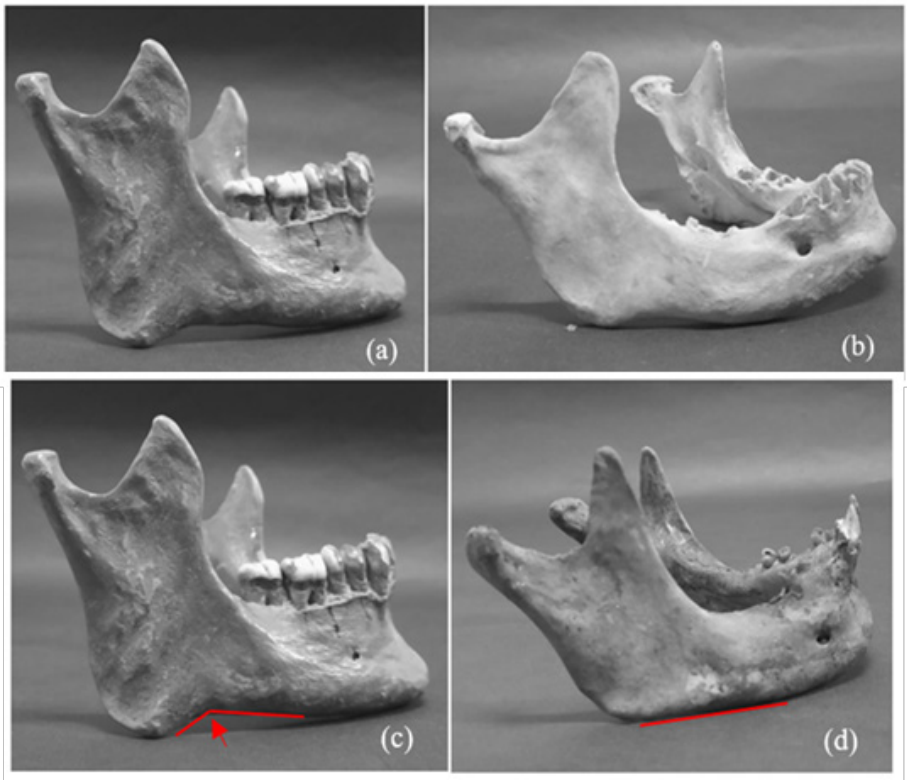

Fig. 4. Muscle marking: (a) rough/more prominent and (b) smooth. Presence of antegonial notch: (c) present and (d) absent.

For the statistical analysis, the data were analysed by the Pearson chi-square test and discriminant function analysis using SPSS program, version 22.0. Sex-specific predictive value/accuracy was calculated from the discriminant function classification table. The p-value <0.05 being considered statistically significant.

Results

According to chi-square test (see Table 1), the non-metric features that significantly differentiated sex were chin shape (p<0.05), posterior mandibular ramus flexure (p<0.001), gonial angle divergence (p<0.001), and muscle markings (p<0.001). The bilobate chin shape was found only in males, while females exhibited either a square or pointed chin shape. Most mandibles in males had flexures at the posterior border of the ramus (83.3 %) and more prominent or coarse muscle markings (83.3 %). Females exhibited a straight posterior border of the ramus (73.7 %) and finer muscle markings (78.9 %). The everted gonial angle type was predominant in males at 76.7 %, while females showed an inverted type (42.1 %).

Table 1. Comparison of non-metric parameter to differentiate the sex of the mandible.

Non-metric parameter n (%)		Males	Females	
		n (%)		
Chin shape	Bilobate	7 (23.3)	0	<0.05
	Square	17 (56.7)	9 (47.4)	
	Pointed	6 (20.0)	10 (52.6)	
Chin profile	Vertical	9 (30.0)	2 (10.5)	0.165
	Prominent	21 (70.0)	17 (89.5)	
Mandibular ramus shape	Pinched	18 (60.0)	13 (68.4)	0.771
	Wide	12 (40.0)	6 (31.6)	
Mandibular ramus profile	Vertical	11 (36.7)	3 (15.8)	0.229
	Slanted	15 (50.0)	14 (73.7)	
	Inverted	4 (13.3)	2 (10.5)	
Posterior mandibular ramus flexure	Flexure	25 (83.3)	5 (26.3)	<0.001
	Straight	5 (16.7)	14 (73.7)	
Gonial angle divergence	Everted	23 (76.7)	5 (26.3)	<0.001
	Straight	5 (16.7)	6 (31.6)	
	Inverted	2 (6.7)	8 (42.1)	
Muscle marking	Rough/more prominent	25(83.3)	4 (21.1)	<0.001
	Smooth	5 (16.7)	15 (78.9)	
Antegonial notch	Present	20 (66.7)	9 (47.4)	0.298
	Absent	10(33.3)	10 (52.6)	

The four non-metric parameters with significant differences were then analysed by employing the discriminant analysis. The predictive sex of the mandible is shown in Table 2. The male and female predictive value were 86.7 % and 78.9 %, respectively. The total predictive accuracy was 83.7 %.

Table 2. The predictive sex of the mandible using the discriminant function analysis.

True sex of the mandible	Predictive sex of the mandible	
	Male	Female
Male	26	4
Female	4	15

Discussion

The mandible is considered the most sexually dimorphic bone in the skull. Variations in the mandible traits among populations are influenced by environmental factors, growth patterns, developmental duration, and dietary habits, all of which are closely related to masticatory function [27]. The present study demonstrates that several non-metric mandibular traits exhibit significant sexual dimorphism and can be applied as an initial approach for sex determination in an Indonesian population. Among the eight non-metric traits evaluated, chin shape, posterior mandibular ramus flexure, gonial angle divergence, and muscle markings showed statistically significant differences between males and females. When these parameters were combined using discriminant function analysis, a high level of sex classification accuracy was achieved (86.7 % in males and 78.9 % in female), supporting the usefulness of non-metric mandibular assessment as a practical screening tool in forensic contexts.

The shape of the chin emerged as one of the most sexually dimorphic features. Our study reported that a bilobate chin configuration observed exclusively in male mandibles and square shape was shown by 56.7 % of males. Whereas female mandibles predominantly exhibited square or pointed chin shapes. Previous studies have identified chin shape as a trait in sex differentiation, with square chins more common in males and pointed chins more frequently observed in females [1, 6, 14]. Although the shape of the chin is more distinctive in males than in females, sex determination based solely on this trait is not sufficiently reliable. Nevertheless, its strong association with male sex underscore its usefulness as an initial morphological indicator.

In the present study, 83.3 % of males exhibited posterior mandibular ramus flexure, while 73.7 % of females presented a straight posterior border, suggesting that ramus flexure is predominantly a male trait. This result aligns with several previous studies suggesting that ramus flexure must be considered as one additional feature in sex determination [6, 22]. However, the reported accuracy rate of this trait varies among different population. D. H. Badran et al. [4] reported that ramus flexure higher predictive accuracy in female (94.6 %) than in male (47.6 %) within a Jordanian population, with an overall accuracy 70.9 %. Similarly, another in an Indian population reported a total accuracy of 61 % for this parameter [16]2014 to August, 2015 in various Medical

Colleges of the state of Odisha, India with the use of morbid anatomical specimen of mandibles and simple measuring instruments. The posterior ramus of adult mandibles were studied for presence or absence of any notching and if present its position in relation to occlusal plane. The study resulted, that there was a role of notch position in sex determination. The presence or absence of the notch though was not a consistent finding of all the mandibles. Males had frequent notching at the level of occlusal plane ($P< 0.01$.

The divergence of the gonial angle also showed a significant sex difference in this present study. An everted gonial angle more frequently observed in male (76.7 %) and inverted configurations predominating in females. Gonial eversion has been remain as a male trait in previous studies [1, 8, 12, 19, 23]. A study conducted by Shree B. et al. [23] demonstrated that 89 % males in a North Indian population had gonial eversion and 68 % females had inversion. Similarly, Saini V. [19] reported that gonial flare yielded an overall accuracy of 78.34 % for sex determination. N. F. Deana and N. Alves [8] also found that Black males in Brazilian population presented the everted more frequently than Black females with the sex accuracy up to 93 % in Black males.

In the present study, the muscle markings on the mandibles surface were significantly more prominent in male than female. Several previous studies have reported similar observations [12, 24, 25]. Study by Alias A. et al. [1] using postmortem computed tomography data in Malaysia, showed that man was significantly association with prominent muscle marking (85 %), whereas women had less prominent muscle marking (90 %).

The observed sexual dimorphism in mandibular traits, including chin shape, gonial eversion, muscle markings, and posterior ramus flexure, is likely associated with differences in biomechanical loading, growth patterns, and hormonal influences between males and females [3, 17, 27]. Males generally exhibit stronger masticatory muscles, particularly the masseter and medial pterygoid, which attach around the gonial region and mandibular ramus. The greater mechanical loading produced by these muscles contributes to more pronounced bone remodelling, resulting in features such as a more prominent or squared chin, everted gonial angle, and stronger muscle markings [2, 19, 21]. Posterior ramus flexure likely results from variations in the size, strength, or angulation of the masticatory muscles, particularly the masseter and medial pterygoid muscles attaching below the ramus flexure. In males, the more pronounced medial pterygoid attachment contributes to a more vertically oriented ramus, while the temporalis and lateral pterygoid muscles attach superior to the flexure [2]. In contrast, females typically generate lower masticatory forces, leading to smoother muscle attachment surfaces and less pronounced mandibular features. These morphological differences are further influenced by sex hormones and growth dynamics, as prolonged post-pubertal skeletal development in males and earlier estrogen-mediated maturation in females contribute to the development of distinct mandibular characteristics [17].

In this result, when the four significant non-metric parameters were analysed collectively using discriminant function analysis, the model achieved sex-specific predictive accuracies of 86.7 % for males and 78.9 % for females, with an overall predictive accuracy of 83.7 % based on cross-validated classification. These values indicate a substantial improvement over chance classification and demonstrate the advantage of combining multiple non-metric traits rather than relying on a single morphological feature. The use of cross-validation further strengthens the reliability of the reported accuracy by minimizing the risk of overfitting. These findings also reinforce the concept that sexual dimorphism based on mandibula is population-specific, highlighting the importance of developing local standards for forensic identification.

Despite these encouraging results, several limitations should be acknowledged. The sample size was relatively small and unevenly distributed between sexes, which may influence classification performance. Furthermore, the analysis was limited to dry mandibles and did not incorporate metric measurements or radiological data, which may provide complementary information for sex determination.

Future studies should aim to validate these findings in larger and more balanced samples, assess observer reliability, and explore the integration of non-metric and metric mandibular parameters. The incorporation of three-dimensional imaging techniques, such as CT-based morphometric analysis, may further enhance the accuracy and objectivity of sex estimation models. Nevertheless, the present study highlights the value of non-metric mandibular analysis as a rapid and practical initial step in sex determination, particularly in forensic situations involving incomplete or fragmented skeletal remains.

Conclusion

1. This study demonstrates that selected non-metric mandibular parameters exhibit significant sexual dimorphism and can be effectively utilized as an initial approach for sex determination in an Indonesian population. Among the evaluated traits chin shape, posterior mandibular ramus flexure, gonial angle divergence, and muscle markings showed statistically significant differences between males and females, with an overall predictive accuracy of 83.7 %.

2. The findings highlight the advantage of using a multivariate, non-metric approach rather than relying on a single morphological trait. Given its practicality, minimal equipment requirements, and applicability to incomplete or fragmented skeletal remains, non-metric mandibular analysis represents a valuable screening tool in forensic and anthropological contexts. However, population-specific validation remains essential, and future studies incorporating larger samples, observer reliability assessment, and complementary metric or imaging-based methods are recommended to further enhance the accuracy and robustness of sex determination models.

References

[1] Alias, A., Ibrahim, A., Bakar, S. N. A., Shafie, M. S., Das, S., Abdullah, N., ... & Nor, F. M. (2018). Anthropometric analysis of mandible: an important step for sex determination. *La Clinica Terapeutica*, *169*(5), e217-e223. doi: 10.7417/CT.2018.2082

[2] Amin, W. M. (2018). Assessing Ramus Dimorphism of Jordanian Mandibles. American Journal of Medical and Biological Research, *6*(1), 1-6. doi: 10.12691/ajmbr-6-1-1

[3] Arthanari, A., Sureshbabu, S., Ramalingam, K., Yuwanati, M., Prathap, L., & Ravindran, V. (2024). Role of Mandibular Parameters in Gender Determination: A Systematic Review and Meta-Analysis. *Cureus*, *16*(5). doi: 10.7759/cureus.59965

[4] Badran, D. H., Othman, D. A., Thnaibat, H. W., & Amin, W. M. (2015). Predictive Accuracy of Mandibular Ramus Flexure as a Morphologic Indicator of Sex Dimorphism in Jordanians. *International Journal of Morphology*, *33*(4), 1248-1254. doi: 10.4067/s0717-95022015000400009

[5] Beschiu, L. M., Ardelean, L. C., Tigmeanu, C. V., & Rusu, L. C. (2022). Cranial and odontological methods for sex estimation – A scoping review. *Medicina*, *58*(9), 1273. doi: 10.3390/medicina58091273

[6] Corda, J. V., Karthikeyan, A., Zuber, M., Jacob, M., Ramos, A., Hosapatna, M., ... & Ankolekar, V. H. (2025). Estimation of sexual dimorphism of adult human mandibles of South Indian origin using non-metric parameters and machine learning classification algorithms. *Scientific Reports*, *15*(1), 34534. doi: 10.1038/s41598-025-17831-3

[7] Datta, A., Siddappa, S. C., Gowda, V. K., Channabasappa, S. R., Shivalingappa, S. B., & Dey, D. (2015). A study of sex determination from human mandible using various morphometrical parameters. *Indian J Forensic Community Med*, *2*(3), 158-66.

[8] Deana, N. F., & Alves, N. (2017). Nonmetrical sexual dimorphism in mandibles of Brazilian individuals. *Biomed Res*, *28*(9), 4233-4238. Corpus ID: 43605627

[9] Decaup, P. H., Garot, E., Vanderesse, N., & Couture, C. (2024). How geographical origin and dietary habits interact with the shape of cortical mandibular sections? A geometric morphometrics study in an archaeological context. *Archives of Oral Biology*, *161*, 105938. doi: 10.1016/J.ARCHORALBIO.2024.105938

[10] Drake, R., Vogl, A. W., & Mitchell, A. W. (2023). *Gray's Basic Anatomy 3rd edition*. Elsevier Health Sciences.

[11] Duangchit, S., Boonthai, W., Sindecharak, T., Munkong, W., Tangsrisakda, N., Poodendaen, C., & Srisen, K. (2023). Sex Determination from the Mandible of the Northeastern Thai Population: compared between Conventional and Radiographic Measurements. *Srinagarind Medical Journal*, *38*(6), 578-588.

[12] Kumar, A., Klinkhachorn, P. S., & Mohammed, C. A. (2022). Measurement of metric and nonmetric parameters for determining the gender of the human mandible. *National Journal of Clinical Anatomy*, *11*(1), 22-29. doi: 10.4103/NJCA.NJCA_112_21

[13] Mączka, G., Kulus, M., Grzelak, J., Porwolik, M., Dobrzyński, M., & Dąbrowski, P. (2022). Morphology of the antegonial notch and its utility in the determination of sex on skeletal materials. *Journal of Anatomy*, *241*(4), 919-927. doi: 10.1111/joa.13731

[14] Mobin, N., & Vathsalya, S. K. (2018). Sexual dimorphism in adult human mandibles: a southern Indian study. *International Journal of Anatomy, Radiology and Surgery, 7*(4), 15-21. doi: 10.7860/IJARS/2018/37047:2429

[15] Padmavathi, S., Ganesan, A., Kannan, A., Krithika, C. L., & Swathi, K. (2022). Assessment of Mandibular Flexure for Sexual Dimorphism : A Retrospective Study. *Neuroquantology*, *20*(22), 557-566. doi: 10.48047/nq.2022.20.22.NQ10040

[16] Panda, B. B., Mishra, K., Hansda, M. K., Naik, S. K., & Sethi, S. S. (2016). Mandibular Ramus Notching As a Tool for Sexual Dimorphism. *International Journal of Medical Research & Health Sciences*, *5*(2), 64-69.

[17] Plotkin, L. I., Bruzzaniti, A., & Pianeta, R. (2024). Sexual Dimorphism in the Musculoskeletal System: Sex Hormones and Beyond. *Journal of the Endocrine Society*, *8*(10), 1-8. doi: 10.1210/jendso/bvae153

[18] Narayan Reddy, K. S., & Murty, O. P. (2014). *The essentials of forensic medicine and toxicology*. KS Narayan Reddy/Twentythird Edition/Medical book company–Hyderabad.

[19] Saini, V. (2017). Scrutiny of four conventional visual traits of mandible for sex estimation in Indian population. *Austin Journal of Forensic Science and Criminology*, *4*(4), 1070.

[20] Saini, V., Chowdhry, A., & Mehta, M. (2022). Sexual dimorphism and population variation in mandibular variables: a study on a contemporary Indian population. *Anthropological Science*, *130*(1), 59-70. doi: 10.1537/ase.2108282

[21] She, X., Sun, S., Damon, B. J., Hill, C. N., Coombs, M. C., Wei, F., … & Yao, H. (2021). Sexual dimorphisms in three-dimensional masticatory muscle attachment morphometry regulates temporomandibular joint mechanics. *Journal of Biomechanics*, *126*, 110623. doi: 10.1016/j.jbiomech.2021.110623

[22] Shivaprakash, S., & Vijaykumar, A. G. (2014). Sex determination by using mandibular ramus posterior flexure–A prospective study. *International Journal of Health Sciences & Research*, *4*(1), 155-159.

[23] Shree, B., Soni, S., Sharma, S. K., Handge, K., Kumar, A., Das, S. S., & Puri, N. (2023). Analytical study of mandible: prerequisite for sex determination. *Journal of Pharmacy and Bioallied Sciences*, *15*(Suppl 2), S1215-S1217. doi: 10.4103/jpbs.jpbs

[24] Sikka, A., & Jain, A. (2016). Sex determination of mandible: a morphological and morphometric analysis. *International Journal of Contemporary Medical Research*, *3*(7), 1869-1872.

[25] Singh, R., Mishra, S. R., Sushobhana, P. J., Kumar, P., Singh, S., Sinha, P., & Gupta, S. (2015). Sexual dimorphism in adult human mandible of North Indian origin. *Forensic Medicine and Anatomy Research*, *3*(3), 82-88. doi: 10.4236/fmar.2015.33014

[26] Standring, S. (Ed.). (2021). *Gray's Anatomy E-Book: Gray's Anatomy E-Book*. Elsevier Health Sciences.

[27] Toneva, D. H., Nikolova, S. Y., Fileva, N. F., Zlatareva, D. K. (2023). Size and shape of human mandible: Sex differences and influence of age on sex estimation accuracy. *Legal Medicine*, *65*, 102322. doi: 10.1016/j.legalmed.2023.102322

[28] Villanueva, E. Á., Garmendia, A. M., Torres, G., Sánchez-Mejorada, G., & Gómez-Valdés, J. A. (2017). Gender assessment using the mandible in the Mexican population. *Spanish Journal of Legal Medicine*, *43*(4), 146-154. doi: 10.1016/j.reml.2017.06.003

МОРФОЛОГІЧНИЙ АНАЛІЗ СУХОЇ ДОРОСЛОЇ МАНДІБУЛИ ЯК ПОЧАТКОВИЙ ПІДХІД ДО ВИЗНАЧЕННЯ СТАТІ

Прасетіоваті Л., Сакіна С., Деві Р. К.

Визначення статі за скелетними останками є вирішальним кроком у судово-медичній ідентифікації, особливо у випадках, коли останки неповні або фрагментовані, як-от ті, що трапляються під час масових катастроф. Серед елементів скелета нижня щелепа часто зберігається завдяки своїй високій стійкості до пошкоджень навколишнього середовища. Нижня щелепа є найбільшою та найміцнішою кісткою лицевого скелета. Вона забезпечує прикріплення основних жувальних м'язів. Нижня щелепа також демонструє чіткі морфологічні ознаки, які є цінними для визначення статі. Повідомлялося про кілька неметричних ознак нижньої щелепи, які демонструють статевий диморфізм. Однак прогностична точність цих ознак значно варіює серед різних популяцій через генетичні, функціональні та екологічні впливи. Крім того, дослідження, що вивчають неметричні характеристики нижньої щелепи в індонезійському населенні, залишаються обмеженими. Це дослідження мало на меті проаналізувати неметричні характеристики нижньої щелепи у дорослих індонезійців та оцінити їх ефективність для визначення статі. Було проведено перехресне дослідження нижньої щелепи у 49 дорослих особин (30 чоловіків та 19 жінок) з індонезійської популяції. Спостерігалися вісім неметричних параметрів, включаючи форму підборіддя, профіль підборіддя, форму гілки нижньої щелепи, профіль гілки нижньої щелепи, задній вигин гілки нижньої щелепи, розбіжність кута гоніалу, м'язове маркування та наявність антегоніальної вирізки. Статистичний аналіз проводився з використанням відповідного програмного забезпечення SPSS версії 22.0. Була розрахована частота зустрічальності кожної змінної. Статеві відмінності аналізували за допомогою тесту хі-квадрат, а рівень значущості встановлювали на рівні p<0,05. Потім проводився аналіз дискримінантної функції для оцінки комбінованої прогностичної точності значущих ознак. В результаті, чотири морфологічні ознаки продемонстрували значний статевий диморфізм, включаючи форму підборіддя (p<0,05), задній вигин гілки нижньої щелепи (p<0,001), розбіжність кута гоніального згину (p<0,001) та м'язові позначки (p<0,001). На основі аналізу дискримінантної функції, точність прогнозування визначення статі становила 86,7 % у чоловіків та 78,9 % у жінок, а загальна точність прогнозування становила 83,7 %. Отримані дані підкреслюють, що кілька неметричних морфологічних ознак нижньої щелепи, включаючи форму підборіддя, задній вигин гілки нижньої щелепи, розбіжність кута гоніального згину та м'язові позначки, демонструють виражений статевий диморфізм і тому можуть служити початковим підходом до визначення статі в індонезійській популяції. Комбінована оцінка кількох неметричних ознак покращує точність прогнозування та пропонує практичний інструмент скринінгу в судово-медичному контексті, особливо коли скелетні останки є неповними або фрагментованими.

Ключові слова: *судова антропологія, права людини, нижня щелепа, неметрична морфологія, статевий диморфізм.*

Author's contribution

Prasetiowati L. – conceived and designed the study, collected and analyzed the data, wrote the manuscript.
Sakina S. – analyzed the data, drafted the manuscript, critically revised the manuscript.
Dewi R.K. – collected and analyzed of literature sources, revised the manuscript.

Signed for print 12.03.2026
Format 60x84/8. Printing offset. Order № 1724. Circulation 100.
Vinnytsia. Printing house “TVORY”, Nemyrivske shose St., 62a,
Vinnytsya, 21034
Phone: 0 (800) 33-00-90, (096) 97-30-934, (093) 89-13-852,
(098) 46-98-043
e-mail: tvory2009@gmail.com
http://www.tvoru.com.ua